Acoustic Particle-Image Velocimetry: development and applications

Thesis

Acoustic Particle-Image Velocimetry

Development and Applications

Ali Tonddast–Navæi

Acoustic Particle-Image Velocimetry

Development and Applications

Ali Tonddast–Navæi

A Thesis
Submitted in Fulfilment of the requirements
for the Degree of
Doctor of Philosophy

13 December 2005

Abstract

Particle Image Velocimetry (PIV) is a non-intrusive technique for simultaneously measuring the velocities at many points in a fluid flow. The fluid is seeded with tracer particles and the region under investigation is illuminated. An image of the illuminated region is captured and then, a short time period later, a second image is taken. Suitable analysis of these images yields an instantaneous velocity vector map.

Until recently, restrictions in the rate at which images could be captured have limited the PIV technique to the analysis of slow flows. However, advances in camera technology have now opened up the possibility of using PIV in the analysis of faster flows. Indeed, image capture rates are now fast enough to enable two images to be captured during a fraction of an acoustic cycle, indicating the potential for using PIV to analyse sound fields.

In this thesis, after some aspects of sound field theory have been outlined and following a discussion of the theory of PIV, the development of experimental PIV apparatus for measuring sound fields is described. Measurements of the temporal variation in the velocities of particles within some common sound fields are presented. In particular, the passage of an acoustic pulse is monitored and the sinusoidal motion of particles in a resonating tube is recorded yielding the corresponding standing wave pattern. Finally, the main limitations of the PIV technique when applied to acoustic fields are discussed.

In Memory of My Grandfather

Contents

List of Figures

List of Tables

Acknowledgements

I would like to thank Dr David Brian Sharp, the project supervisor, for his patience and support. Thanks to Dr Shahram Taherzadeh, who introduced the project to me, for his guidance throughout. Thanks to Dr John Cosgrove, from the Acoustics Group of the University of Edinburgh, for his advice on initiating the instrumentation components. Thanks to Professor Murray Campbell, the supervisor of my supervisor, for his valuable discussions.

I would like to thank Alexandre-César-Léopold Bizet, Achille-Claude Debussy, George Gershwin and Donald-Ervin Knuth for their unknowing, yet remarkable, contribution to this work.

I owe much gratitude to my parents for their constant encouragement throughout and beyond this work. Thanks to my wife Leila for her timeless tolerance of a meticulous writer—without her, this work would have ended somewhere before this page.

Chapter I

Introduction

After the first acoustic velocity measurements were carried out by Rayleigh at the end of the 19th century, there followed a long period during which there were only small advances in the measurement of velocities in sound fields. Indeed, it was nearly a century later, with the employment of optical methods, that acoustic velocimetry took its next leap forward.

Particle Image Velocimetry (PIV) has become a widely used optical method for measuring fluid flow velocities. It has the unique features of being non-intrusive and whole-field; that is, simultaneously measuring the velocities at many points in a fluid flow without any disturbance to it. The technique involves seeding the fluid with tracer particles and illuminating the region under investigation. Two or more images of the illuminated region are then captured in rapid succession. Finally, the images are analysed to extract the velocity values.

Until recently, restrictions in the rate at which images could be captured have limited the PIV technique to the analysis of slow flows. However, advances in camera technology have now opened up the possibility of using PIV in the analysis of faster flows, in particular for the measurement of sound fields.

1.1 The Aims

The main goals of the present work are:

1. To investigate the possibility of employing PIV to study high-speed acoustic motions, exploring the limits under which the principles underpinning PIV remain valid for acoustic measurements.

2. To develop a PIV set-up which is capable of measuring acoustic particle velocities. That is, a measurement system that is able to accurately record the oscillatory motion of particles in sound fields.

3. To employ the extended PIV set-up in the spatial and temporal measurement of acoustic velocity.

1.2 Outline of Thesis

Chapter 2 presents a brief theory of sound fields. In particular, the equations of resonant tubes, which are later studied experimentally, are introduced.

Chapter 3 is an in-depth review of the theory and development of Particle Image-Velocimetry. The chapter covers the structure of PIV systems, describing in detail each component of the technique. It then presents the theory behind the most common method of PIV data analysis. Throughout, specific attention is paid to the digital form of the technique.

Based on the previous chapters, Chapter 4 discusses the potential problems associated with using PIV for sound field measurements. The assumptions upon which PIV are based are examined to verify that they remain valid when measuring sound fields. In particular, the level of intrusion caused by the measurements and the degree to which the results truly reflect the actual acoustic velocities are investigated.

Chapter 5 describes the experimental configuration used in this study presenting the design of the data acquisition and data analysis systems.

Chapter 6 examines some applications of acoustic PIV. It presents the results of the measurement of some common sound fields. In particular, the passage of an acoustic pulse is monitored and the sinusoidal motion of particles in resonating tube is recorded yielding the corresponding standing wave pattern. Finally, it discusses some unexpected results encountered during the acoustic PIV measurement of oscillatory motions.

The thesis concludes with Chapter 7 which contains a summary of the main findings of the research and some ideas for future work.

Part I

Theory

Chapter 2

Sound Fields

All science is either physics or stamp collecting.

Ernest Rutherford

This chapter covers those parts of sound field theory which are related to this study. A detailed development of the theory presented in this chapter can be found in most standard acoustics and fluid dynamics textbooks (Meyer and Neumann 1972; Morse and Ingard 1968; Kinsler et al. 2000; Skudrzyk 1971; Landau and Lifshitz 1987) and consequently only the most pertinent results are outlined here.

2.1 Terminology

2.1.1 Fluid Flows

Throughout this study, it is considered that the fluid under investigation consists of *fluid elements*, which are volumes small enough that all the sound field parameters can be assumed to be constant within them. The position of a fluid element, in the Cartesian co-ordinate system, is denoted by

$$\vec{x} = (x, y, z) = x\hat{x} + y\hat{y} + z\hat{z}, \tag{2.1.1}$$

where $\hat{x}$, $\hat{y}$ and $\hat{z}$ are the unit vectors. When at rest, i.e. when there is no force applied to any of its elements, the fluid has an *equilibrium pressure* of P_0 and

equilibrium density of ρ_0.

When the effect of energy dissipation is considered, the fluid is said to be *real* or *viscous*. Energy dissipation in fluids is an irreversible process which is caused by *viscosity*, which is the internal friction between molecules of the fluid, or thermal conduction or both. In the idealised case, where all of these effects are negligible, the fluid is referred to as *ideal* or *inviscid*.

Fluids are also classified according to their compressibility. In a *compressible fluid* the equilibrium density is a function of space and time while it is a constant value in an *incompressible fluid*.

2.1.2 Acoustical Parameters

In the presence of forces generated by a sound field, the instantaneous properties of the fluid are said to be acoustical in nature. Under this condition, a fluid element has an *instantaneous displacement* from its equilibrium position denoted by

$$\vec{\xi} = (\xi_x, \xi_y, \xi_z).$$

The velocity associated with this instantaneous displacement is known as the *acoustic velocity* and is denoted

$$\vec{v} = (v_x, v_y, v_z) = \partial_t \vec{\xi}. \tag{2.1.2}$$

The *acoustic pressure* p is the difference between the the *instantaneous pressure* $\mathcal{P}$ and the equilibrium pressure:

$$p = \mathcal{P} - \mathcal{P}_0. \tag{2.1.3}$$

The *instantaneous density* ρ defines the *condensation* of the fluid as

$$s = \frac{\rho - \rho_0}{\rho_0}. \tag{2.1.4}$$

2.2 Fundamental Equations

A sound field in a fluid can be fully described by the corresponding acoustic velocity $\vec{v}$ and two thermodynamic quantities, which are usually acoustic pres-

sure $\mathcal{P}$ and condensation s. These parameters are related by three fundamental equations presented in this section.

2.2.1 Equation of Motion

The equivalent of NEWTON's equation of motion in an incompressible viscous fluid is the *Navier-Stokes equation* which in its general form may be written as

$$\rho \left(\partial_t \vec{v} + (\vec{v}.\vec{\nabla})\vec{v} \right) = -\vec{\nabla} p + \eta \nabla^2 \vec{v} + \left(\frac{1}{3}\eta + \eta_B \right) \vec{\nabla}(\vec{\nabla}.\vec{v}). \tag{2.2.1}$$

where η is the *shear* or *dynamic viscosity coefficient* of the fluid and η_B is the *bulk viscosity coefficient* of the fluid.

For an incompressible fluid, when $\vec{\nabla}.\vec{v} = 0$ and the viscosity is zero, the NAVIER-STOKES equation is reduced to *Euler's equation of inviscid motion* given by

$$\rho \left(\partial_t \vec{v} + (\vec{v}.\vec{\nabla})\vec{v} \right) = -\vec{\nabla} p. \tag{2.2.2}$$

For steady flow, EULER's equation simplifies to *Fourier's law*, which is expressed as

$$\rho (\vec{v}.\vec{\nabla})\vec{v} = -\vec{\nabla} p. \tag{2.2.3}$$

In the linear acoustics approximation, the second order term in EULER's equation is negligible and the equation is reduced to

$$\rho \, \partial_t \vec{v} = -\vec{\nabla} p, \tag{2.2.4}$$

which is known as the *linear Euler equation*.

2.2.2 Equation of Continuity

Based on the law of conservation of mass, the *equation of continuity* of a fluid can be derived as

$$\partial_t \rho + \vec{\nabla}.(\rho \, \vec{v}) = 0, \tag{2.2.5}$$

which relates the motion of the fluid to its compression or expansion. In the linear acoustic estimation, the *linear equation of continuity* is given by

$$\partial_t s + \vec{\nabla}.\vec{v} = 0. \tag{2.2.6}$$

2.2.3 Equation of State

When the host fluid is a perfect gas, in most cases, the change of all parameters of the sound field is much faster than the change of temperature. As a result, the temperature can be assumed to be a constant implying that the host fluid is *adiabatic*. This requires the condition

$$\frac{\mathcal{P}}{\mathcal{P}_0} = \left(\frac{\rho}{\rho_0}\right)^{\gamma}, \tag{2.2.7}$$

where γ is the *ratio of specific heats* given by

$$\gamma = \frac{c_P}{c_V}, \tag{2.2.8}$$

with c_P and c_V representing the *specific heat at constant pressure* and *specific heat at constant volume*, respectively.

The *equation of state* for an adabatic gas is given by

$$p = c^2 (\rho - \rho_0), \tag{2.2.9}$$

where c is the *thermodynamic speed of sound* given by

$$c = \left(\frac{\mathcal{P}_0}{\rho_0}\right)^{\frac{1}{2}}. \tag{2.2.10}$$

In the linear approximation, when the condensation is much smaller than unity, the *linear equation of state* can be found from Taylor's expansion of the instantaneous pressure around its equilibrium value. This yields

$$p = \mathcal{B}\, s, \tag{2.2.11}$$

where $\mathcal{B}$ is the *adiabatic bulk mudulus* given by

$$\mathcal{B} = \rho_0 \left(\partial_\rho \mathcal{P}\right)_{\rho_0}. \tag{2.2.12}$$

2.3 Linear Sound Waves

2.3.1 Propagating Waves

Combining the linear forms of the fundamental equations for an inviscid fluid yields the *linear lossless wave equation* of propagation of sound as (Kinsler et al. 2000)

$$\Box^2 p(\vec{x}, t) = 0, \tag{2.3.1}$$

where $\Box^2$ denotes the d'Alembertian operator defined as

$$\Box^2 = \nabla^2 - c^{-2}\,\partial_t{}^2, \tag{2.3.2}$$

with c being the speed of propagation of sound in the fluid and ∇^2 denoting the Laplacian operator.

The general solution of Equation (2.3.1) is a *harmonic plane wave*. That is, a wave where, at any point on a plane perpendicular to the direction of propagation, the properties of the sound field are the same.

In *potential* or *irrotational fluids*, i.e. when $\vec{\nabla} \times \vec{v} = 0$, the acoustic velocity may be presented in terms of the gradient of a scalar, known as the *velocity potential*, by[1]

$$\vec{v}(\vec{x}, t) = \vec{\nabla}\phi(\vec{x}, t). \tag{2.3.3}$$

Using the linear Euler equation (2.2.4), the pressure can be expressed in terms of the temporal differentiation of the velocity potential:

$$p(\vec{x}, t) = -\rho_0\,\partial_t\phi(\vec{x}, t). \tag{2.3.4}$$

Practically, when calculating properties of sound fields, the aim is to obtain the velocity potential which in turn yields the other parameters. It can be shown that, with the same linear approximation, the velocity potential satisfies the wave equation as

$$\Box^2\phi(\vec{x}, t) = 0, \tag{2.3.5}$$

In this study, the plane waves of interest are one-dimensional, satisfying the

[1] Sometimes the velocity is expressed, conventionally, by the gradient of the velocity potential with a minus sign, i.e. $\vec{v}(\vec{x}, t) = -\vec{\nabla}\phi(\vec{x}, t)$.

reduced linear wave equation

$$(\partial_x^2 - c^{-2}\,\partial_t{}^2)\,\phi(x,t) = 0, \tag{2.3.6}$$

which has real harmonic solutions in terms of the trigonometric functions. It is convenient to express these solutions in the complex exponential form and then use the real part.[2] With this in mind, the solution of Equation (2.3.6) can be written as

$$\phi(x,t) = \Re\left[\phi_x(x)\,e^{-\imath\omega t}\right], \tag{2.3.7}$$

where ω is the *angular frequency* of the wave and the velocity potential ϕ_x is a function only of space fulfilling the Helmholtz equation

$$(\nabla^2 + k^2)\,\phi_x(\vec{x}) = 0, \tag{2.3.8}$$

with k being the *wave number* related to the *wavelength* λ by

$$k = \frac{\omega}{c} = \frac{2\pi}{\lambda}. \tag{2.3.9}$$

Solving the Helmholtz equation (2.3.8), the final form of the velocity potential may be given by

$$\phi(x,t) = \Re\left[\phi_0\,e^{\imath(kx-\omega t)}\right], \tag{2.3.10}$$

where ϕ_0 is the amplitude. Equation (2.3.10) describes a *monochromatic* (i.e. with constant frequency ω) *travelling wave* propagating in an infinite medium in the x direction and with a speed of ω/k.

The *linear lossy wave equation* for a viscous fluid may be obtained by combining the linear equations of continuity and state with the Navier-Stokes equation for incompressible fluid to give

$$\Box_L^2\phi(\vec{x},t) = 0, \tag{2.3.11}$$

where $\Box_L^2$ stands for the lossy d'Alembertian operator defined as

$$\Box_L^2 = (1+\tau_f\partial_t)\nabla^2 - c^{-2}\,\partial_t{}^2, \tag{2.3.12}$$

[2] Usually, when only linear operations are involved, the real part sign is omitted during calculations but appears in the final results.

with τ_f denoting the *relaxation time of the viscous fluid element*.

It can be shown (Kinsler et al. 2000, §8.2) that the general solution of the lossy wave equation (2.3.11) is the same as the lossless version but with a complex wave number

$$\mathbf{k} = k + \imath\,\alpha, \tag{2.3.13}$$

where the boldface denotes a complex variable and α is the *absorption coefficient*. Thus, one-dimensional wave propagation in a real fluid can be described by

$$\boldsymbol{\phi}(x,t) = \phi_0\, e^{\imath(\mathbf{k}x-\omega t)}. \tag{2.3.14}$$

2.3.2 Standing Waves

Many observed acoustical phenomena take place in finite media where the sound waves meet the boundaries of the finite media. In such a case, based on the properties of the boundaries, the incident waves convert to reflected and/or transmitted waves.

Sound fields in finite one-dimensional media can be described by *acoustic transmission line* theory. With reference to Equation (2.3.10), a lossy transmission line consists of an incident wave

$$\boldsymbol{\phi}^{\rightarrow}(x,t) = \phi_0^{\rightarrow}\, e^{\imath(+\mathbf{k}x-\omega t)}, \tag{2.3.15}$$

and its reflection from a real boundary

$$\boldsymbol{\phi}^{\leftarrow}(x,t) = \phi_0^{\leftarrow}\, e^{\imath(-\mathbf{k}x-\omega t)}, \tag{2.3.16}$$

where it is assumed that the boundary wall is *rigid* or *acoustically hard*, that is, the incident wave is almost completely reflected. The linear superposition of these waves at each point inside the finite medium and at any instant yields

$$\boldsymbol{\phi}(x,t) = \boldsymbol{\phi}^{\rightarrow}(x,t) + \boldsymbol{\phi}^{\leftarrow}(x,t). \tag{2.3.17}$$

Applying the boundary conditions for a finite medium, Equation (2.3.17) can only be satisfied for a limited number of frequencies known as the *natural* or *characteristic frequencies* of that finite medium. Moreover, the waves described by the solutions of this equation do not propagate in space and are said to be *stationary* or *standing waves*.

2.3.3 Impedance

The *acoustic impedance* acting on a surface of area S is defined as the quotient of the complex acoustic pressure and the complex volume velocity associated with that area:

$$Z(x,t) = \frac{\mathbf{p}(x,t)}{S\,\boldsymbol{v}(x,t)}. \tag{2.3.18}$$

The *specific acoustic impedance* is, in general, given by the quotient of the acoustic pressure and velocity as

$$Z_S(x,t) = \frac{\mathbf{p}(x,t)}{\boldsymbol{v}(x,t)}. \tag{2.3.19}$$

In the special case, where the acoustic pressure and velocity correspond to a plane wave, the specific acoustic impedance is

$$Z_0 = \rho_0\, c. \tag{2.3.20}$$

which is known as the *characteristic acoustic impedance* or the *wave impedance of the medium*.

2.4 Theory of the Resonance Tube with Rigid Ends

Consider a tube[3] of length L which is driven at one end ($x = 0$) by a sound generating device, eg a piston or a loudspeaker, and closed at the other end ($x = L$). Both ends of the tube are assumed to be rigidly terminated. Let the sound generating device produce a monochromatic wave with frequency ω shown by

$$x'(t) = l\sin(\omega t), \tag{2.4.1}$$

where l is the displacement amplitude of the sound generating device.

In the steady state, the velocity potential created by the sound source inside the tube, as a finite medium, can be described by the standing wave Equation (2.3.17) as

$$\boldsymbol{\Phi}(x,t) = \phi_0^{\rightarrow} e^{\imath(+\mathbf{k}x-\omega t)} + \phi_0^{\leftarrow} e^{\imath(-\mathbf{k}x-\omega t)}. \tag{2.4.2}$$

[3] Other commonly used synonyms of 'tube' in the literature are *duct*, *pipe* or *wave-guide*.

The 'exact' boundary conditions of this system may be given by

$$v(x', t) = \partial_x \phi(x, t) \mid_{x=x'} = \partial_t x'(t), \tag{2.4.3}$$

for the sound generating side and

$$v(L, t) = \partial_x \phi(x, t) \mid_{x=L} = 0, \tag{2.4.4}$$

for the rigid termination side of the tube.

2.4.1 Assumptions

Before solving the standing wave Equation (2.4.2) some assumptions must be taken into account.

First, it is supposed that the wave equation is linearised. However, the boundary condition Equation (2.4.3) leads the constant velocity amplitudes $v_0^{\rightarrow}$ and $v_0^{\leftarrow}$ to be a function of time and, consequently, generating non-linear solutions. This may be overcome by assuming that the displacement amplitude of the sound generating device is negligible comparing to the length of the tube (Temkin 1981, §3.6) or

$$\frac{l}{L} \ll 1, \tag{2.4.5}$$

which causes the boundary condition Equation (2.4.3) to be replaced by

$$v(0, t) = \partial_x \phi(x, t) \mid_{x=0} \cong 0. \tag{2.4.6}$$

Hence, Equations (2.4.5) and (2.4.6) are required to be met for a linear regime.

The second assumption is important in order to have a plane *and* longitudinal sound wave inside the tube. Of these criteria, the first one can be fulfilled when the length of the tube is much larger than its transverse dimensions or, in other words, if

$$L \gg \sqrt{S}. \tag{2.4.7}$$

where S denotes the transverse cross section of the tube. Apparently, the wave created by the sound generation device can be purely longitudinal when the device motion is perpendicular to the axis of the tube. However, in practice this may not happen perfectly. It can be shown that there exists a cut-off frequency proportional to $l/\sqrt{S}$ under which, even when the device motion normal is not

absolutely axial, any transverse waves are dumped quickly (Temkin 1981, §3.5). This criterion may be written as

$$\omega \lessapprox \frac{l}{\sqrt{S}}. \tag{2.4.8}$$

Finally, it is assumed that the attenuation is negligibly small, i.e. $\mathbf{k} \cong k$ which implies $\mathbf{Z}_S \cong Z_0$.

2.4.2 Solutions

Under the previous assumptions, the standing wave Equation (2.4.2) may be fulfilled by the real solutions

$$\phi_n(x,t) = \phi_0 \cos(k_n x) \sin(\omega_n t) + \text{const}, \tag{2.4.9}$$

with

$$k_n = \frac{2\pi}{n\lambda}, \tag{2.4.10a}$$

$$\omega_n = 2\pi n f. \tag{2.4.10b}$$

Here, n denotes a natural number and each of its values stands for a certain *mode of vibration*. Similarly, the value of ω_n corresponds to the nth angular *resonance frequency*.

Using the velocity potential solutions (2.4.9), and in the light of Equations (2.3.3) and (2.3.4), the acoustic velocity and pressure may be derived as

$$v_n(x,t) = v_0 \sin(k_n x) \sin(\omega_n t), \tag{2.4.11}$$

and

$$p_n(x,t) = p_0 \cos(k_n x) \cos(\omega_n t), \tag{2.4.12}$$

respectively, where v_0 and p_0 are the velocity and pressure amplitude related by

$$p_0 = v_0 Z_0. \tag{2.4.13}$$

Chapter 3

Particle-Image Velocimetry

The word you've entered [velocimetry] isn't in the dictionary.

Merriam-Webster's Online Dictionary
http://m-w.com

Despite its high-tech features, Particle Image Velocimetry (PIV) is based on a simple idea: recording moving objects at known times and extracting their displacements by comparing the recordings. Maybe this is the most basic understanding one can have of the concept of 'velocity'.

This chapter is an overview of the principles of PIV and the theory of PIV data analysis in general.

3.1 Historical Overview

The description of fluid flow can be traced back to very early works of art in the way that the artists painted streams, rivers or ocean waves. However, from a scientific point of view, maybe the first documented *flow visualisation* was performed by Lèonardo da Vinci in his qualitative studies of cardiac mechanics and the vascular system in the 16th century (Gharib et al. 2002). Figure (3.1) shows Vinci's schematic drawings of the cardiovascular system.

In 1883 Osborne Reynolds used flow visualisation to demonstrate the laminar to turbulent transition (Reynolds 1883) which enabled him to specify a dimensionless number to describe the flow, later named the *Reynolds number*. The

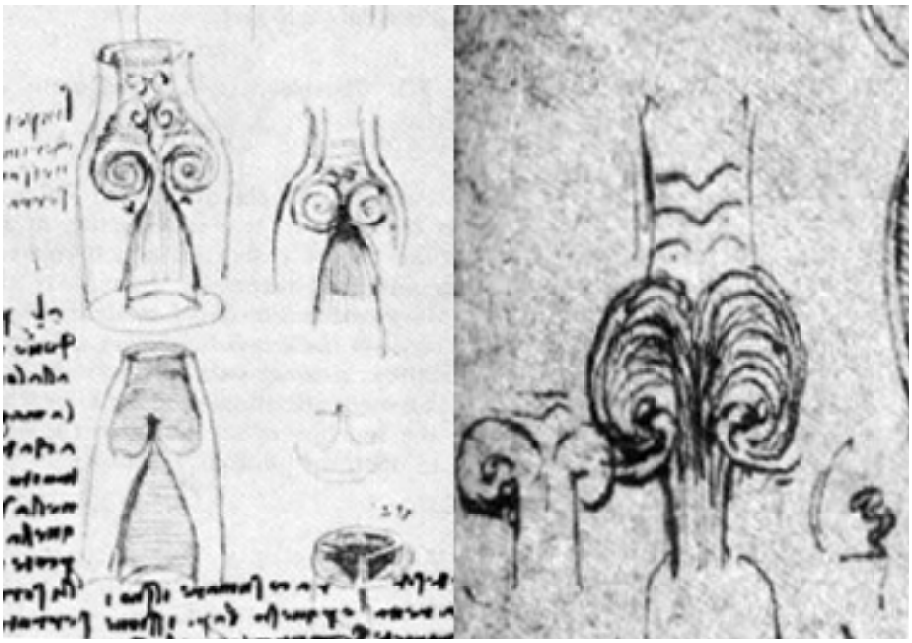

Adopted from (Gharib et al. 2002).

Figure 3.1: *Lèonardo da Vinci's vision.*

flow visualisation employed by Reynolds involved sketching water flow in different laminar and turbulent phases. Later, at the beginning of the 20th century, Ludwig Prandtl studied the steady and unsteady behaviour of water flow in a tunnel by applying mica particles to trace fluid motion at the surface (Prandtl 1904).

The invention of photography provided researchers with the ability to record their flow observations with greater reliability and accuracy. It is possible that, prior to the scientific application of taking pictures for fluid dynamics research purposes, art photographers began capturing images of flows (Grant 1997). Ogle Winston Link is well-known for his photo collection picturing American steam locomotives at the end of their era (Figure (3.2)). His most renowned works were taken at night using elaborate flash bulb systems to capture steam particles in air.

In parallel with progress in photographic technology, namely the increase in the spatial resolution of photographs, the innovation of the laser made it possible

Figure 3.2: *'Hotshot Eastbound' by Ogle Winston Link in 1950's.*

to improve the temporal resolution. These improvements paved the way for a new family of optically-based flow visualisation measurement systems, with the overarching name of *laser velocity-meter* (*velocimetry*).

Like many other scientific breakthroughs, the first use of laser velocimetry was accidental. In their Brownian motion studies using laser scattering, Cummins et al. found an unpredicted net shift in the frequency of the incident laser (Cummins et al. 1964). They created a model calculating the velocity of particles from the Doppler shift and promptly published a paper describing the fundamentals of *Laser Doppler Velocimetry* (*LDV*), also known as *Laser Doppler Anemometry* (*LDA*) (Yeh and Cummins 1964).

Laser Speckle Velocimetry (*LSV*), first demonstrated by Barker and Fourney (1977), had the novelty of measuring the flow velocity in a less intrusive way than that offered by LDV. The technique, based on the measurement of the velocity of the visualised fluid-markers, also has the advantage of being whole-field.

It is difficult to pinpoint the first usage of PIV as this method emerged from LSV, borrowing many data acquisition and analysis components from the laser velocimetry family. It has been pointed out (Adrian 1991; Westerweel 1993) that when people were performing LSV observations, they were not aware that

they were in fact carrying out PIV measurements. An extensive review of the development of PIV may be found in Adrian (1986*b*).

The theory underpinning the analysis of PIV data is mainly due to Adrian (Adrian 1984; Adrian and Yao 1985; Adrian 1988*a*; Keane and Adrian 1990, 1991, 1992). In its early days, PIV data evaluation was quite time consuming as it was based on opto-mechanical techniques. One major advance which has eliminated this problem is the use of digital technology in the data processing, enabling the method to be automated and, almost, real-time (Willert and Gharib 1991; Westerweel 1997).

Nowadays, PIV is a well-established technique. It has been applied to the study of flows in many research fields and commercial PIV measurement systems are readily available.

3.2 Pulsed Light Velocimetry

Consider a system of independently moving objects. An ideal velocity-meter which can measure both the magnitude and direction of the velocities of the objects should follow the rationale below:

data acquisition. Marking the moving objects in space and time.

Rule 3.i. *Spatial marking* is necessary when the actual objects are not visible. It can be achieved by adding some easy-to-visualise but faithful-to-follow external objects to the system.

Rule 3.ii. The spatial marking must not be intrusive to the system. In addition, the markers must not interact with each other.

Rule 3.iii. *Temporal marking* is defined as capturing the spatial state of the system at a given time. The marking time should be short enough so that the moving objects can be considered as 'frozen' within it.

data analysis. Evaluating the recorded markings. Based on the fundamental definition of velocity and depending on the characteristics of the marking data, an evaluation process can be applied to yield the velocity vectors corresponding to the observed objects.

This abstract velocity-meter can be applied to fluid flows almost without losing its generalisation. Since the fluid elements under investigation are not visible normally, some fluid markers, also called *tracer particles* or *seeding particles*, which fulfill rules (3.i) and (3.ii) are added to it. Based on rule (3.iii), the tracer particles are illuminated at least twice for a short enough time and their images are recorded for subsequent processing. The analysis process converts the images to a grid of velocity vectors or a *vector-map*. As the temporal marking part of the measurement is usually carried out by short pulses of light, the technique is referred to as *Pulsed Light Velocimetry* (*PLV*).

3.2.1 The PLV Class

Adrian (1991) classified PLV according to the attributes of the applied fluid markers and the phases of the PLV images (Figure (3.3)). In the first step, the PLV class is organised according to the fluid marker type. Molecular markers, which are activated by laser beams to visualise the flow, are used only in the study of certain flows whereas particulate markers have a more general usage. It is particulate markers which are of particular interest in this study.

Depending on how the PLV data collection system is configured, for particulate markers the acquired data falls into one of three phases, each of which requires its own specific method of analysis. These three phases are explained in the next section.

3.2.2 PLV Data Phases

Raw PLV data comprises an image which records the positions of the fluid markers, referred to as *particle-images*, at an arbitrary time. The phase of a PLV image is specified by two dimensionless numbers. We review these numbers here and leave their analytical definitions for later.

source density $\mathcal{N}_S$. A number that determines whether the particle-images are distinct individuals or whether they overlap each other in the image plane and form a *speckle*.

image density $\mathcal{N}_I$. In processed PLV data, which has a grid structure with velocity vectors at each grid point, a vector is representative of a specific region around it known as an *interrogation area*. Image density is the number of particle-images within an interrogation area.

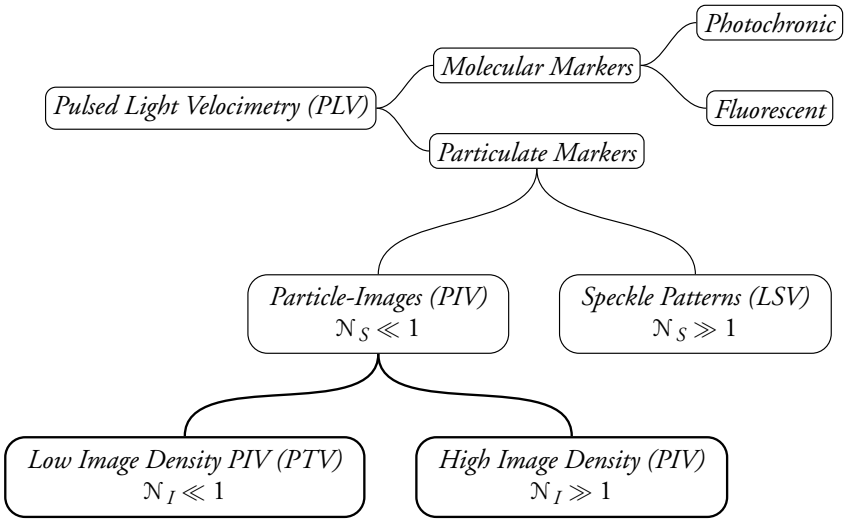

Figure 3.3: *Pulsed Light Velocimetry class as grouped by Adrian (1991).*

Different values of source and image densities result in three possible phases for PLV data (Figure (3.4)).

3.2.2.1 Laser-Speckle Phase: $\mathcal{N}_S \gg 1,\ \mathcal{N}_I \gg 1$

When the source density $\mathcal{N}_S$ is too high, which obviously requires the image density $\mathcal{N}_I$ to be high too, the particle-images cannot be found in the single form. Instead, the light scattering from the tracer particles overlaps and creates a pattern known as *laser speckle* (Figure (3.4c)). The image processing method require for this phase determines the displacement of speckles between successive exposures, a technique referred to as *Laser Speckle Velocimetry* (*LSV*).

3.2.2.2 Low-Density Particle-Image Phase: $\mathcal{N}_S \ll 1,\ \mathcal{N}_I \ll 1$

In this case the source density $\mathcal{N}_S$ is so low that the distances between particle-images are much more than their dimensions. This leaves most of the interrogation areas empty. The ones which do contain some scattering particles have so few of them that it becomes easy to link the particle-images from two successive

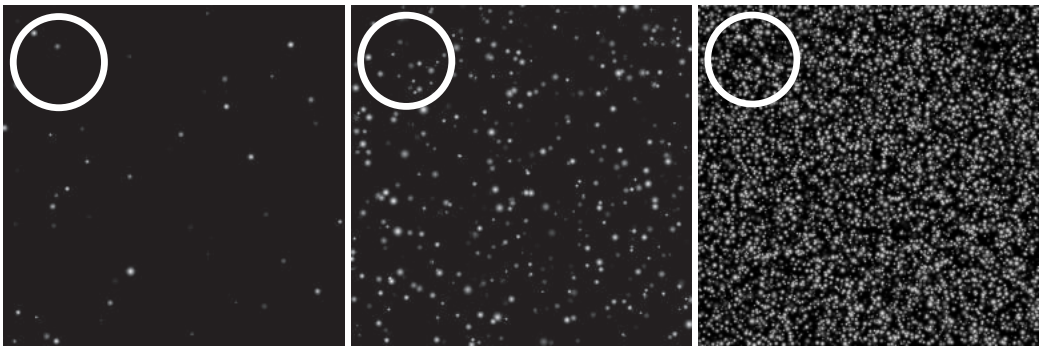

a) *PTV:* $\mathcal{N}_S \ll 1, \mathcal{N}_I \ll 1$. b) *PIV:* $\mathcal{N}_S \ll 1, \mathcal{N}_I \gg 1$. c) *LSV:* $\mathcal{N}_S \gg 1, \mathcal{N}_I \gg 1$.

The circles display interrogation areas.

Figure 3.4: *PLV data phases.*

exposures; i.e. it is practical to 'track' each individual particle (Figure (3.4a)). The related image analysis method for this phase is called *Particle Tracking Velocimetry* (*PTV*). Because of the lack of spatial data, it is not possible to get a regular multi-field grid of velocity vectors from this 'particle-tracking' phase.

3.2.2.3 High-Density Particle-Image Phase: $\mathcal{N}_S \ll 1,\ \mathcal{N}_I \gg 1$

This phase falls between the laser-speckle and particle-tracking phases. That is, the source density $\mathcal{N}_S$ is low enough to give separate particle-images, but there are sufficient scattering particles contained within each interrogation area for velocity vectors to be extracted (Figure (3.4b)). The high image density $\mathcal{N}_I$ increases the ambiguity in matching the scattering particles in successive exposures, making particle-tracking style processing inefficient. Instead, the displacement of particle-images is calculated 'in group' using statistical techniques. This is the essence of *Particle Image Velocimetry* (*PIV*) image evaluation.

3.2.3 PIV Principles

The remainder of this chapter is focused on the high-density particle-image, or PIV, phase. The principles of PIV are, in general, the same as those described in the implementation of the abstract velocity-meter at the beginning of §3.2. The

forthcoming sections, as outlined in Figure (3.5), discuss each element of the PIV method in detail.

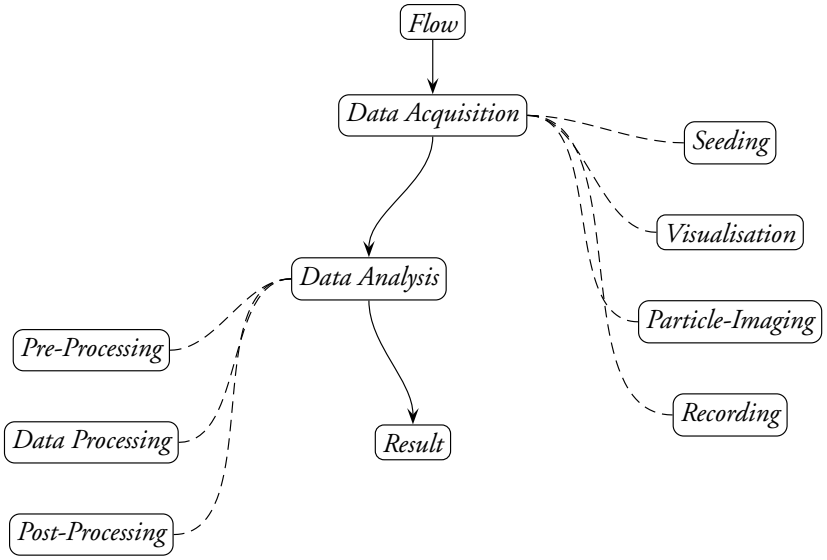

Figure 3.5: *Principles of PIV.*

3.3 Visualisation

3.3.1 Light Sources

While white light sources have the advantages of being low-cost and not restricted by laser safety rules, they are not the best choice as they are less collimated than monochromatic sources and recording mediums are not optimised for them.

Lasers have been used widely in PIV set-ups since the early days of the technique. Apart from being free of the disadvantages of white light sources, the variety of laser types makes them suitable for specific purposes.

cw. *Continuous Wave* (*CW*) lasers have an output beam which can be operated continuously. The power is adjustable and, by applying a mechanical

shutter, it is possible to generate short pulses from the output. However, the output power may not be high enough for high-speed flow visualisation or short-exposure PIV recording.

PULSED. Unlike continuous wave lasers, *pulsed* lasers have a discrete output. Pulsed lasers can be one or more of the following types:

Q-SWITCHED. The output of a *Q-switched* laser is a short-duration high-energy pulse which is generated using a shutter-like device. [1] The device releases the output only when the built-up laser energy reaches a specific limit.

SINGLE-PULSED. Also known as the *normal mode*, the output of a *single pulsed* laser consists of only one pulse which is of the order of 0.1 to 1 ms.

REPETITIVE-PULSED. Also known as *scanning* lasers, the *repetitive-pulsed* lasers have an output of the order of 10^4 pulses per second.

MODE-LOCKED. Although laser beams are monochromatic, in the laser cavity there is a range of modes close in frequency to each other; this can affect the characteristics of the output. The *locking* technique synchronises the phases of all the modes and, consequently, generates an output of regularly-spaced pulses. The duration of each pulse is around 10^{-15} to 10^{-12} s.

Table (3.3.1) lists some common lasers employed in PIV and describes their properties. It can be seen that Nd:Yag lasers have features which are very appropriate for PIV measurement.

3.3.2 Light Sheet

The minimum optical configuration needed to create a sheet from a beam of light is a cylindrical lens. When the light beam is narrow and collimated, a single cylindrical lens can be effective in generating a sufficiently thin light sheet. However, in most cases it is preferable to add a few more optical elements into the configuration to allow control of the thickness, height and intensity distribution of the sheet. In this section, various ways of generating light sheets, along with a formulation of their intensity distribution, are presented.

[1] The 'Q' refers to the measure of the sharpness of the resonance peak.

Laser	*Name*	*Wavelength* nm	*Power*	*CW*	Pulsed QS*	ML†	SP‡	RP§
He-Ne	Helium-Neon	633	10^{-3} - 10^{-2} *W*	✓				
Cu	Copper-Vapor	510, 578	1 - 30 *W*				✓	
Ar^{+}	Argon-Ion	488, 514	60 - 100 *W*	✓	✓		✓	
Cr^{+3}	Ruby	694			✓		✓	
Nd:YAG	Neodym:YAG¶	532	$>$ 0.4 J per pulse	✓		✓		✓

* Q-Switch.
† Mode-Locked.
‡ Single-Pulsed.
§ Repetitive-Pulsed.
¶ Yttrium-Aluminium-Garnet.

Source: Young (1986).

Table 3.1: *General properties of some lasers used in PIV.*

3.3.2.1 Configurations

Figure (3.6) shows some schematic optical configurations for creating light sheets, as suggested by Raffel et al. (1998).

One way to manipulate the light sheet emerging from a cylindrical lens is to add two more lenses of the same type in order to vary the height and thickness (Figure (3.6a)). Because of safety reasons, which will be explained shortly, the focal point of this configuration is chosen to be virtual. This restricts the structure spatially and consequently puts a lower limit on the thickness of the final light sheet.

Sandwiching the sheet-generating cylindrical lens between two spherical lenses (one diverging and one converging) provides the option of more dynamic variation of the height and thickness of the sheet (Figure (3.6b)); nonetheless, these parameters cannot be controlled independently of each other. The configuration has the advantage of being more economical by using spherical lenses as opposed to cylindrical.

Both of the previous configurations contain a lens with a negative focal length. This ensures there is no real focal point in the set-up which prevents any high-energy concentration point in the system. When using a high-energy laser as a light source, focal points are generally to be avoided as they can burn small particles like dust floating around the point or, in a less likely case, ionise the

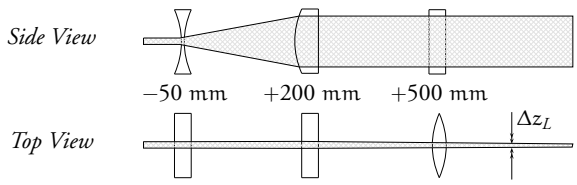

a) −*Cylindrical*, +*Cylindrical*, +*Cylindrical*

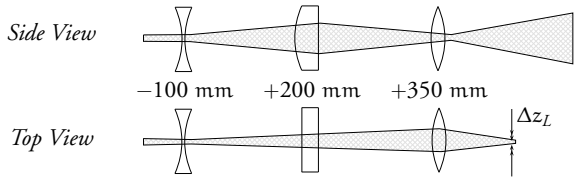

b) −*Spherical*, +*Cylindrical*, +*Spherical*

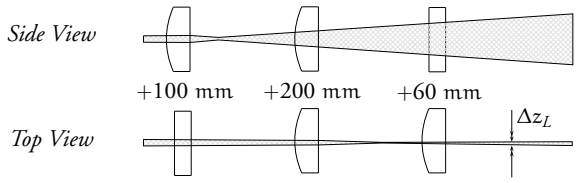

c) +*Cylindrical*, +*Cylindrical*, +*Cylindrical*

Shifting the lenses respect to each other adjusts the height and/or thickness of the light sheet. Adopted from Raffel et al. (1998).

Figure 3.6: *Some light sheet generation configurations.*

air particles. In cases where versatility is crucial, a configuration such as the one depicted in Figure (3.6c) can be used in conjugation with appropriate safety precautions.

3.3.2.2 Intensity Profile

If the generated light sheet is assumed to lie in the x-y plane, and the illuminated area of interest is small enough to make the light intensity distribution constant in the plane, the intensity profile will be a function only of the depth z. The spatial variation in intensity of light emitted from a point source is Gaussian in nature; the same is true of light from a line source. Hence, the intensity profile of a light sheet can be expressed as a Gaussian function of z:

$$\mathcal{I}(z) = \mathcal{I}_0 e^{-8(z-z_0)^2/\Delta z_L{}^2}, \tag{3.3.1}$$

with $\mathcal{I}_0$, z_0 and Δz_L being the maximum intensity, position of the centre and thickness of the light sheet respectively.

Some modern optical set-ups offer an intensity profile with a rectangular box form given by

$$\mathcal{I}(z) = \begin{cases} \mathcal{I}_0 & \text{if} \quad |z - z_0| \leqslant \Delta z_L/2 \\ 0 & \text{elsewhere} \end{cases} . \tag{3.3.2}$$

3.4 Particle-Imaging

Figure (3.7) illustrates the optical details of the particle-imaging system in a PIV set-up. The camera's convex spherical lens is assumed to be thin and aberration-free[2] with a focal length of γ_f and diameter of D_L . The average distance of the light sheet described in §3.3.2 to the camera lens is d_o, while the average distance of the camera lens to the image plane is d_i. The finite thickness of the light sheet Δz_L causes the visualised seeding particles to lie at different depths from the lens. Therefore, their images are magnified by a factor which depends on the depth z. Assuming the origin of the axes is chosen to be at the centre of the light sheet:

$$M(z) = \frac{d_i}{d_o - z}, \; -\frac{\Delta z_L}{2} < z < +\frac{\Delta z_L}{2}, \tag{3.4.1}$$

where d_o and d_i are related to each other by

$$\frac{1}{d_o} + \frac{1}{d_i} = \frac{1}{\gamma_f}. \tag{3.4.2}$$

[2] §3.4.5.

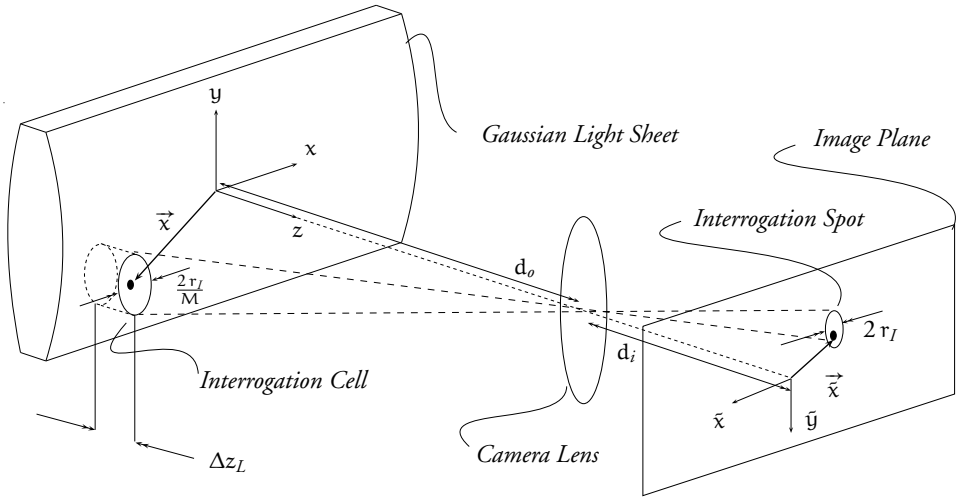

Figure 3.7: *Particle imaging system.*

Throughout, it is assumed the light sheet thickness is much smaller than the distance of particles to their images, i.e. $\Delta z_L \ll (d_o + d_i)$. This implies that perspective projection can be ignored; that is, the tracer particles can be mapped from the light sheet volume to the x-y plane, referred as the *object plane*. The mapping for any function $f(\vec{x})$ is given by its mean over the intensity across the light thickness:

$$\langle f(\vec{x})\rangle_{\mathcal{I}(z)} = \frac{1}{\mathcal{I}_0}\int_{-\Delta z_L/2}^{+\Delta z_L/2} \mathcal{I}(z) f(\vec{x})\, dz. \tag{3.4.3}$$

The lack of perspective projection means that the variation of the magnification $M(z)$ across the light sheet thickness is negligible and can be written as

$$M \equiv M(0) = \frac{d_i}{d_o}. \tag{3.4.4}$$

The purpose of the particle-imaging system is to map the positions of the tracers in the object space (the light sheet) to the recording media image plane.

This transformation involves some loss of data originating from both the imaging and recording processes. The aim is to anticipate the output of the imaging device considering the data loss error. To facilitate this, diffraction theory is used to describe the formation of particle-images and then their diameters are determined as a function of the imaging system parameters.

3.4.1 Scattered Light Field

In this section, the analytical structure of the light field is discussed. Throughout, it is assumed that the light source used for illuminating seeding particles is monochromatic and coherent. In common with the *particle-image* expression, the corresponding tracer particle is sometimes referred as a *particle-source*.

Let us consider the scattered light wave from the particle-source, $\check{a}(\vec{x})$, to have an angular frequency $\check{\omega}$ and complex field amplitude $\mathcal{A}(\vec{x})$. The field can be described by the following equations (Goodman 1968, §3.2)

$$\check{a}(\vec{x}) = \Re\left[\mathcal{A}(\vec{x})\, e^{-\imath\check{\omega}t}\right], \tag{3.4.5a}$$

$$\mathcal{A}(\vec{x}) = \mathcal{A}_0(\vec{x})\, e^{-\imath\check{\varphi}(\vec{x})}; \tag{3.4.5b}$$

where $\mathcal{A}_0(\vec{x})$ and $\check{\varphi}(\vec{x})$ are a non-imaginary amplitude and phase respectively.[3] In this context, it is the time-invariant part of the wave, the complex field amplitude, which is of interest and which satisfies the Helmholtz equation

$$(\nabla^2 + \check{k}^2)\,\mathcal{A}(\vec{x}) = 0, \tag{3.4.6}$$

where $\check{k}$ is the wave number, ordinarily related to the wavelength $\check{\lambda}$ and group speed $\check{c}$ by

$$\check{k} = 2\pi/\check{\lambda} = 2\pi\check{\omega}/\check{c}. \tag{3.4.7}$$

3.4.2 Diffraction Pattern

In spite of the geometrical optics prediction, typical particle-images on a recording medium plane are *not* regions with sharp borders that are well-separated from

[3] To distinguish between light field and sound field, the parameters for light waves are marked by check signs ($\check{}$).

the background; instead, they fade out to it in the form of fringes. This can be explained by *Huygens's principle* founded on the wave nature of light.

Particle-images can be thought of as a colony of diffraction patterns, produced by light waves scattered from the tracer particles, which are incident on the imaging system aperture. Depending on the distance of the tracer particle from the aperture d_o, the distance of the aperture to the image plane d_i, the size of the aperture (camera lens diameter) D_L, and the wavelength of the scattered light $\check{\lambda}$, the produced diffraction pattern can be grouped into different regimes. The regimes can be specified by a dimensionless quantity known as the *Fresnel number*:

$$\mathcal{N}_F = \frac{{D_L}^2}{4\,\check{\lambda}\,d_o}. \tag{3.4.8}$$

Generally, in a PIV experiment, the Fresnel number is much smaller than unity,

$$\mathcal{N}_F \ll 1. \tag{3.4.9}$$

This means that the object distance d_o is much greater than the aperture size, implying that both the incident and diffracted light waves are effectively planar. Such a regime is known as *Fraunhofer* or *far-field diffraction*.

The diffraction pattern of a particle-image can be treated as a two-dimensional distribution of irradiance[4] in the image plane. In the case of a monochromatic field, the irradiance distribution is simply the square of magnitude of the corresponding complex amplitude,

$$\tilde{\mathcal{I}}(\vec{\tilde{x}}) = |\mathcal{A}(\vec{\tilde{x}})|^2. \tag{3.4.10}$$

The form of the irradiance distribution can be determined by the diffraction pattern regime and the aperture properties. For a common PIV set-up, the diffraction pattern, as mentioned earlier, is of the Fraunhofer type and the camera lens is a circular aperture. Bearing these in mind, and using the *Kirchhoff-Fresnel formula*, which is a precise mathematical extension of Huygens's principle, it can be shown that the irradiance distribution of the particle-images takes the form of an *Airy pattern* (Hardy and Perrin 1932, §60). This pattern is expressed by the

[4]Sometimes *intensity* is used as a synonym of *irradiance* or *illuminance* . As discussed in Fowles (1975, §7.2), the word 'intensity' is not technically correct in this context. Hence, unlike the other resources, usage of the expression *image intensity field* in this work is avoided and substituted by *irradiance distribution*.

Airy function which in the polar co-ordinate system of the particle-image is:

$$\tilde{\mathcal{I}}(\tilde{r}) = \tilde{\mathcal{I}}_0 \left(\frac{\mathcal{J}_1(\tilde{r}/\tilde{r}_0)}{\tilde{r}/\tilde{r}_0} \right)^2, \text{ with} \tag{3.4.11a}$$

$$\tilde{\mathcal{I}}_0 = \left(\frac{{D_L}^2}{2\,\tilde{r}_0} \right)^2, \tag{3.4.11b}$$

$$\tilde{r}_0 = \frac{\check{\lambda}\, d_i}{\pi\, D_L}; \tag{3.4.11c}$$

and $\mathcal{J}_1(\tilde{r})$ denotes the first order Bessel function of the first kind. Equation (3.4.11a) describes a circularly symmetrical diffraction pattern consisting of a bright central disk surrounded by a set of dark-light concentric annular bands. The set starts with a dark band and the illuminance of the light bands diminishes rapidly. The bright central area is known as the *Airy disk* (Figure (3.8)).

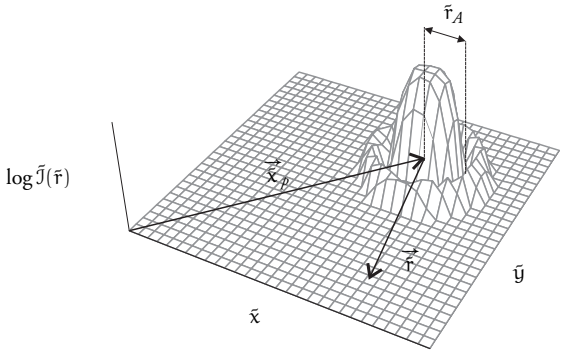

Figure 3.8: *The Airy pattern irradiance distribution in particle-image plane.*

3.4.3 Impulse Response

An imaging device can be considered to be a linear system with both an input and output. To measure the 'quality' of the system, a standard input is needed as a basis for comparison. The standard input normally used is a sudden surge, or *impulse*, with infinite amplitude and zero width. This surge, better known as the DIRAC δ-function, is referred to as the *unit impulse*. The output of a system when the input is a unit impulse is the *impulse response* or *point-spread function* of that system.

The impulse response may be treated as a 'mapper' which transforms the particle-source field amplitude in the object space $\mathcal{A}_o(\vec{x})$ to the particle-image field amplitude in the image plane $\mathcal{A}_i(\vec{\tilde{x}})$. This mapping is given by the superposition integral

$$\mathcal{A}_i(\vec{\tilde{x}}) = \iint_{-\infty}^{+\infty} \mathcal{H}_{\mathcal{A}}(\vec{\tilde{x}}; \vec{x})\, \mathcal{A}_o(\vec{x})\, \mathrm{d}\vec{x}, \tag{3.4.12}$$

where the complex impulse response is denoted by $\mathcal{H}_{\mathcal{A}}(\vec{\tilde{x}}; \vec{x})$. The integral in Equation (3.4.12) is said to be the *convolution* of the functions $\mathcal{H}_{\mathcal{A}}(\vec{\tilde{x}})$ and $\mathcal{A}_o(\vec{\tilde{x}})$ and in a simplified form is shown as

$$\mathcal{A}_i(\vec{\tilde{x}}) = \mathcal{H}_{\mathcal{A}}(\vec{\tilde{x}}) \circledast \mathcal{A}_o(\vec{\tilde{x}}), \tag{3.4.13}$$

where the sign $\circledast$ denotes the convolution operator. Broadly speaking, the more the input $\mathcal{A}_o$ and the output $\mathcal{A}_i$ look like each other, the higher the quality of the imaging system.

In PIV theory, it is assumed that the particle-sources are geometrical points described by the DIRAC δ-function, i.e. the input is a unit impulse. As a consequence, the output is simply the input impulse response of the system. That is, the impulse response for a PIV system is given by the AIRY pattern (3.4.11a) which in its radial form in the coordinate system of the particle-image is given by

$$|\mathcal{H}_{\mathcal{A}}(\tilde{r})|^2 = \frac{\tilde{\mathcal{I}}(\tilde{r})}{\tilde{\mathcal{I}}_0}. \tag{3.4.14}$$

This is an important property of the system which is not often explicitly mentioned in the literature.

Practically, when used in calculations, equation (3.4.14) is substituted by a

Gaussian approximation (Westerweel 1993, §A.4) given by

$$|\mathcal{H}_{\mathcal{A}}(\tilde{r})|^2 \cong e^{-(\tilde{r}/2\tilde{r}_0)^2}. \tag{3.4.15}$$

3.4.4 Source-Image Mapping

It is convenient to break up the mapping of particle-sources from the visualisation volume to the recording plane into a few steps.

The first mapping is from the object space to the image plane using the geometrical optics theory. Consider, for the moment, that the diffraction effect in an imaging system with a converging lens is negligible. Under this condition, the prediction provided by geometrical optics theory is predominant. That is, the particle-image is the exact reproduction of the particle-source, but, magnified and inverted;

$$\tilde{x}_p = -M\,x, \quad \tilde{y}_p = -M\,y, \tag{3.4.16}$$

where $\vec{\tilde{x}}_p$ denotes the position of the particle-image as a geometrical point. A similar relationship exists between the complex field amplitudes (Goodman 1968, §5.3)

$$\mathcal{A}_i^{(G)}(\vec{\tilde{x}}_p) = \frac{1}{M}\,\mathcal{A}_o(\vec{x}), \tag{3.4.17}$$

where $\mathcal{A}_i^{(G)}$ indicates the geometrical prediction.

Finally, to obtain the actual field amplitude of particle-images, the diffraction effect must be incorporated. This is a mapping from the geometrical point form of the particle-image to its diffraction pattern. Goodman (1968) gives the final image output as a convolution of the aperture impulse response and the geometrical prediction. The convolution in our notation can be re-written as

$$\mathcal{A}_i(\vec{x}) = \iint_{-\infty}^{+\infty} \mathcal{H}_{\mathcal{A}}(\vec{r})\,\mathcal{A}_i^{(G)}(\vec{\tilde{x}}_p)\,d\vec{\tilde{x}}_p, \tag{3.4.18}$$

where as illustrated by Figure (3.8),

$$\vec{r} = \vec{x} - \vec{\tilde{x}}_p.$$

Substituting Equation (3.4.17) into the convolution expression gives the source-

image mapping in the following compact form

$$\mathcal{A}_i(\vec{x}) = \frac{1}{M}\,\mathcal{H}_{\mathcal{A}}(\vec{x}) \circledast \mathcal{A}_o(\vec{x}), \tag{3.4.19}$$

The convolution (3.4.19) expresses the final form of the complex amplitude field in the image plane, however, in practice the quantity of interest is the irradiance $\tilde{\mathcal{I}}(\vec{x})$. For any given position $\vec{x}$ in the image plane, the square of the magnitude of the complex amplitude field generated by two particle-images positioned at $\vec{x}_p$ and $\vec{x}'_p$ is

$$|\mathcal{A}_i(\vec{x})|^2 = \iint_{-\infty}^{+\infty}\iint_{-\infty}^{+\infty} \mathcal{H}_{\mathcal{A}}(\vec{x}-\vec{x}_p)\,\mathcal{H}^*_{\mathcal{A}}(\vec{x}-\vec{x}'_p)\,\mathcal{A}_i^{(G)}(\vec{x}_p)\,\mathcal{A}_i^{(G)*}(\vec{x}'_p)\,d\vec{x}_p d\vec{x}'_p. \tag{3.4.20}$$

Assuming the imaging system is set to be in the PIV phase, the source density $\mathcal{N}_S$ is very low. Hence, there is no overlapping between neighbouring particle-images. This implies that, at each position in the image plane, the irradiance value is generated by only one particle-image or

$$\mathcal{A}_i^{(G)}(\vec{x}_p)\,\mathcal{A}_i^{(G)*}(\vec{x}'_p) = |\mathcal{A}_i^{(G)}(\vec{x}_p)|^2\,\delta(\vec{x}_p - \vec{x}'_p). \tag{3.4.21}$$

This greatly simplifies Equation (3.4.20) to

$$|\mathcal{A}_i(\vec{x})|^2 = |\mathcal{H}_{\mathcal{A}}(\vec{x})|^2 \circledast |\mathcal{A}_i^{(G)}(\vec{x})|^2, \tag{3.4.22}$$

which can be written alternatively as

$$\tilde{\mathcal{I}}(\vec{x}) = \frac{1}{M^2}\,|\mathcal{H}_{\mathcal{A}}(\vec{x})|^2 \circledast \mathcal{I}(\vec{x}). \tag{3.4.23}$$

In other words, in the PIV phase, the impulse response of the light intensity distribution is simply the square of the magnitude of the imaging system impulse response.

3.4.5 Resolution Limit of Camera Lens

The Fraunhofer diffraction imposes a resolution limit on the imaging aperture. Optical systems with this limit are said to be *diffraction-limited* or *aberration-free*. According to the *Rayleigh criterion*, the minimum distance between two particle-

images at which they can still be 'resolved' by the camera lens is the radius of the corresponding maximum Airy disk (Hardy and Perrin 1932, §61). This distance is known as the *theoretical resolution limit*.

The Airy disk radius, $\tilde{r}_A$, can be obtained by calculating the first zero of the Bessel function $J_1(\tilde{r}/\tilde{r}_0)$ occurring for $\tilde{r}/\tilde{r}_0 \cong 3.8217$. Applying Equation (3.4.11c), the radius is given by

$$\tilde{r}_A \cong 1.22\,\check{\lambda}\,\frac{d_i}{D_L}. \tag{3.4.24}$$

It is convenient to express this quantity as a pure function of the system parameters. Combining Equations (3.4.1) and (3.4.2), Equation (3.4.24) can be alternatively written as

$$\Delta_L \equiv \tilde{r}_A \cong 1.22\,\check{\lambda}\,(M+1)\,f^{\#}; \tag{3.4.25}$$

where Δ_L denotes the resolution limit of the camera lens and $f^{\#}$ is the *f-number* of the aperture lens defined as

$$f^{\#} = \frac{\gamma_f}{D_L}. \tag{3.4.26}$$

3.4.6 Particle-Image Size

The convolution equation (3.4.19) together with the system resolving limitations can be used to calculate the particle-image dimensions. Adrian and Yao (1985) used a Gaussian approximation for the convolution components—the Airy irradiance distribution and the image predicted by geometrical optics—and obtained the following estimated value for the particle-image radius

$$\tilde{r}_p \cong \left(M^2\,{r_p}^2 + \frac{1}{4}{\Delta_L}^2 + \frac{1}{4}{\Delta_R}^2\right)^{\frac{1}{2}}; \tag{3.4.27}$$

where Δ_R notates the resolution limit of the recording medium.

3.5 Spatial Correlation Theory

The concepts presented in this section are based on appendix A.

3.5.1 Source and Image Densities

Earlier, in §3.2.2, the concepts of source and image densities were introduced. In this section, more accurate definitions for these quantities, as given by Adrian (1984, 1991), are presented.

Consider a cylindrical volume in the particle-source space which is created by the intersection of the illuminating light sheet (of thickness Δz_L) with a circle whose radius is $\tilde{r}_p/M$; i.e., the circle that is produced when a particle-image with a radius given by Equation (3.4.27) is back-projected on to the object space. This cylindrical volume is said to be a *resolution cell* expressed by

$$V_R = \Delta z_L \, \pi \left(\frac{\tilde{r}_p}{M} \right)^2 . \tag{3.5.1}$$

The mean number of particle-sources in a resolution cell is the source density and is given by

$$\mathcal{N}_S = C \, V_R, \tag{3.5.2}$$

where C is the mean number of particle-sources per unit volume.

From the definition of the source density, it can be immediately concluded that the condition for particle-images to be thoroughly separated from each other is that the corresponding particle-sources are laid uniquely within resolution cells. That is, if more than one particle-source shares the same resolution cell their associated particle-images overlap. Applying Equation (3.5.2), the probability of *exactly* k particles being in a volume V_R is given by the Poisson distribution (A.2.16) as

$$p_{k;\mathcal{N}_S} = \frac{{\mathcal{N}_S}^k}{k!} \, e^{-\mathcal{N}_S}. \tag{3.5.3}$$

For $\mathcal{N}_S \gg 1$, the probability $p_{k>1;\mathcal{N}_S}$ becomes significant which means formation of speckle patterns, whilst for $\mathcal{N}_S \ll 1$ one has

$$p_{k;\mathcal{N}_S} \cong \frac{{\mathcal{N}_S}^k}{k!}.$$

implying the phase is particle-image.

By analogy with the resolution cell definition, an *interrogation cell* can be defined as

$$V_I = \Delta z_L \, \pi \left(\frac{r_I}{M} \right)^2 , \tag{3.5.4}$$

which describes a cylindrical volume created by the intersection of the light sheet with a circle whose radius is given by back-projecting an interrogation spot with radius D_I in the image plane. The mean number of tracer particles in an interrogation cell is the image density given by

$$\mathcal{N}_I = C\, V_I. \tag{3.5.5}$$

In the case that $\mathcal{N}_I \gg 1$, the probability $p_{k>1;\mathcal{N}_S}$ is high, meaning that there are many particle-images in each interrogation spot; i.e. the phase is high-density particle-image. On the other hand when $\mathcal{N}_I \ll 1$, the probability $p_{k<1;\mathcal{N}_S}$ is more significant implying the phase is low-density particle-image.

3.5.2 Displacement Field

Assume that the flow under study is described by the velocity field $\vec{v}\left(\vec{x}(t)\right)$. If an ideal tracer particle at time t_i is located at position $\vec{x}(t)$ with velocity $\vec{v}_p\left(\vec{x}(t)\right)$, based on Rule (3.i), at time t_j the particle *displacement field* is given by

$$\vec{d}_{\vec{x};ji} \equiv \vec{d}(\vec{x}; t_i, t_j) = \int_{t_i}^{t_j} \vec{v}_p\left(\vec{x}(t)\right)\, dt. \tag{3.5.6}$$

The displacement field is an 'averaging' over time, which means it does not give any information on the motion of the flow within the averaging time. Thus, there always exists some error ε where

$$|\vec{d}_{\vec{x};ji} - \vec{v}\left(\vec{x}(t)\right)\,(t_j - t_i)| \leqslant \varepsilon, \quad t_i \leqslant t \leqslant t_j. \tag{3.5.7}$$

Needless to say, a PIV experiment only measures the velocity of the flow where the tracer particles are positioned. That is, since the particles are located randomly, the flow can only be probed by random sampling.

3.5.3 Particle-Source Pattern

Particle-sources can be treated as geometrical points randomly distributed in the object space. Assume there are $\mathcal{N}_p$ tracer particles in the flow under investigation and at any time t the particle α is positioned at $\vec{x}_\alpha(t)$. The scattered light intensity, at any point $\vec{x}(t)$ in the object plane, may be described by the Dirac

δ-function as

$$\mathcal{I}(\vec{x}) = \sum_{\alpha=1}^{\mathcal{N}_p} \mathcal{I}(z_\alpha)\, \delta(x - x_\alpha, y - y_\alpha). \tag{3.5.8}$$

This equation can be given in a compact form by

$$\mathcal{I}\left(\vec{x}(t)\right) = \mathcal{I}_0 \left\langle G\left(\vec{x}(t)\right)\right\rangle_{\mathcal{I}(z)}, \tag{3.5.9}$$

where

$$G\left(\vec{x}(t)\right) = \sum_{\alpha=1}^{\mathcal{N}_p} \delta\left(\vec{x}(t) - \vec{x}_\alpha(t)\right). \tag{3.5.10}$$

The dimensionless quantity $G\left(\vec{x}(t)\right)$ is known as the *particle-source pattern*.

For each element t_i of a given time set $\{t_1, t_2, \ldots, t_n\}$, the particle-source pattern has a value $G\left(\vec{x}(t_i)\right)$ which for brevity may be denoted as

$$G_i(\vec{x}) \equiv G_i\left(\vec{x}(t)\right) \equiv G\left(\vec{x}(t_i)\right). \tag{3.5.11}$$

As time passes, from all of the possible patterns (the *ensemble* of patterns), a 'history' is generated which describes a *stochastic process*.[5] We describe the stochastic process of the particle-source patterns as

$$\{G_1(\vec{x}), G_2(\vec{x}), \ldots, G_n(\vec{x})\},$$

or in a compact form as $\{G(\vec{x})\}$, where $G(\vec{x})$ is said to be a *random variable*[6] or a *realisation*.

Let $\vec{s}_{\vec{x};ji}$ indicate the displacement between two points $(\vec{x}, t_i)$ and $(\vec{x}', t_j)$ by

$$\vec{s}_{\vec{x};ji} = \vec{x}'(t_j) - \vec{x}(t_i), \tag{3.5.12}$$

The process $\{G(\vec{x})\}$ may be considered as a chain of events in which each individual random variable $G_j(\vec{x} + \vec{s}_{\vec{x};ji})$ at $(\vec{x} + \vec{s}_{\vec{x};ji}, t_j)$, as an output, is produced by another random variable $G_i(\vec{x})$ at $(\vec{x}, t_i)$, as the input. In order to link these input and output signals, an impulse response $\mathcal{H}_{G_jG_i}(\vec{s}_{\vec{x};ji})$ can be specified and,

[5] §A.4
[6] Definition (A.v)

consequently, each random variable can be written as the following convolution

$$G_j(\vec{s}_{\vec{x};ji}) = \mathcal{H}_{G_jG_i}(\vec{s}_{\vec{x};ji}) \circledast G_i(\vec{s}_{\vec{x};ji}). \tag{3.5.13}$$

Assuming the displacement field to be *local*, i.e. $\vec{d}_{\vec{x};ji} \cong \vec{d}_{ji}$, the impulse response can be expressed as the shift of the input by the local displacement:

$$\mathcal{H}_{G_jG_i}(\vec{s}_{\vec{x};ji}) = \delta(\vec{s}_{\vec{x};ji} - \vec{d}_{ji}); \tag{3.5.14}$$

At any point $\vec{x}$, the data of velocimetry interest to extract from the process $\{G(\vec{x})\}$ is the displacement $\vec{s}_{\vec{x};ji}$. One way to do this is to find out how 'correlated' the random variables $G_i(\vec{x})$ and $G_j(\vec{x} + \vec{s}_{\vec{x};ji})$ are by calculating the *covariance matrix* [7] corresponding to the process $\{G(\vec{x})\}$. Using Equation (A.4.18), the covariance matrix elements for the random variables are given by the following *cross-covariance* [8]

$$\begin{aligned}\mathcal{R}_{G_jG_i}(\vec{s}_{\vec{x};ji}) &= \mathrm{cov}\{G_i(\vec{x}), G_j(\vec{x} + \vec{s}_{\vec{x};ji})\} \\ &= \mathcal{E}\{\Big(G_j(\vec{x}) - \mathcal{E}\{G_j(\vec{x})\}\Big)\ \Big(G_i(\vec{x} + \vec{s}_{\vec{x};ji}) - \mathcal{E}\{G_i(\vec{x} + \vec{s}_{\vec{x};ji})\}\Big)\},\end{aligned} \tag{3.5.15}$$

where $\mathrm{cov}\{\,,\,\}$ stands for the *covariance operator* [9] and the *expectation value* [10] is denoted by $\mathcal{E}\{\}$. Substituting Equation (3.5.13) into the cross-covariance relation yields

$$\begin{aligned}\mathcal{R}_{G_jG_i}(\vec{s}_{\vec{x};ji}) &= \mathrm{cov}\{G_i(\vec{x}), \mathcal{H}_{G_jG_i}(\vec{x} + \vec{s}_{\vec{x};ji}) \circledast G_j(\vec{x} + \vec{s}_{\vec{x};ji})\} \\ &= \mathcal{H}_{G_jG_i}(\vec{s}_{\vec{x};ji}) \circledast \mathrm{cov}\{G_i(\vec{x}), G_j(\vec{x} + \vec{s}_{\vec{x};ji})\} \\ &= \mathcal{H}_{G_jG_i}(\vec{s}_{\vec{x};ji}) \circledast \mathcal{R}_{G_iG_i}(\vec{s}_{\vec{x};ii}),\end{aligned} \tag{3.5.16}$$

Defining the *auto-covariance* [11] values as the diagonal members of the covariance

[7] §A.4.3.
[8] §A.4.2.1.
[9] §A.4.1.2.
[10] §A.2.3.
[11] §A.4.1.3.

matrix denoted by

$$\mathcal{R}_{G_i}(\vec{s}_{\vec{x};i}) \equiv \mathcal{R}_{G_iG_i}(\vec{s}_{\vec{x};ii}),$$

the cross-covariance can be alternatively given by

$$\mathcal{R}_{G_jG_i}(\vec{s}_{\vec{x};ij}) = \{\mathcal{H}_{G_jG_i} \circledast \mathcal{R}_{G_i}\}(\vec{s}_{\vec{x};i}). \tag{3.5.17}$$

That is, the non-diagonal members of the covariance can be generated by knowing the diagonal members. Using Equation (3.5.17), it can be shown (Adrian 1988*b*) that the covariance matrix elements are of the form

$$\mathcal{R}_{G_jG_i}(\vec{s}_{\vec{x};ji}) = C\,\delta(\vec{s}_{\vec{x};ji} - \vec{d}_{ji}). \tag{3.5.18}$$

Each element of the covariance matrix given for a particle-source pattern describes a point in the displacement-probability space; i.e. $\mathcal{R}_{G_jG_i}(\vec{s}_{\vec{x};ji})$ represents the likelihood that the displacement of particles from the realisation $G_i(\vec{x})$ to the realisation $G_j(\vec{x} + \vec{s}_{\vec{x};ji})$ is equal to to $\vec{d}_{ji}$. The set of these points is referred to as the *correlation plane*.

The covariance matrix in Equation (3.5.15) describes a correlation plane with one infinite sharp peak and zero elsewhere. In the velocimetry of a particle-source pattern process by an imaging system, the aim is to 'measure' the correlation plane of the process. That is, to find the correlation plane corresponding to particle-images. Due to the limiting errors in the imaging system, discussed in §3.4.3, the measured correlation plane contains some noise and has a wider and shorter peak. In the next section the formulation of the measured correlation plane is presented.

3.5.4 Particle-Image Pattern

Earlier, in §3.4.4, the impulse response of light intensity was described. The impulse response may be employed to derive irradiance distribution from light intensity distribution. Combining Equations (3.4.23) and (3.5.9), the following convolution exists

$$\tilde{\mathcal{J}}(\vec{\xi}) = \tilde{\mathcal{J}}_0\,|\mathcal{H}_{\mathcal{A}}(\vec{\xi})|^2 \circledast \left(\frac{1}{M^2}\,\langle G(\vec{x})\rangle_{\mathcal{J}(z)}\right). \tag{3.5.19}$$

By analogy with the particle-source pattern definition, the second part of the convolution is named the particle-image pattern and is given by

$$\tilde{G}(\vec{\tilde{x}}) = \langle G(\tilde{x}, \tilde{y}, z)\rangle_{\mathcal{I}(z)}, \tag{3.5.20a}$$

or, alternatively, in the explicit form of

$$\tilde{G}(\vec{\tilde{x}}) = \frac{1}{\tilde{\mathcal{I}}_0} \sum_{\alpha=1}^{\mathcal{N}_p} \tilde{\mathcal{I}}(z_\alpha)\, \delta(\vec{\tilde{x}} - \vec{\tilde{x}}_\alpha). \tag{3.5.20b}$$

Let $\vec{\tilde{d}}_{ij}$ and $\vec{\tilde{s}}_{\vec{\tilde{x}};ij}$ be, correspondingly, the equivalents of $\vec{d}_{ij}$ and $\vec{s}_{\vec{x};ij}$ in the image plane given by

$$\vec{\tilde{d}}_{ji} = M\,(\hat{x}.\vec{d}_{ji}, \hat{y}.\vec{d}_{ji}), \tag{3.5.21}$$

$$\vec{\tilde{s}}_{\vec{\tilde{x}};ji} = M\,(\hat{x}.\vec{s}_{\vec{x};ji}, \hat{y}.\vec{s}_{\vec{x};ji}), \tag{3.5.22}$$

where $\hat{x}$ and $\hat{y}$ are the unit vectors and . denotes the scalar product operator. Knowing the source-particle pattern form, the covariance matrix of the particle-image pattern process can be obtained (Adrian 1988*b*). The cross-covariance of two realisations $\tilde{G}_i$ and $\tilde{G}_j$ is of the form of

$$\mathcal{R}_{\tilde{G}_j\tilde{G}_i}(\vec{\tilde{s}}_{\vec{\tilde{x}};ji}) = \frac{\tilde{C}_O}{M^2}\, \delta(\vec{\tilde{s}}_{\vec{x};ji} - \vec{\tilde{d}}_{ji}), \tag{3.5.23}$$

where $\tilde{C}_O$ is the number of particle-sources per unit area which remain within the light sheet expressed as

$$\tilde{C}_O = C\, M^2\, \Delta z_L\, F_O(\hat{z}.\vec{d}_{ji}). \tag{3.5.24}$$

Here $F_O(\hat{z}.\vec{d}_{ij})$ is the *out-of-plane loss-of-correlation* given by

$$F_O(\hat{z}.\vec{d}_{ji}) = \frac{\left\langle \mathcal{I}(z + \hat{z}.\vec{d}_{ji})\right\rangle_{\mathcal{I}(z)}}{\langle \mathcal{I}(z)\rangle_{\mathcal{I}(z)}}. \tag{3.5.25}$$

Comparing Equations (3.5.18) and (3.5.23) indicates that the 'measured' $\mathcal{R}_{G_jG_i}$, or $\mathcal{R}_{\tilde{G}_j\tilde{G}_i}$, has the same structure as the original $\mathcal{R}_{G_jG_i}$; but mapped within the

imaging system and altered by a constant. The constant involves number of source particle-sources in the illuminated volume and an error originating from particle-sources losing their pairs between the successive realisations.

As the final step in calculating the spatial correlation properties of PIV data, the cross-covariance of the irradiance can be derived using the known cross-covariance of the particle-image pattern. This derivation as given by Adrian (1988*b*) may be written down as

$$\mathcal{R}_{\tilde{\jmath}_j \tilde{\jmath}_i}(\vec{\tilde{s}}_{\vec{\tilde{x}};ji}) = (\tilde{\jmath}_0 \, M \, h_0)^2 \{F_{\mathcal{H}} \circledast \mathcal{R}_{\tilde{G}_j \tilde{G}_i}\}(\vec{\tilde{s}}_{\vec{\tilde{x}};ji}); \tag{3.5.26}$$

with

$$h_0 = \iint_{-\infty}^{+\infty} |\mathcal{H}_{\mathcal{A}}(\vec{x})|^2 \, d\vec{x}, \tag{3.5.27}$$

and

$$F_{\mathcal{H}}(\vec{\tilde{s}}_{\vec{\tilde{x}};ji}) = \frac{\{|\mathcal{H}_{\mathcal{A}}|^2 \circledast |\mathcal{H}_{\mathcal{A}}|^2\}(\vec{\tilde{s}}_{\vec{\tilde{x}};ji})}{h_0^2}, \tag{3.5.28}$$

as the normalised self-correlation peak. Substituting Equation (3.5.23) into (3.5.26) yields

$$\mathcal{R}_{\tilde{\jmath}_j \tilde{\jmath}_i}(\vec{\tilde{s}}_{\vec{\tilde{x}};ji}) = \tilde{C}_O \, \tilde{\jmath}_0^2 \, h_0^2 \, F_{\mathcal{H}}(\vec{\tilde{s}}_{\vec{\tilde{x}};ji} - \vec{\tilde{d}}_{ji}). \tag{3.5.29}$$

In its new form, the correlation is an indirect function of the complex amplitude impulse response. This implies the correlation peak width is proportional to the dimensions of the particle-images.

3.5.5 Interrogation

The PIV correlation theory presented so far describes the displacement of flow within two realisations without any limited spatial boundary. In practice, it is desirable to measure the displacements inside the interrogation cells. To do this, the irradiance field in each realisation is limited to a region of interest defined by a window function.

Like the light sheet intensity profile, described in §3.3.2.2, the typical window functions are of the Gaussian or rectangular box form given by

$$\mathcal{W}(\vec{\tilde{x}}) = \mathcal{W}_0 \, e^{-8(\tilde{x}-\tilde{x}_I)^2/\Delta\tilde{x}_I{}^2 - 8(\tilde{y}-\tilde{y}_I)^2/\Delta\tilde{y}_I{}^2}, \tag{3.5.30}$$

or

$$\mathcal{W}(\vec{\tilde{x}}) = \begin{cases} \mathcal{W}_0 & \text{if} \quad |\tilde{x} - \tilde{x}_I| \leqslant \Delta\tilde{x}_I/2 \wedge |\tilde{y} - \tilde{y}_I| \leqslant \Delta\tilde{y}_I/2 \\ 0 & \text{elsewhere} \end{cases}, \tag{3.5.31}$$

where $(\tilde{x}_I, \tilde{y}_I)$ and $(\Delta\tilde{x}_I, \Delta\tilde{y}_I)$ are, respectively, the centre and dimensions of the interrogation area. For consistency, throughout, the interrogation area is denoted as S_I.

The interrogated irradiance field is defined as

$$I(\vec{\tilde{x}}) = \mathcal{W}(\vec{\tilde{x}})\,\tilde{J}(\vec{\tilde{x}}). \tag{3.5.32}$$

Given

$$I_i(\vec{\tilde{x}}) \equiv I\left(\vec{\tilde{x}}(t_i)\right), \tag{3.5.33}$$

the cross-covariance matrix for $I_i(\vec{\tilde{x}})$ and $I_j(\vec{\tilde{x}})$ over a shift $\vec{s}_{\vec{\tilde{x}};ji}$ is given by

$$\mathcal{R}_{I_j I_i}(\vec{s}_{\vec{\tilde{x}};ji}) = \mathrm{cov}\{I_i(\vec{\tilde{x}}), I_j(\vec{\tilde{x}} + \vec{s}_{\vec{\tilde{x}};ji})\}, \tag{3.5.34}$$

which may be calculated by a similar procedure presented in §3.5.4. Introducing the window function changes the averaging of irradiance distribution, consequently, some new terms appear in the outcome cross-covariance. It is convenient to present the cross-covariance in terms of its ensemble mean and fluctuations by

$$\mathcal{R}_{II}(\vec{\tilde{s}}) = \left\langle \mathcal{R}_{II}(\vec{\tilde{s}}) \right\rangle + \mathcal{R}'_{II}(\vec{\tilde{s}}), \tag{3.5.35}$$

where, for the sake of brevity, the realisation information indices are omitted. In the next section, the ensemble mean covariance is studied in detail.

3.5.6 Analysis Modes

Consider a *frame* is a recording medium at a specific time, and an *exposure* is registering a realisation of the image plane on a frame. PIV data acquisition has the option of recording images with a combination of number of frames and exposures. Depending on this combination, the ensemble mean covariance appeared in Equation (3.5.35) has different forms as presented in this section.

3.5.6.1 Single-Frame, Single-Exposure

While no velocimetry can be carried out in this analysis mode, it includes some components which can be used in the other analysis modes. As there is only one frame, the ensemble mean covariance is, actually, auto-covariance which in its normalised form is known as *auto-correlation*.[12] In this special case, since there is only one realisation, the auto-correlation is a *self-correlation*. Following the notation in Adrian (1988*b*), the auto-covariance $\mathcal{R}_{\mathrm{I}}$ can be decomposed to the following

$$\left\langle \mathcal{R}_{\mathrm{I}}(\vec{s}) \right\rangle = \mathcal{R}_{\mathrm{C}}(\vec{s}) + \mathcal{R}_{\mathrm{F}}(\vec{s}) + \mathcal{R}_{\mathrm{P}}(\vec{s}), \tag{3.5.36}$$

where $\mathcal{R}_{\mathrm{C}}$ stands for the mean background correlation, $\mathcal{R}_{\mathrm{F}}$ is the fluctuation of the background noise and $\mathcal{R}_{\mathrm{P}}$ shows the *self-correlation* peak, also known as the *pedestal* (Figure (3.9)). As expected, the pedestal is located at the origin of the correlation plane.

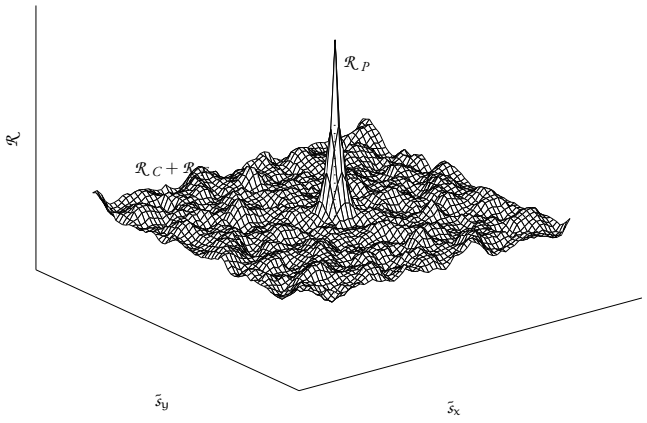

Figure 3.9: *Typical correlation plane for single-frame single-exposure mode.*

[12] §A.4.1.3.

3.5.6.2 Multiple Frames - Single Exposure

The ensemble mean covariance in this mode is cross-covariance or, when it is normalised, *cross-correlation*.[13] Keane and Adrian (1992) gives the double-frames single-exposure ensemble mean cross-covariance as

$$\left\langle \mathcal{R}_{\mathrm{II}}(\vec{\tilde{s}}) \right\rangle = \mathcal{R}_{\mathrm{C}}(\vec{\tilde{s}}) + \mathcal{R}_{\mathrm{F}}(\vec{\tilde{s}}) + \mathcal{R}_{\mathrm{D}}(\vec{\tilde{s}}). \tag{3.5.37}$$

Comparing this covariance to the auto-covariance Equation (3.5.36), the pedestal

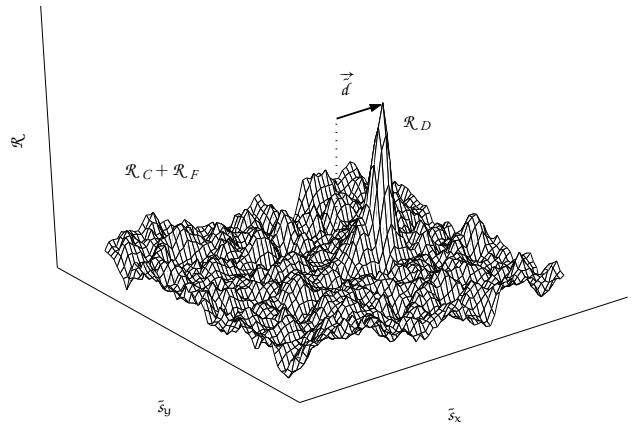

Figure 3.10: *Typical correlation plane for multiple-frames single-exposure mode.*

is replaced by the *displacement-correlation* peak $\mathcal{R}_{\mathrm{D}}$ which contains the information of the mean displacement of the particle images within the interrogation area (Figure (3.10)). The displacement-correlation peak, in its precise form, is given by

$$\mathcal{R}_{\mathrm{D}}(\vec{\tilde{s}}_{\vec{x};ji}) = \tilde{C}_{\mathrm{OI}}(\vec{\tilde{s}}_{\vec{x};ji})\, \tilde{J}_0^2\, h_0^2\, \mathrm{F}_{\mathcal{H}}(\vec{\tilde{s}}_{\vec{x};ji} - \vec{\tilde{d}}_{ji}). \tag{3.5.38}$$

This relationship is comparable to the cross-covariance of the interrogated irradiance fields given in Equation (3.5.29). The only difference is that the latter

[13] §A.4.2.1.

is described by the number of particle-images per unit area which stay within the light sheet *and* the interrogation areas between successive realisations. This quantity, denoted by $\tilde{C}_{OI}$, is referred as the *effective particle-image density* and is given by

$$\tilde{C}_{OI}(\vec{\tilde{s}}_{\vec{x};ji}) = \mathcal{N}_I \, F_I(\vec{\tilde{s}}_{\vec{x};ji}) \, F_O(\hat{z}.\vec{d}_{ji}), \tag{3.5.39}$$

with

$$F_I(\vec{\tilde{s}}_{\vec{x};ji}) = \frac{1}{S_I}\{\mathcal{W}_j \circledast \mathcal{W}_i\}(\vec{\tilde{s}}_{\vec{x};ji}), \tag{3.5.40}$$

which is known as the *in-plane loss-of-correlation*.

3.5.6.3 Single Frame - Multiple Exposures

When, due to hardware limitations, the image recording process is not fast enough to capture each realisation in a separate frame, the resultant data can be analysed in a way which is a combination of the previous modes. The outcome irradiance field, denoted by I_Σ, is a super-position of the individual realisations. As there is only one frame, the displacement can be extracted from an auto-covariance. In the case of a single-frame double-exposures state, the auto-covariance as given by Keane and Adrian (1990) is

$$\left\langle \mathcal{R}_{I_\Sigma}(\vec{\tilde{s}}) \right\rangle = \mathcal{R}_C(\vec{\tilde{s}}) + \mathcal{R}_F(\vec{\tilde{s}}) + \mathcal{R}_P(\vec{\tilde{s}}) + \mathcal{R}_{D^-}(\vec{\tilde{s}}) + \mathcal{R}_{D^+}(\vec{\tilde{s}}). \tag{3.5.41}$$

Here the displacement-correlation peaks appears as $\mathcal{R}_{D^-}$ or $\mathcal{R}_{D^+}$ (Figure (3.11)). This is not a surprising result as the single-frame does not store any temporal information about the super-positioned realisations which causes a *directional ambiguity*.

There are techniques which can be employed to eliminate the directional ambiguity. A common method introduced by Adrian (1986*a*) is referred to as *image-shifting*, where the first realisation is spatially pre-shifted. The pre-shifting is performed by physically displacing the camera by a certain value during the two realisations. This solution also removes the pedestal which may make the extraction of some small displacements hard or impossible.

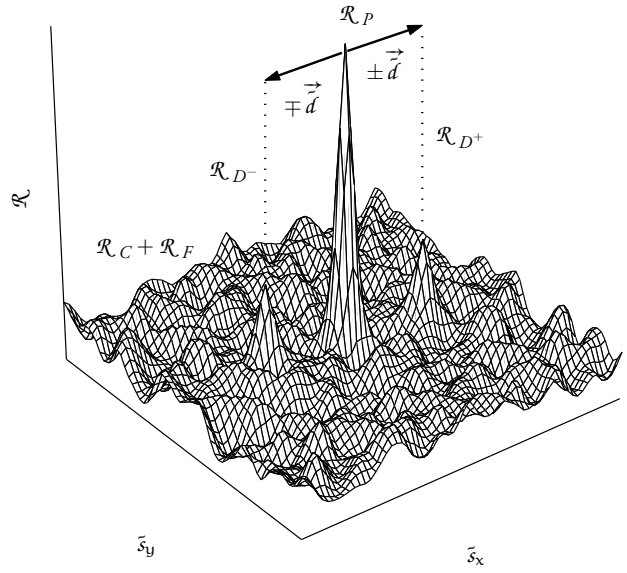

Figure 3.11: *Typical correlation plane for single-frame double-exposure mode.*

3.5.7 Estimation Values

In the spatial correlation theory presented so far, it has been assume that the statistical properties of the PIV data are *known*. In particular, Equation (3.5.34) expresses a cross-covariance value which is calculated by some *presumably known* expectation values:

$$\begin{aligned}\mathcal{R}_{I_j I_i}(\vec{s}_{\vec{x};ji}) &= \mathrm{cov}\{I_i(\vec{x}), I_j(\vec{x}+\vec{s}_{\vec{x};ji})\} \\ &= \mathcal{E}\{\Big(I_j(\vec{x}) - \mathcal{E}\{I_j(\vec{x})\}\Big)\ \Big(I_i(\vec{x}+\vec{s}_{\vec{x};ji}) - \mathcal{E}\{I_i(\vec{x}+\vec{s}_{\vec{x};ji})\}\Big)\}.\end{aligned} \tag{3.5.42}$$

In this equation, the expectation operators perform *ensemble averaging*; that is, averaging over all possible values of the argument. In practice, when observing

a process, there is no pre-knowledge of that process available to describe the features of the process; however, it is possible to 'estimate' the features of the process by the observation itself. This is the fundamentals of the *statistical inference* technique (Hogg and Tanis 1996).

Let the mean of the observed values be called the *observation averaging*. It can be shown (Priestly 1981) the estimated values of the features of a static *ergodic* [14] process can be obtained when the ensemble averaging is substituted by the observation averaging. Implementing this to PIV data, the associated cross-covariance can be estimated when the ensemble averaging is replaced by the *spatial averaging*. The final form of the estimated cross-covariance is given later in §3.6.2.1.

3.6 Digital Analysis

Traditionally, the spatial correlation analysis method was applied to PIV data using hardware-based techniques. These included semi-optical methods, introduced initially for LSV data analysis by Burch and Tokarski (1968) using Young's fringes, and fully-optical methods, as suggested by Coupland and Halliwell (1988). The disadvantages of the opto-mechanical methods, like complexity and temporal consumption, caused it to become obsolete and to be substituted by software-based methods which have been increasingly efficient and economical.

This section contains an introduction to the digital interface to the spatial correlation theory which, in a more general form, is known as *Digital Particle-Image Velocimetry* (*DPIV*).

3.6.1 Pre-Processing

Before the correlation-based digital image evaluation, some verification of the PIV data suitability may be necessary. This includes checking whether there is enough data to produce valid output and mapping the data to the digital space. The PIV data may be directly digitally recorded, or it may be digitised after recording. In both cases the digitisation parameters must be chosen in such

[14] A process is said to be ergodic when, for infinite number of observations, the observation averaging is the same as the ensemble averaging.

a way that the data loss is optimised. The following subsections discuss these aspects of PIV data pre-processing in more detail.

3.6.1.1 Image Sampling

In the first step of digitising the particle-image field, the data space is divided into discrete components named *pixels*. With the sampling impulse response defined as

$$\mathcal{H}_{I_\Delta I}(\vec{\tilde{x}}) = \begin{cases} 1/\Delta_{px}^2 & \text{if} \quad |\tilde{x}| < \Delta_{px}/2 \wedge |\tilde{y}| < \Delta_{px}/2 \\ 0 & \text{elsewhere} \end{cases}, \tag{3.6.1}$$

with Δ_{px} being the size of the pixels, the *discrete irradiance field* can be obtained from the continuous irradiance field:

$$I_\Delta(\vec{x}_\Delta) = \{\mathcal{H}_{I_\Delta I} \circledast I\}(\Delta_{px}.\vec{x}_\Delta), \tag{3.6.2}$$

where $\vec{x}_\Delta = (x_\Delta, y_\Delta)$ is a dimensionless discrete vector. Using this definition, the associated auto- and cross-covariances can be derived as

$$\mathcal{R}_{I_\Delta}(\vec{s}_\Delta) = \{(\mathcal{H}_{I_\Delta I} \circledast \mathcal{H}_{I_\Delta I}) \circledast \mathcal{R}_I\} \left(\Delta_{px}.(\vec{s}_\Delta)\right), \tag{3.6.3}$$

and

$$\mathcal{R}_{I_\Delta I_\Delta}(\vec{s}_\Delta) = F_I(\hat{z}.\vec{d}_{ji})\{(\mathcal{H}_{I_\Delta I} \circledast \mathcal{H}_{I_\Delta I}) \circledast \mathcal{R}_I\} \left(\Delta_{px}.(\vec{s}_\Delta) - \vec{\tilde{d}}\right), \tag{3.6.4}$$

(Westerweel 1993, §3.2), with $\vec{s}_\Delta$ being the dimensionless discrete correlation space.

3.6.1.2 Data Bandwidth

The *bandwidth* of a two-dimensional matrix with elements M_{ij} is defined as the value of $|i - j|$ such that $M_{ij} \neq 0$. In the case where the bandwidth of a matrix is a finite value, that matrix is said to be *band-limited*. According to the *sampling theorem*, a band-limited matrix is reconstructible if it is sampled at a minimum rate of twice of its bandwidth, also known as the *Nyquist rate*.

Assume that the Fourier transform of the irradiance field is given by the matrix $\mathfrak{F}[I]$ where $\mathfrak{F}$ denotes the Fourier transform operator. It can be shown

that $\mathfrak{F}[I]$ is 'nearly' band-limited (Priestly 1981). By sampling PIV data, the irradiance field may be treated as a signal which is reconstructed in the discrete form. The sampling rate, at which the data can be recovered, may be determined by the bandwidth of $\mathfrak{F}[I]$.

Westerweel (1993, §3.5) gives the bandwidth of the PIV imaging system as

$$W_P \cong \frac{0.86}{\tilde{r}_A}, \tag{3.6.5}$$

where $\tilde{r}_A$ is the Airy disk radius given by Equation (3.4.24). Since the radius of the particle-image, as expressed by Equation (3.4.27) is larger than $\tilde{r}_A$, W_P acts like an upper limit for the bandwidth of $\mathfrak{F}[I]$, which is the PIV data bandwidth. According to this, for a typical imaging system, a data sampling rate of 64 mm^{-1} is quite sufficient.

3.6.1.3 Quantisation

While data sampling converts the argument of the irradiance $I(\tilde{x})$ to a discrete value, *quantisation* digitises the value of the irradiance itself. The digitisation is a mapping from real values to some limited integers, also known as number of colors.

Quantisation is an irreversible mapping which adds some noise to the output data. It has been shown (Westerweel 1993, §3.3) that the noise produced by an 8-bit quantiser is negligible. That is, digitising the irradiance field to an image of 256 colors—which is not necessarily, but typically, in gray-scale—preserves the data for processing.

3.6.1.4 Valid-Data Yield

An inappropriate value of the effective particle-image density $\tilde{C}_{OI}$, described by Equation (3.5.39), can cause a noise peak in the correlation plane which is stronger than the displacement peak. Introducing the quantity *valid-data yield* helps to optimise the value of $\tilde{C}_{OI}$.

Similar to the discussion in §3.5.1, the probability of finding *exactly* k particles in an interrogation area may be written as

$$p_{k;\mathcal{N}_{OI}} = \frac{\mathcal{N}_{OI}{}^{k}}{k!}\, e^{-\mathcal{N}_{OI}}, \tag{3.6.6}$$

where $\mathcal{N}_{OI}$, which could be non-integer, is the effective number of particle-image pairs per interrogation area given by

$$\mathcal{N}_{OI} = \tilde{C}_{OI} S_I. \tag{3.6.7}$$

Assume k' is the number of particle-image pairs per interrogation area that is sufficient to remove the majority of the noise peak in the correlation plane. The valid-data yield is defined as the probability of having k' or more particle-image pairs in an interrogation area and is given by [15]

$$\Gamma_{k'}(\mathcal{N}_{OI}) \equiv p_{k \geqslant k'; \mathcal{N}_{OI}} = 1 - \sum_{k=0}^{k'} p_{k; \mathcal{N}_{OI}}. \tag{3.6.8}$$

Figure (3.12) shows some different values of $\Gamma_{k'}(\mathcal{N}_{OI})$. It can be seen when the

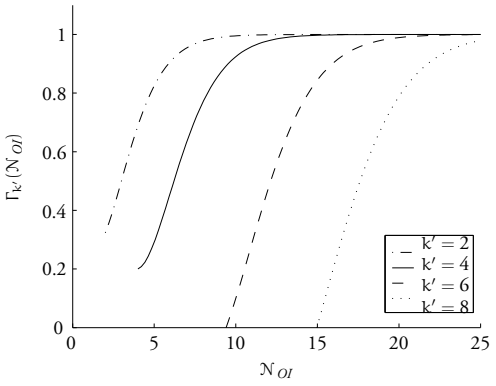

Figure 3.12: *Some values of valid-data yield.*

effective number of particle-image pairs per interrogation area is approximately between 10 and 15, the probability of finding at least 4 particle-image pairs per interrogation area ($k' = 4$) is almost 1. Choosing $\mathcal{N}_{OI}$ to be a larger number causes overlapping of particle-images and should be avoided.

[15] Westerweel (1993, § 3.6.4) gives the valid-data yield, in our notation, as $\Gamma_{k'}(\tilde{C}_{OI})$. This cannot be correct as the argument of the valid-data yield function must be a dimensionless number.

To summarise, setting the interrogation area to have, roughly, 10-20 particle-image pairs is necessary to reduce the noise in the correlation plane.

3.6.2 Data Processing

3.6.2.1 Implementing Estimation

Given the discrete irradiance field described by Equation (3.6.2) and following the arguments presented in §3.5.7, in this section the estimation value of the cross-covariance of discrete PIV data is presented.

Consider two interrogation areas $I'_\Delta(\vec{x}_\Delta)$ and $I''_\Delta(\vec{x}_\Delta)$ with the same size of $N \times N$ pixels. Given that the spatial average of discrete irradiance is

$$\bar{I}_\Delta \equiv \langle I_\Delta(\vec{x}_\Delta)\rangle = \frac{1}{N^2}\sum_{x_\Delta=1}^{N}\sum_{y_\Delta=1}^{N} I_\Delta(\vec{x}_\Delta), \tag{3.6.9}$$

it can be seen that the the mean value is the same for all realisations:

$$\langle I'_\Delta(\vec{x}_\Delta)\rangle = \langle I''_\Delta(\vec{x}_\Delta)\rangle = \bar{I}_\Delta. \tag{3.6.10}$$

The cross-covariance of the two realizations $I'_\Delta(\vec{x}_\Delta)$ and $I''_\Delta(\vec{x}_\Delta)$ over a shift $\vec{s}_\Delta$ can be estimated as

$$\hat{\mathcal{R}}_{I'_\Delta I''_\Delta}(\vec{s}_\Delta) = \frac{1}{N^2}\sum_{x_\Delta=1}^{N}\sum_{y_\Delta=1}^{N}\left(I_\Delta(\vec{x}_\Delta)-\bar{I}_\Delta\right)\left(I_\Delta(\vec{x}_\Delta+\vec{s}_\Delta)-\bar{I}_\Delta\right), \tag{3.6.11}$$

where subtracting the mean values removes the background noise values $\mathcal{R}_C$ and $\mathcal{R}_F$ discussed in §3.5.6 (Westerweel 1997). The estimated cross-correlation is given by

$$\{I'_\Delta \star I''_\Delta\}(\vec{s}_\Delta) = \frac{\hat{\mathcal{R}}_{I'_\Delta I''_\Delta}(\vec{s}_\Delta)}{\hat{\mathcal{R}}_{I'_\Delta I''_\Delta}(0)}, \tag{3.6.12}$$

where the sign $\star$ denotes the correlation operator.

3.6.2.2 DFT-based Correlation

The digital calculation of the measured discrete correlation plane, given by Equation (3.6.11), is computationally intensive and, in practice, when the calculation

is needed to be repeated many times, is not functional. One way to overcome this problem is to perform the computations in the frequency domain, where the processing is less expensive, by making use of *Discrete Fourier Transforms* (*DFT*).

Using the *cross-correlation theorem*, Equation (3.6.12) can be alternatively written as

$$\{I'_\Delta \star I''_\Delta\}(\vec{s}_\Delta) = \mathfrak{DFT}^{-1}\left[\mathfrak{DFT}\left[I'_\Delta\right]\,\mathfrak{DFT}\left[I''_\Delta\right]\right](\vec{s}_\Delta), \tag{3.6.13}$$

where $\mathfrak{DFT}$ denotes the discrete fourier transform.

Usually, the DFT algorithm used in computations is the classical *Fast Fourier Transform* (*FFT*) method introduced by Cooley and Tukey (1965). The algorithm reduces the processing for an interrogation area of $N \times N$ pixels by a factor of $2\log_2(N)/N^2$. One disadvantage of the classical FFT is that it is only efficient when N is a power of 2,imposing restrictions on the interrogation area size. However, there are many other alternative algorithms (Press et al. 1992, Chapter 12) which can lessen the restrictions and increase the interrogation area size choice.

3.6.2.3 Sub-Pixel Peak Detection

The information stored in the discrete correlation plane, given by $\{I'_\Delta \star I''_\Delta\}(\vec{s}_\Delta)$, allows the position of the displacement peak to be determined with a resolution of less than a pixel. In fact, since the correlation peak always covers more than one discrete unit in the correlation plane (Westerweel 1997), the displacement peak can be detected with sub-pixel accuracy. Based on this idea, Willert and Gharib (1991) introduced the sub-pixel peak detection theory by interpolation which is essential for calculating second order quantities, e.g. vorticity or pressure.

Chapter 4

Acoustic Velocimetry Using Particle-Imaging

Everything you can imagine is real.

Pablo Picasso

Laser velocimetry methods are ordinarily applied to fluid flows under no or negligible external forces. Consequently, when implemented on sound fields, PIV principles should be validated in order to meet the new conditions. This chapter examines aspects of PIV theory and discusses the limitations of PIV when applied to sound fields.

4.1 Acoustic Velocimetry Techniques

Unlike the scalar quantities associated with fluids in sound fields, particularly pressure and temperature, measurement of acoustic velocity vectors is not straightforward. Figure (4.1) shows the most common acoustic velocimetry techniques classified in terms of their level of intrusion during a measurement. The techniques are described briefly in this section.

4.1.1 Intrusive Techniques

In the late 19th century, Rayleigh described a system for measuring acoustic velocity (Rayleigh 1945, §253b). After observing the torque that a non-symmetrical

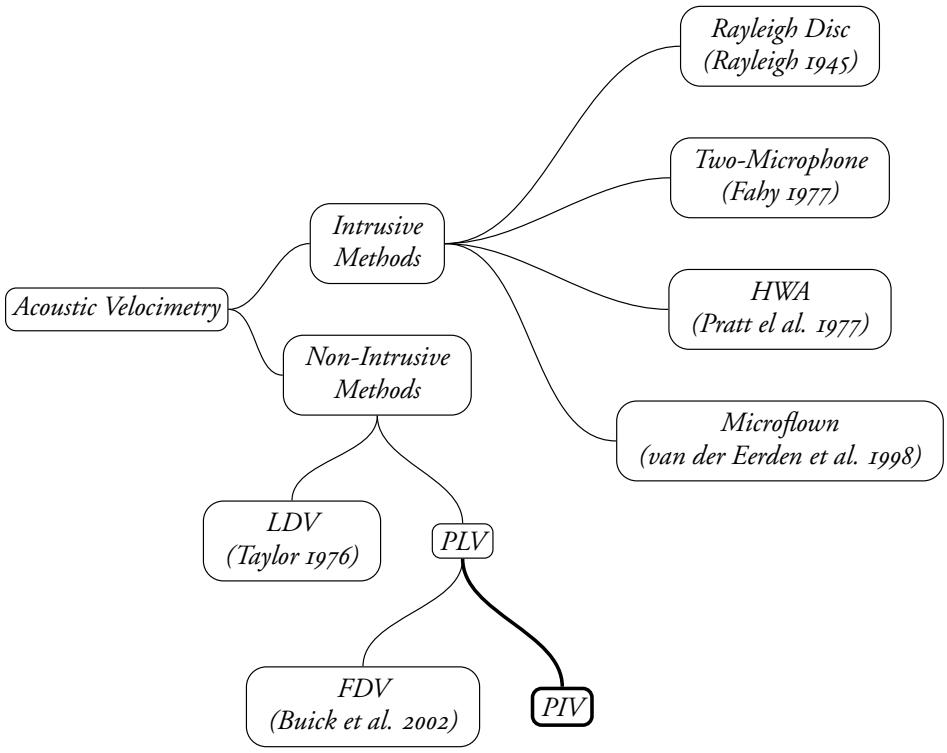

Figure 4.1: *Acoustic velocimetry techniques are grouped according to intrusiveness.*

obstacle of appropriate dimensions experiences in a sound field, Rayleigh suggested using the deviation of a disc floating in a fluid from its equilibrium position to calculate the acoustic velocity of the fluid. The technique, which is referred to as the *Rayleigh disc*, has now been consigned to history and is no longer in use.

One way to measure acoustic velocity vectors is to calculate them from scalar quantities which can be measured more easily. For example, a *two-microphone* method may be applied to extract velocity from pressure (Fahy 1977).

Thermo-electric methods like *Hot-Wire Anemometry* (*HWA*) (Pratt et al. 1977) or *Hot-Film Anemometry* (*HFA*) offer a better accuracy at the expense of a more complicated set-up. The *Microflown* (van der Eerden et al. 1998), which

is based on a thermo-electric structure, is convenient to use but has an upper limit for velocity measurement which is usually lower than the range of interest in acoustic studies.

Because of their physical presence in a sound field, and because their dimensions are not negligible when compared to the wavelength of the sound field, all of the devices used in the techniques mentioned so far have the disadvantage of being intrusive in nature.

4.1.2 Non-Intrusive Techniques

As they are optically based, the laser velocimetry techniques inherit the characteristic of non-, or at least low-, intrusion. Of these, LDV (LDA) and PLV are of special interest.

Taylor (1976) was the first to apply LDV to resonant tubes. The technique involves measuring acoustic velocity by the Doppler shift of waves scattered from tracer particles within small volume found by the intersection of two laser beams. The technique is now well-established and widely used; however, it suffers from the lack of a whole-field feature.

The use of PLV in the study of sound fields has only recently taken off due to previous limitations in capturing images of high-speed flows. The applications of this technique in sound fields may be grouped according to the type of fluid markers used in the measurements.

Fluorescent Dye Velocimetry (FDV) is a PLV-based technique in which dye is used as the molecular marking (§3.2.1) for fluid visualisation (Buick et al. 2002). The method has been applied successfully to acoustic streaming measurements. In comparison to PIV, FDV has the advantage of eliminating the interaction between sound field and particulate fluid markers (§4.4.2); however, there are limitations in applying dye to the fluid under investigation.

Using particulate marking in PLV sound field measurements actually involves acoustic PIV, which is the focus of this chapter.

4.2 Acoustic PIV Applicability

Investigation of the limitations of applying PIV to sound fields may be implemented in two parts. First, the restrictions of PIV as an existing technique is presented. This includes positioning the spatial and temporal ranges of PIV in

the framework of sound fields. Later, in §4.4, the effects of the presence of sound fields in PIV measurements are discussed.

4.2.1 PIV Ranges

A detailed description of spatial resolution of particle-images is given in §3.4. At the time of this study, a typical CCD camera has a resolution of the order of 1000×1000 pixels together with the pixel spacing $\Delta_R \lesssim 10$ μm. Given some rough values for the laser wavelength $\lambda\!\!\!^{-} \approx 500$ nm, magnification $M \approx 2$, f-number $f^{\#} \approx 1$ and applying Equation (3.4.27) it may be seen that a 10 μm displacement is mapped to almost 3 pixels. The associated uncertainty is approximately 1 μm.

For improving the spatial resolution of PIV down to micron and sub-micron level, some substantial work has been carried out leading to a method known as *Micron-resolution PIV* (*micro-PIV* or μ*PIV*) introduced by Meinhart et al. (1999). Their μPIV set-up could map a 200 nm displacement to almost 3 pixels (spaced by 6.8 μm) with an uncertainty of about 53 nm. The technique requires sub-micron seeding particles for tracing the flow faithfully and sub-micron width of the illuminating light sheet for avoiding out-of-the-plane motions.

The temporal resolution of a PIV set-up depends, at least, on the following parameters:

> **Illumination.** Intensity of illumination, duration of each illumination and time separation between illuminations.
>
> **Recording.** Sensitivity of recording medium, duration of each recording and time separation between recordings.
>
> **Synchronisation.** The duration of each illumination and each recording together with the corresponding time separations must be matched.

Of these, the right temporal parameters of the recording parameters seems to be harder to achieve. Recent advances in digital imaging has eliminated a big part of this problem by the use of interline CCD chips, allowing recordings with a time separation of the order of nano-seconds. However, the technology still suffers from a lack of flexibility in recording durations. This deficiency may be covered by taking advantage of the more flexibility available in the duration

of illuminations. The limitation of this method is determined by the trade-off between the flexibility of illumination duration and illumination intensity; that is, shorter illumination durations may be reached at the expense of lower illumination intensity.

4.2.2 Sound Field Ranges

One feature of acoustical phenomena is that their characteristic quantities have a broad range. In particular, this may involve the orders of 1 Hz to 10^8 Hz in the frequency domain while, in different media and depending on the pressure level, the acoustic displacement of interest could vary from 10^{-8} m to 10^{-2} m. This makes the development of a versatile measurement system a challenging task.

Sound fields in the linear regime simply involve *acoustic motion*, that is, the motion of the fluid in the field is directly generated by the sonic source. As the Reynolds number of the fluid—identified by the ratio of the inertial force to the viscous force—gets higher values, the fluid transits to the non-linear regime. The fluid in the non-linear regime may be purely in the acoustic motion phase, as when energy is transferred to the higher modes, or it could transit to the *hydrodynamic motion* where secondary flows are formed as a result of time-averaged fluctuations with a non-zero mean. These hydrodynamic motions are mainly known as *acoustic streaming* (Nyborg 1965; Lighthill 1978) or *steady streaming*.[1]

Figure (4.2) illustrates sound field ranges in the frequency and space domains in comparison with the PIV ranges discussed previously. The sound field ranges are grouped into acoustic and hydrodynamic motions and the ranges of each group, as explained later, are presented based on the corresponding *characteristic* parameters. It is assumed that the PIV measurements sample the sound field under investigation at a rate of ~ 10 in space and time. Hence, as shown in the figure, the 'applicable' PIV ranges are smaller than their actual values by one order.

The characteristic frequency and displacement of acoustic motions is essentially the frequency and amplitude of the associated oscillatory motions. In air, typical amplitudes of linear oscillatory motions with 100 to 200 dB SPL ($\mathcal{P}_{\text{ref}} = 20$ μPa) and a frequency range of 1 to 2 kHz is reported to be of the

[1] Riley (2001) suggests the term 'steady streaming' as an alternative to 'acoustic streaming'. This is due to the fact that the associated phenomenon involves incompressible flows, while, 'acoustic streaming' implements compressibility of the fluid.

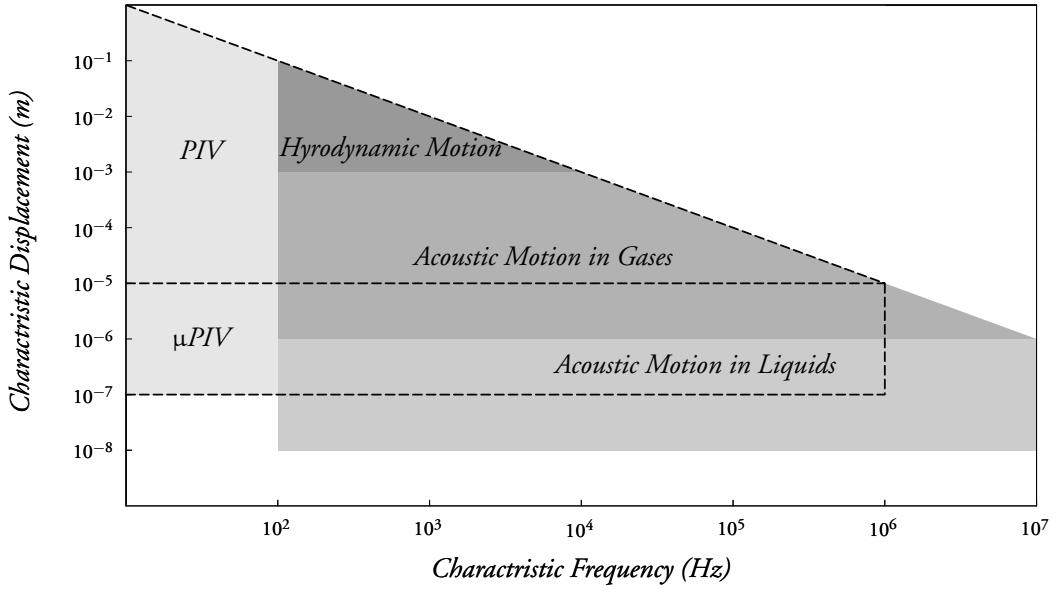

Figure 4.2: *A rough illustration of acoustic PIV ranges based on the characteristic frequency and displacement of the fluid. The product of the characteristic parameters at each point gives the corresponding velocity amplitude. It is assumed that the PIV (μPIV) measurements sample the fluid motion at a rate of* $\sim$ 10 *and the cut-off velocity of the fluid is around* 10 *m/s. The dashed lines represent the PIV (μPIV) borders.*

order of sub-millimeter (Hann and Greated 1997a,b). Thus, acoustic motion is, at least in some regions, measurable by PIV. In contrast, based on Vignola et al. (1991), amplitudes in water with 180 dB SPL ($\mathcal{P}_{\text{ref}} = 1$ μPa) at a frequency of $\sim$ 2 kHz are of much lower sub-micron values which are quite out of the PIV borders. Nevertheless, it seems to be possible potentially to apply μPIV to acoustic motions in liquids. It should be noted that applying μPIV to sound flow passages of dimensions much greater than the micron order cannot yield relatively whole-field results, being closer to a point measurement technique.

Increasing the sound intensity level in order to gain higher amplitudes of acoustic motions may cause two undesirable effects. First, this increments the acoustic velocity which demands higher temporal PIV sampling and, conse-

quently, shrinks the PIV ranges. Secondly, increasing the amplitude in this way can create some unwanted non-linear events such as distortion or streaming.

In hydrodynamic motions, the characteristic parameters are a few orders greater than the ones of acoustic motions. Acoustic streaming velocities are normally of the order of $\lesssim$ 1 cm/s and rarely up to a few meters per second (Akulichev 1971). This well-fits the hydrodynamic motions within the PIV ranges.

4.3 Previous Studies On Acoustic PIV

Based on the discussed acoustic ranges, the applications of PIV to sound fields can be mainly divided into the measurement of acoustic and hydrodynamic motions. The following is an overview of these applications where some of them are also covered in Campbell et al. (2000).

4.3.1 Acoustic Motions

Due to the restrictions in applying PIV to acoustic motions, namely difficulties associated with capturing images rapidly enough to track fast tracer particles, the literature on this topic is quite sparse.

In the first attempt to use PIV to study a sound field, due to the lack of illumination intensity for short exposures and/or the difficulty in sending illumination pulses fast enough, the image recording process was carried out over a few acoustic cycles (Hann 1995; Hann and Greated 1997a,b). The acquired data was a set of *streaks* rather than particle-images and consequently required a slightly different data analysis method to that used in general PIV. As the image recoding process takes more than half of an acoustic cycle, no phase information can be obtained using this method.

The direct measurement of acoustic displacement in air using real particle-imaging was introduced by Blackshire (1997) and later extended by Humphreys Jr et al. (1998). The output of the measurement is the 'absolute displacement' of fluid particles from their equilibrium which is *not* the same as the 'instantaneous displacement' that leads to velocimetry. The technique is based on two independent laser sources, with a static delay of half an acoustic cycle, which are synchronised with the sound field by a microphone trigger. The displacement data is extracted from a single-frame double-exposure recording followed

by auto-correlation analysis. The advantage of this system is that it extracts phase information as well as the amplitude and direction of acoustic displacement.

4.3.2 Hydrodynamic Motions

The application of PIV to the study of different types of acoustic streaming, that involve velocities which are much lower than the velocities associated with typical acoustic oscillatory motions, demands less challenging conditions.

Initiated by Sharpe et al. (1988), a considerable amount of research has been undertaken on PIV applied to hydrodynamic motions; namely, Rayleigh acoustic streaming in air (Hann and Greated 1997c; Rockliff et al. 2000; Rockliff and Greated 2001; Skulina et al. 2003; Johansson et al. 2003) and Eckart acoustic streaming in water (Cosgrove et al. 2001). Many of these studies involve double-frame single-exposure recordings with an exposure time of the order of a few tens of milliseconds or more.

4.3.3 Novelty

The use of PIV in the study of sound fields has provided a better qualitative understanding of acoustic behaviour, particularly, in complex geometries. In addition, quantitative results such as standing wave pattern and the impedance of low-speed flow passages have been achieved.

However, from the flow visualisation point of view, not much remarkable progress can be seen in recent works. Figure (4.3) compares recent visualisations with some similar cases performed in the 1930s. The lack of progress can be seen particularly in the measurement of high-speed oscillatory motion where no substantial work has been reported on the capturing of particle-images within *one* acoustic cycle.

4.4 Effect of Sound Fields On PIV Measurements

In its general form, PIV is known as a non-intrusive technique, as has been well-verified through applications such as the measurement of turbulent flows. However, the presence of a sound field in the fluid under investigation introduces various new phenomena which may alter the fundamental assumptions that PIV

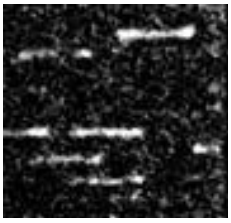

a) *Brandt and Hiedemann (1936).*

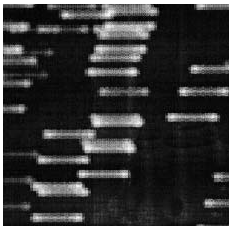

b) *Hann (1995).*

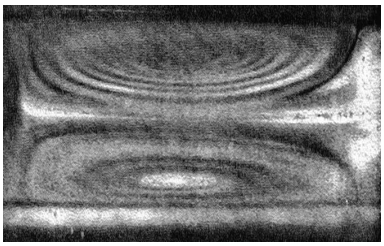

c) *Andrade (1931).*

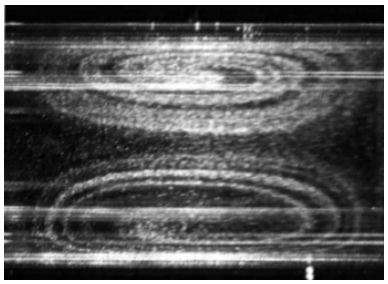

d) *Rockliff (2002).*

Figure 4.3: *A comparison between flow visualisation on PIV measurements in sound fields in the 1930s to similar studies in recent research. Figures (a) and (b) show the visualisation of acoustic oscillatory motion over a few cycles. Figures (c) and (d) correspond to visualisation of hydrodynamic motion generated by Rayleigh streaming.*

provides a non-intrusive measurement (§3.2). Accordingly, a careful consideration of any acoustical effect on the laser velocimetry configuration must be taken into account.

To study the level of intrusion incurred during acoustic PIV measurements, it is convenient to decompose a PIV measurement into sound field, light field and tracer particles components, as illustrated in Figure (4.4). Under this assumption, the measurement can be considered non-intrusive provided that none of these components interact with each other or if the interaction is negligible. The amplitudes of the interactions depend crucially on the characteristics of the sound field, like frequency and sound intensity, and the material and optical features of the fluid and tracer particles. Hence, the amount of intrusion during an acoustic PIV measurement is very specific to that measurement. The following is a discussion of the common interactions which stop acoustic PIV measurements from being completely non-intrusive or providing reliable output data.

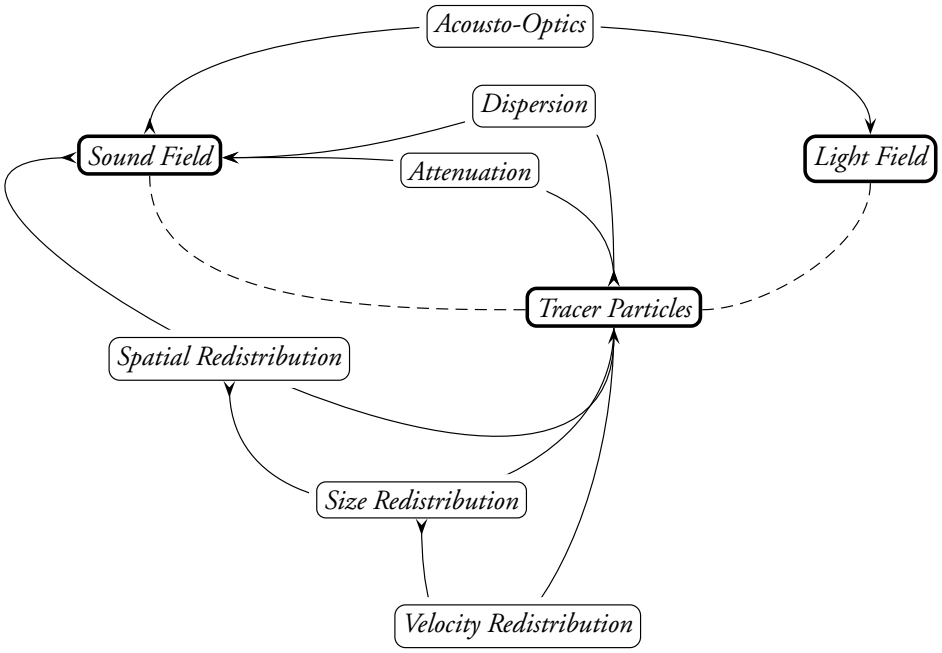

Figure 4.4: *The intrusion parameters in acoustic velocimetry using particle-imaging.*

4.4.1 Sound Field – Light Field Interactions

The presence of sound waves in a medium is a source of optical inhomogeneity which makes the light scattered from an object in the medium experience a gradient of the refractive index. This causes the apparent optical properties of the object, such as the position, to differ from the exact values.

In the case of ultra-sonic waves, the interaction between sound and light fields can be explained by *acousto-optics* (Sapriel 1979). In acoustic LDV measurements, the acousto-optical effect has been studied for propagating (Jack et al. 1998) and standing sound waves (Jack et al. 1999) in water. It has been shown that sound waves may intrude the Doppler signal in a non-negligible way.

The aero-optical effect on the distortion of PIV data has been pointed out by Elsinga et al. (2004), reporting three types of errors introduced by the optical inhomogeneity of the medium under investigation: the position and velocity errors and particle-image blur. The first two errors are systematic while the last one increases the signal-to-noise ratio of the PIV data. In addition, it was

demonstrated that the systematic errors are related to the second derivative of the refractive index in the velocity direction.

In acoustic PIV, the instantaneous refractive index of the fluid under observation is proportional to the acoustic pressure. According to this and based on the results by Elsinga et al. (2004), the source of the velocity error is only significant when the second order pressure gradient in the direction of velocity is remarkable.

4.4.2 Sound Field – Tracer Particles Interactions

The interaction between sound field and tracer particles in a PIV measurement is mutual and may have a strong intrusive participation.

The presence of tracer particles in a fluid can cause attenuation of the propagation of sound in that fluid (Kinsler et al. 2000, §8.10). In fact, the more faithfully the tracers follow the fluid, implying that more momentum from the sound waves is transferred to them, the greater the attenuation of the sound wave. This leads to a sort of 'uncertainty' between the accuracy of the acoustic PIV measurement and the disturbance of the measured acoustic wave.

Conversely, the effect of sound fields on tracer particles, beyond helping to measure the fluid motion by forcing the tracers to follow it, takes the unwanted form of spatial redistribution of the tracer particles. This happens as a result of migration of the particles introduced by a non-zero averaging motion. Moreover, the different motions of the tracer particles may cause them to collide and adhere to each other which leads to a size redistribution. As will be shown later, a consequence of the size redistribution is the velocity redistribution of the particles.

The remainder of this chapter focusses upon the sound field – tracer particles interactions.

4.5 Motion of Small Particles in Standing Sound Fields

4.5.1 Terminology

The term *aerosol* refers to a suspension of fine solid or liquid particles in a gaseous medium. A similar suspension in a liquid is referred to as a *hydrosol*. The scope of this study is limited to aerosols.

In the presence of sound fields, *rigid* aerosol particles are defined as volumes with no sound waves inside them, while sound waves can exist inside *deformable* aerosol particles.

The motion of fluid around an aerosol particle applies a force to it. The elements of this force which are parallel and perpendicular to the fluid motion are known as the *drag* and *lift* forces, respectively. When the fluid motion is oscillatory, as in an acoustic field, the temporal average force that aerosol particles experience is named the *drift* force.

The *Reynolds number of the aerosol particles* helps to describe how the fluid flows around the particles. The number is defined as the ratio of the inertial and the viscous forces which, for a spherical particle, may be given as

$$\mathcal{N}_{\mathrm{Re}} = \frac{2\,r_p\,|\vec{v} - \vec{v}_p|}{\nu}, \tag{4.5.1}$$

where r_p is the radius of the particle, $|\vec{v} - \vec{v}_p|$ is the relative velocity of the particle and the fluid and the kinematic viscosity coefficient is denoted by ν.

4.5.2 Equation of Motion

In a turbulent flow, the motion of spherical particles with dimensions much smaller than the minimum wavelength of the turbulence may be described by the Basset-Boussinesq-Oseen (BBO) equation (Boussinesq 1885; Basset 1888; Oseen 1927). A general form of the BBO integro-differential equation, which is also valid for the spacial case of laminar flow, can be written as

$$\begin{aligned}
\frac{4\pi}{3} r_p^3 \rho_p \frac{\mathrm{d}}{\mathrm{d}t}\vec{v}_p = &-\frac{4\pi}{3} r_p^3 \vec{\nabla} p \\
&+ \frac{1}{2}\frac{4\pi}{3} r_p^3 \rho_0 \frac{\mathrm{d}}{\mathrm{d}t}(\vec{v} - \vec{v}_p) \\
&+ \frac{4\pi}{3} r_p^3 \rho_p \frac{1}{\tau_D}(\vec{v} - \vec{v}_p) \\
&+ 6 r_p^2 \sqrt{\pi \rho_0 \eta} \int_{t_0}^{t} \frac{1}{\sqrt{t - t'}} \frac{\mathrm{d}}{\mathrm{d}t'}(\vec{v} - \vec{v}_p)\mathrm{d}t' \\
&+ F_e,
\end{aligned} \tag{4.5.2}$$

where ρ_p is the density of the aerosol particle and η is the dynamic viscosity of the fluid.

The first term on the right hand side of this equation describes the force generated by the pressure gradient $\vec{\nabla}p$ in the fluid around the particle.

The second term is the force due to the *apparent mass* of the particle relative to the fluid. This force is the outcome of the direct exchange of momentum between the particle and the fluid, assuming that the fluid is ideal (Lamb 1932).

The third term of the equation is due to the viscous drag force with $1/\tau_D$ as a time constant for the momentum transfer given by

$$\frac{1}{\tau_D} = \frac{3}{8} C_D \frac{\rho_0}{\rho_p r_p} |\vec{v} - \vec{v}_p|, \tag{4.5.3}$$

where C_D is the *drag coefficient*.

The fourth term of the BBO equation (4.5.2) is the *Basset history integral force*. This force is due to the non-uniform relative motion of the viscous fluid depending crucially on the path of the motion of the particle.

The last term is due to any potential field force such as gravity or electromagnetic forces.

4.5.2.1 Assumptions

The BBO equation is valid for a wide range of parameters. The scope of interest throughout this study is defined by the following assumptions.

Assumption 4.i. The aerosol particles have a spherical shape and they are rigid in sound waves.

Assumption 4.ii. The particles do not have any kind of interaction with each other.

Assumption 4.iii. The dimension of the aerosol particles is much smaller than the wavelength of the sound field,

$$\frac{r_p}{\lambda} \ll 1. \tag{4.5.4}$$

Assumption 4.iv. The density of the aerosol particles is much greater than the equilibrium density of the host fluid,

$$\frac{\rho_p}{\rho_0} \gg 1. \tag{4.5.5}$$

Assumption 4.v. The velocity of the aerosol particles relative to the host fluid changes slowly so that

$$\left| \frac{d}{dt}(\vec{v} - \vec{v}_p) \right| \ll 1. \tag{4.5.6}$$

Assumption 4.vi. The aerosol particles have low Reynolds numbers implying that the drag coefficient is given by the Stokes' law regime as (Stokes 1847)

$$C_D = \frac{24}{\mathcal{N}_{Re}}. \tag{4.5.7}$$

4.5.2.2 Equation of Motion in Standing Sound Fields

The preceding assumptions enable the BBO equation (4.5.2) to be greatly simplified. For example, taking into account Assumption (4.iv), the pressure gradient and apparent mass terms are negligible. In addition, Assumption (4.v) ensures that the Basset history integral value can be ignored. Finally, Assumption (4.vi) determines the final form of the viscous drag force giving the one-dimensional equation of motion of aerosol particles as

$$\frac{4\pi}{3} r_p^3 \rho_p \frac{d}{dt} v_p = 6\pi \eta \, r_p \, (v - v_p). \tag{4.5.8}$$

Introducing the *relaxation time of an aerosol particle* as a function of the size of the particle:

$$\tau_p(r_p) = \frac{2}{9} \frac{\rho_p}{\rho_0} \frac{r_p^2}{\nu}, \tag{4.5.9}$$

the equation of motion can be re-arranged to

$$\tau_p \frac{d}{dt} v_p + v_p = v. \tag{4.5.10}$$

In the particular case of a standing wave sound field, substituting Equation (2.4.9) into the equation of motion yields

$$\tau_p \frac{d}{dt} v_p + v_p = v_0 \sin(kx) \cos(\omega t). \tag{4.5.11}$$

The general form of this differential equation may be given as (Polyanin and Zaitsev 1995)

$$v_p(x,t) = v_x \mu_p \sin(\omega t - \varphi) + v_x \mu_g e^{-t/\tau_p} \tag{4.5.12a}$$

$$v_x = v_0 \sin(kx) \tag{4.5.12b}$$

$$\varphi = \tan^{-1}(\omega \tau_p) \tag{4.5.12c}$$

$$\mu_p = \cos(\varphi) \tag{4.5.12d}$$

$$\mu_g = \sin(\varphi), \tag{4.5.12e}$$

where φ is a phase shift angle and μ_p and μ_g are the *entrainment coefficient* and the *flow-around coefficient*, respectively. After a time approximately equal to τ_p, the second term in Equation (4.5.12a) is negligible and the particle is approximately in a steady-state. Considering this, the velocity of an aerosol particle in a sinusoidal standing wave is sinusoidal in nature with the spatial amplitude reduced by a factor of $\cos(\varphi)$ and a temporal delay of φ introduced.

4.5.3 Velocity Distribution

In practice, an ensemble of aerosol particles has a size distribution. According to Equation (4.5.12a), the velocity of an aerosol particle in a sound field is a function of its size. This implies that, at any space-time, aerosol particles have a distribution in the velocity space. One immediate consequence of this argument is that the number of tracer particles which follow the fluid faithfully is a function of space-time. Consequently, when performing an acoustic PIV measurement, a pre-existing knowledge of the velocity distribution behaviour of the tracer parti-

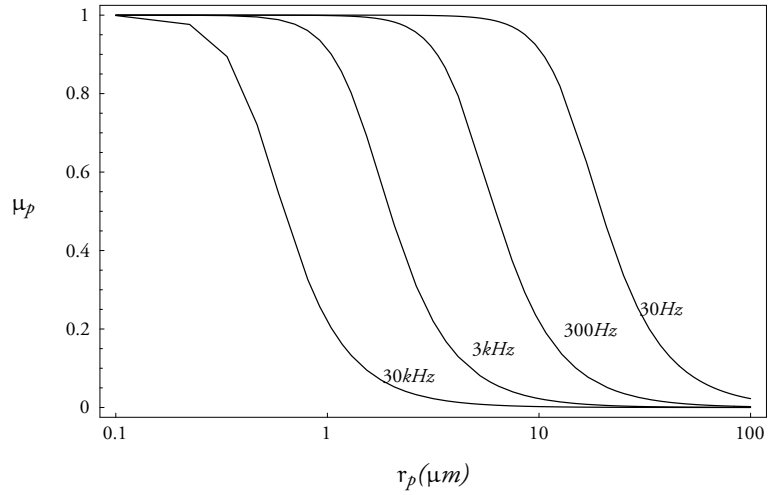

Figure 4.5: *Values of the entrainment coefficient for different frequencies.*

cles in the sound field under investigation may be crucial.

4.5.3.1 Fluctuation of Number of Illuminated Particles

The tracer particles which contribute to velocimetry, distinguished by illumination, are a sub-set of the whole ensemble of particles. Given a fixed illumination volume, in the presence of a sound field, the number of contributing particles is a function of the dimensions and position of the visualisation volume, as well as of time. The aim is to calculate this number at any space-time as a pre-requisite for obtaining the velocity distribution.

Consider a resonant tube with aerosol particles homogenously distributed inside it. It is assumed that the velocimetry measurement is performed in a narrow-enough band, with a length of Δx_L, across the tube so that the velocity within the illumination volume has an almost constant value implying the criterion

$$\Delta x_L \ll \lambda. \tag{4.5.13}$$

Let the *instantaneous number density* of the aerosol particles be n_p; that is, the number of particles per unit volume at any time. The aerosol particles and the host fluid can be treated as a multi-phase system where each phase fulfills the

continuity condition independently. Hence, the equation of continuity for the aerosol particles may be written as

$$\partial_t n_p + \partial_x (n_p v_p) = 0, \tag{4.5.14}$$

Expressing the instantaneous number density as *equilibrium number density* n_{p_0} and *fluctuating number density* n_p:

$$n_p = n_{p_0} + \delta n_p, \tag{4.5.15}$$

the equation of continuity can be linearised to

$$\partial_t \delta n_p + n_{p_0} \partial_x v_p = 0. \tag{4.5.16}$$

Using the boundary condition of Equations (2.4.4) and (2.4.6), a solution of the linear continuity equation is

$$\delta n_p = -n_{p_0} \frac{v_0}{c} \cos(\varphi) \cos(kx) \cos(\omega t - \varphi), \tag{4.5.17}$$

giving the instantaneous number density as

$$n_p(x,t) = n_{p_0} \left(1 - n_{p_0} \frac{v_0}{c} \cos(\varphi) \cos(kx) \cos(\omega t - \varphi)\right). \tag{4.5.18}$$

The number of illuminated particles in the volume $(\Delta z_L \, W \, \Delta x_L)$ can be given by

$$\mathcal{N}_p = \Delta z_L \, W \int_x^{x+\Delta x_L} n_p(x) \, dx, \tag{4.5.19}$$

where W and Δz_L are the width of the tube and the thickness of the light sheet, respectively. After integration, the number of illuminated particles may be expressed in terms of equilibrium and fluctuating parts by

$$\mathcal{N}_p = \mathcal{N}_{p_0} + \delta \mathcal{N}_p, \tag{4.5.20a}$$

where

$$\mathcal{N}_{p_0} = (\Delta z_L \, \Delta x_L \, W) \, n_{p_0}, \tag{4.5.20b}$$

and

$$\delta\mathcal{N}_p = \mathcal{N}_{p_0} \frac{v_0}{c} \cos(\varphi) \cos(\omega t - \varphi) \left(\frac{\sin(kx - k\Delta x_L) - \sin(kx)}{k\Delta x_L} \right). \quad (4.5.20c)$$

Using Equation (4.5.13), when $k\Delta x_L \ll 1$, the fluctuation in the number of illuminated particles can be approximated as

$$\delta\mathcal{N}_p \cong \mathcal{N}_{p_0} \frac{v_0}{c} \cos(\varphi) \cos(\omega t - \varphi) \cos(kx). \quad (4.5.21)$$

Equation (4.5.21) shows that the value of $\delta\mathcal{N}_p$ depends mainly upon the ratio of the acoustic velocity to the phase velocity. In linear sound fields this ratio is a small number implying that the fluctuation is negligible in the linear regime and

$$\mathcal{N}_p \cong \mathcal{N}_{p_0}. \quad (4.5.22)$$

This value of the instantaneous number of illuminated particles will be used to calculate their velocity distribution.

4.5.3.2 Calculation of Velocity Distribution

As a consequence of homogenous spatial distribution, the illuminated aerosol particles in an acoustic PIV measurement have almost the same size distribution as the whole ensemble. The probability density function (PDF) of the size distribution is defined by

$$d\mathcal{N}_{p_0} = f_r(r_p)\, dr_p, \quad (4.5.23a)$$

where $d\mathcal{N}_{p_0}$ represents the number of illuminated particles whose radii are between r_p and $r_p + dr_p$. The normalisation condition gives the total number of illuminated particles at any space-time which, following on from the discussion in §4.5.3.1, may be approximated to its equilibrium value:

$$\int_0^{+\infty} f_r(r_p)\, dr_p = \mathcal{N}_{p_0}. \quad (4.5.23b)$$

Commonly, the size distribution of aerosol particles is described by a log-normal distribution.

In a similar way, the PDF of the velocity distribution of the illuminated particles and the associated normalisation condition may be written as

$$\mathrm{d}\mathcal{N}_{p_0} = f_v(v_p)\,\mathrm{d}v_p \tag{4.5.24a}$$

$$\int_{-v_0}^{+v_0} f_v(v_p)\,\mathrm{d}v_p = \mathcal{N}_{p_0}. \tag{4.5.24b}$$

Combining Equations (4.5.23a) and (4.5.24a) and expressing each differential element of the velocity space in terms of a differential element in the size space, the PDFs of velocity and size distributions are related to each other by

$$f_v(v_p)\,\partial_\varphi v_p\,\partial_{r_p}\varphi\,\mathrm{d}r_p = f_r(r_p)\,\mathrm{d}r_p. \tag{4.5.25}$$

Typical values for the phase shift φ of the tracer particles commonly used in acoustic PIV measurements are much smaller than unity. Considering this, after some algebraic manipulation, Equation (4.5.25) reads

$$f_v(v_p) = \left(\frac{r_p}{2\varphi\, v_0\, \sin(kx)\, \sin(\omega t - 2\varphi)}\right) f_r(r_p),\ \varphi \ll 1. \tag{4.5.26}$$

Since the area under the distribution curve is assumed to be constant, a rough estimation of the width of the distribution may be given by

$$\sigma_v \cong \sigma_{v_0}\, v_0\, |\sin(kx)\, \sin(\omega t - 2\varphi)|, \tag{4.5.27a}$$

where

$$\sigma_{v_0} = \frac{2\varphi\, \mathcal{N}_{p_0}}{r_p f_r(r_p)}\,. \tag{4.5.27b}$$

Equation (4.5.27a) states that at the extremum points of the acoustic velocity the velocity distributions of the aerosols are wider than the velocity distributions where the acoustic velocity is zero. The ratio of these velocity distribution widths is given by $\tan(2\varphi)$.

Part II

Applications

Chapter 5

Instrumentations

Dear friend,
all theory is gray;
And green
the golden tree of life.

Johann Wolfgang von Goethe, *Faust*

The experimental set-up, designed for acoustic PIV measurements, comprises a set of hardware which is controlled by, and whose output is analysed by, self-written software (Figure 5.1). The measurement cycle is initiated by the software sending a series of input signals to the hardware. The signals contain the required information for both running the experiment and performing the measurement. The measurement cycle continues as the hardware output is received and analysed by the software.

Typically, acoustic PIV measurements need to be run temporally as well as spatially, requiring a large number of inputs and the analysis of a high volume of output. This makes automating the measurement cycle a crucial factor in speeding up the process and cutting down on human error. To this end, the software layer has been designed to allow the number of hardware components to be kept to a minimum, enabling a large number of PIV measurements to be made in rapid succession via automation of the system. Some other benefits include making the system more flexible, time-effective and cost-friendly.

In the following, the hardware and software components are discussed in detail.

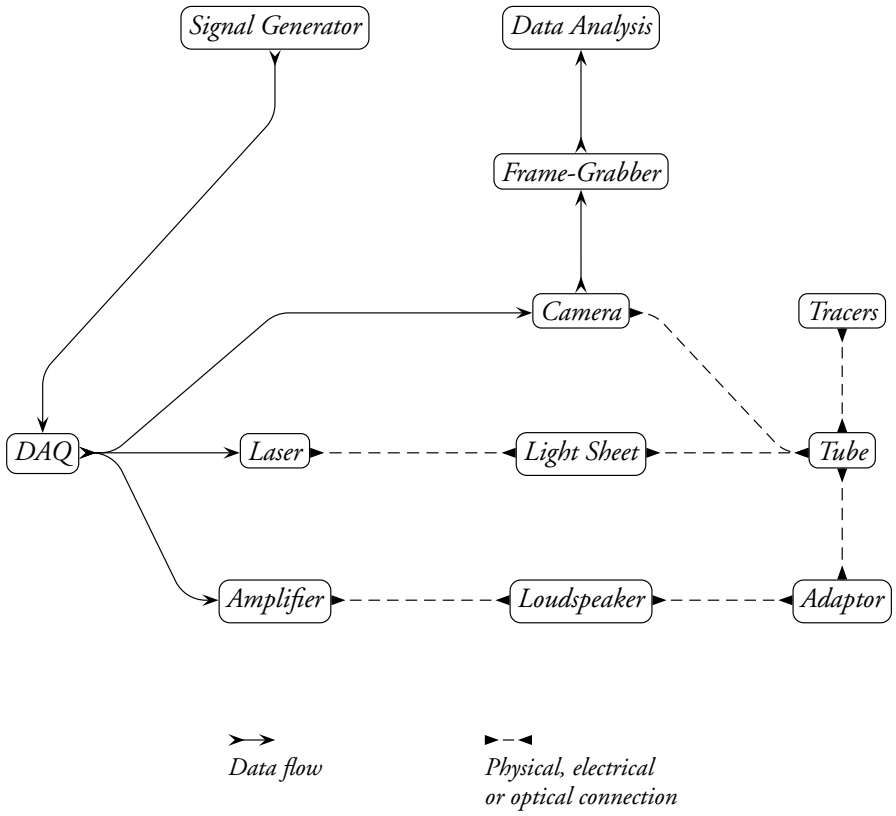

Figure 5.1: *Experimental design.*

5.1 Hardware

The hardware configuration is illustrated in Figures (5.1) and (5.2). The input signals, explained in §5.2, are sent to a data acquisition board (DAQ) housed within a PC. The DAQ performs two main jobs; generating voltages to trigger the other devices and synchronising or delaying the triggered events. In this way, the DAQ is used to control the loudspeaker, to create the desired phenomena inside the tube; and the laser and digital camera, to perform the measurements on the tube. The measurement process ends with the recorded images from the camera being downloaded to the PC via a frame-grabber card and stored in a

digital medium for processing later. The technical specifications of the devices are given in Table (5.1).

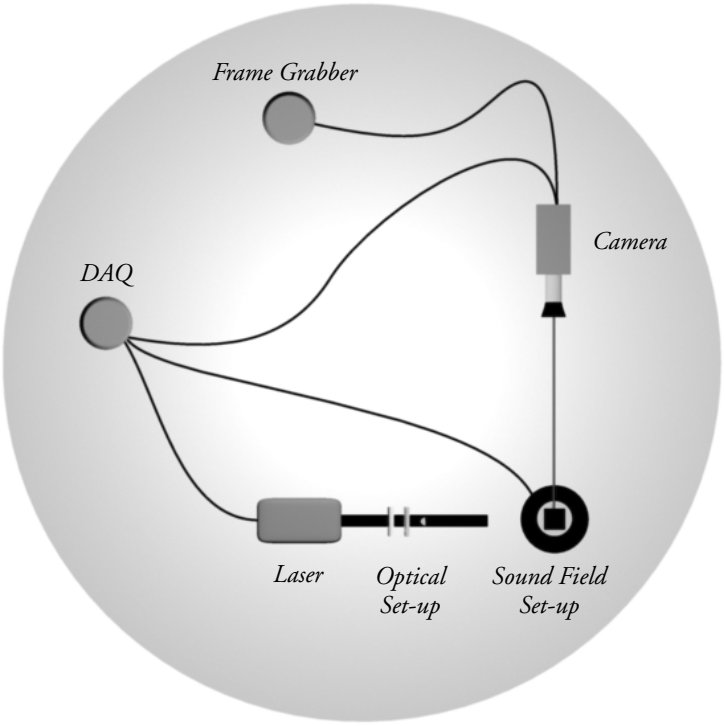

Figure 5.2: *Experimental set-up: hardware configuration.*

5.1.1 The Tube

The transparent tube used in the study is made of Perspex[1] material. The thermal conductivity of Perspex is about 16% that of glass, making it possible to

[1]Perspex is the UK trade name for polymethyl-methacrylate (PMMA).

Device	*Specifications*
DAQ	*IOtech DaqBoard*-2000, 16 bit, 200 kHz
Loudspeaker	
Laser	*Laser Quantum*, 532 nm, 250 mW, CW solid-state
light sheet generator	Three cylindrical lenses (Figure 3.6c),
	Focal lengthes: +19 mm, +200 mm and +60 mm
Camera	*PCO DoubleShutter Sensicam*
Camera lens *A*	$\gamma_f = 12.5$ - 75 mm
Camera lens *B*	$\gamma_f = 55$ - 110 mm
Tube	Perspex
	Length 62.0 cm
	Square cross-section 3.5 cm $\times$ 3.5 cm
	Wall thickness 0.5 cm

Table 5.1: *Specifications of hardware devices.*

thermally insulate the volume inside the tube more efficiently than glass. Moreover, allowing about 92% of visible light, Perspex is a better choice over glass in transmitting light energy.

One end of the tube is terminated in an acoustically rigid manner while the other end is, via an adaptor, connected to the loudspeaker. The tube length is 62.0 cm with a square cross-section of dimensions 3.5 cm $\times$ 3.5 cm and a wall thickness of 0.5 cm.

The choice of a cuboidal tube shape is in order to avoid the flare problem which is common in cylindrical tubes due to the unwanted light reflected from their curved walls. The area in PIV images which is affected by flare suffers a severe lack of data. In principle, it is conceivable to overcome the flare problem when the light scattered from the tracer particles has a different wavelength to the light reflected from the walls.[2] In this way, the flare light may be easily filtered.

5.1.2 Tracer Particles

During the measurement, the tube under investigation is seeded using smoke for the tracer particles. The smoke is generated by burning incense of the joss-stick type. Figure (5.3) shows the size distribution of typical joss-stick smoke

[2]This is possible by dying the tracer particles using fluorescence when, after absorbing the illumination light, they can emit a light with a different wavelength.

particles measured by an Electric Low Pressure Impactor (ELPI) (Jetter et al. 2002). The peak of the size distribution is located between 2.6 and 4.0 μm.[3] As generated from oil-based material, the density of the smoke particles is expected to be of the order of 1000 to 2000 Kg/m^3.

Following the discussions in §4.5.2.2, at sound field frequencies up to a few kilo-Hertz, sub-micron aerosols whose density is much higher than of air have an entrainment coefficient near unity (Figure 4.5). This implies that, at low-enough frequencies, the smoke particles are expected to follow the air flow faithfully.

While incense smoke is the most cost-effective way of visualising air flows, there are alternative methods which provide better control over physical characteristics of the tracer particles. One example is using aerosol generators which create micron-sized particles from almost arbitrary liquids. The tracer particles generated by this device have a sharp peak of size distribution. Moreover, in order to get particle-images of better quality, it is possible to increase the intensity of the light reflected from the tracer particles with the right choice of source liquid.

5.1.3 Light Sheet

The optical set-up used to generate the light sheet, for illuminating the tracer particles, consists of three cylindrical lenses, as shown in Figure (3.6c) on page 25, with focal lengths given in Table (5.1). The generated light sheet is able to illuminate a region of around 1 cm high across the width of the tube, thickness of the light sheet has a Gaussian profile with a width of less than 1 mm.

5.1.4 Laser

The option exists to run the laser in either a CW mode (§3.3.1) or to trigger it by an external source to produce a beam with an intensity varying as an arbitrary function of time.

[3]Commonly, in order to fulfil health and safety regulations, burning incense is preferred to cigarette smoke. Measurements by Jetter et al. (2002) points out that incense smoke particles are of sub-micron size and may be as unhealthy as cigarette smoke.

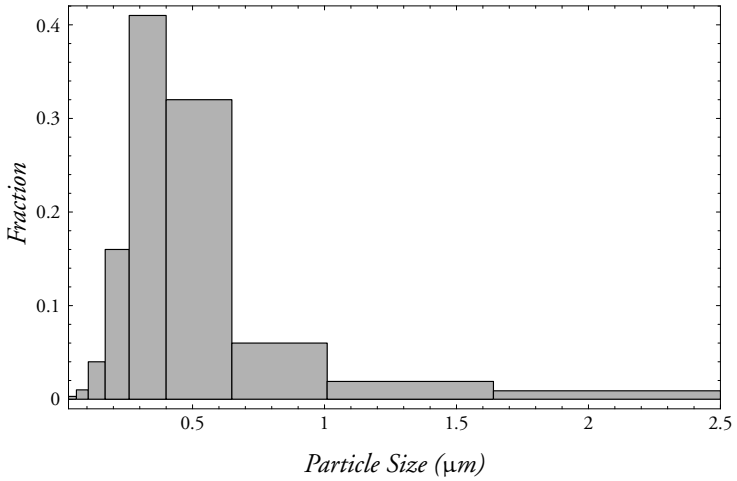

Figure 5.3: *Size distribution of smoke particles generated by burning typical joss-sticks with a peak between* 2.6 *and* 4.0 μ*m. The data is adopted from Jetter et al. (2002)*

5.1.5 Camera

The digital camera device used in the set-up may be triggered, by an external source, to perform two exposures: a dynamic exposure, whose duration can be controlled by the trigger source, and a static exposure which lasts for a constant time of the order of a few milliseconds. The end of the first exposure is separated from the beginning of the second exposure by a delay of the order of nanoseconds.

In a PIV set-up, the recording process may be controlled by either illumination (the laser) or by exposure (the camera). In the first method, depending on the purpose of the experiment, the camera shutter is left open to expose one or more laser illuminations. In the second method, the laser is run in the CW mode and the exposures are performed by the camera at the desired times and durations. Due to the fact that the second exposure of the camera is not controllable, it is only practical to use the first method in this experimental set-up.

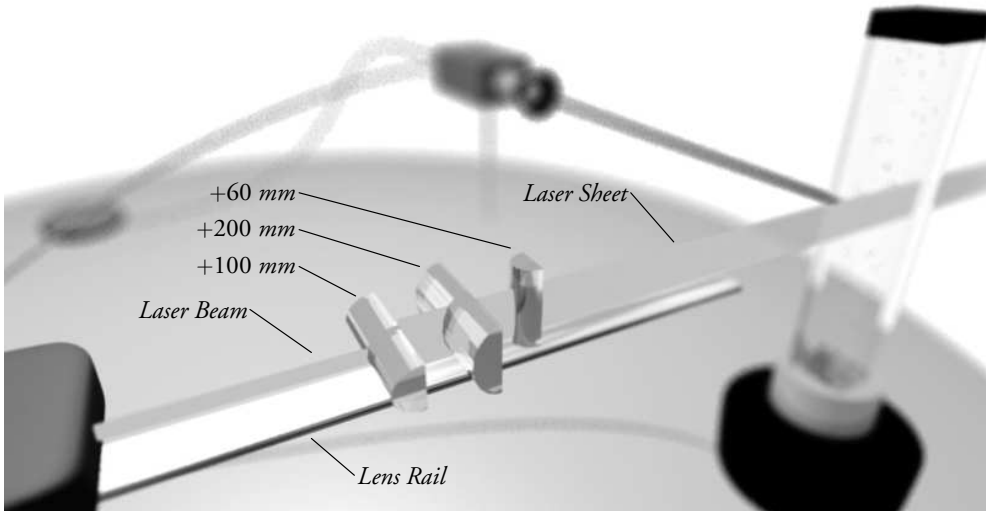

Figure 5.4: *Experimental set-up: hardware configuration.*

5.2 Software: Input Signals

The following signals are used to control the hardware configuration:

SOUND WAVE SIGNAL. The loudspeaker is driven by the corresponding signal for the sound field of interest. Throughout, this signal is referred to as the *sound wave signal*.

ILLUMINATION SIGNAL. The laser is triggered by the *illumination signal* to produce 'quasi-pulses'; that is, pulses which are generated as a result of applying a square-function to the laser running in the trigger mode. Quasi-pulses provide the flexibility of being able to be triggered at any desired time. However, since there is no energy storage prior to sending the quasi-pulse, the output light may not be intense enough for some measurements.

EXPOSURE SIGNAL. A square-function signal, similar to the illumination signal, referred to as the *exposure signal*, is sent to the digital camera device. Following the discussions in §5.1.5, the recording process is controlled by

the illumination signal. Consequently, in order to ensure that each PIV image is captured at the instant when the tube is being illuminated by the light sheet, the recording signal must be carefully synchronised with the illumination signal.

The illumination and exposure signals are in the form of high-TTL.[4] Depending on the aim of the measurement, various combinations of the input signals may be used. The illumination signals used in this study are of identical duration and each is covered by one exposure signal. This configuration produces multiple (double) frames - single exposure data (§3.5.6.2) which is suitable for a cross-correlation analysis.

5.2.1 Scanning the sound wave signals

Although the illumination and exposure signals must be carefully synchronised with each other, the freedom remains to perform the recording at an arbitrary delay time after the start of the sound wave signal is sent to the loudspeaker. This implies that, by progressively increasing this delay, successive PIV measurements can be made to 'scan' the sound wave signal through time and reconstruct it later by data analysis. This procedure may be applied at any position along the tube to study the spatial variation of the sound wave signal.

Let τ_s be the *scanning duration* of the sound wave under investigation and n_s be the number of points within the scanning duration that velocity measurements are performed. Assuming measurements are taken at equal intervals $\delta\tau_s$, known as the *scanning step*, as illustrated in Figure (5.5), the scanning duration is given by

$$\tau_s = n_s \, \delta\tau_s. \tag{5.2.1}$$

The *velocimetry time* t_v, which is the time separation between the start of the scanning and the mid-point of the delay between two illumination pulses, may be determined as

$$t_v = n \, \delta\tau_s, \; 0 \leqslant n < n_s, \tag{5.2.2}$$

where n is an integer. By progressively increasing the quantised time t_v, while performing a PIV measurement at each time, the velocities associated with the sound wave may be obtained at the scanning frequency.

[4] Transistor-Transistor Logic (TTL) signals are commonly used for triggering. The signal is in the form of a square-function and in the high mode its value is between +2 V and +5 V.

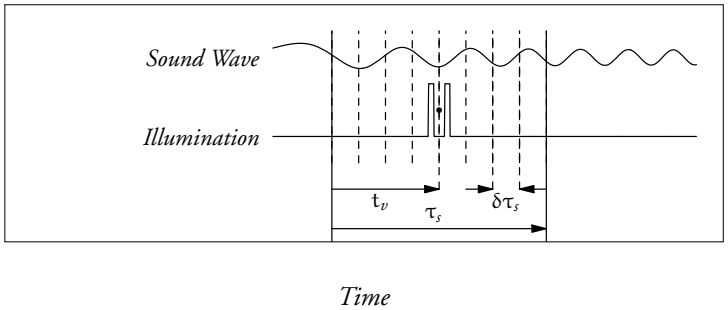

Figure 5.5: *The sound wave scanning process.*

In order to ensure that all the sound wave information in the scanning duration is measured, according to the sampling theorem, the scanning rate $n_s/\tau_s = 1/\delta\tau_s$ must be at least equal to the NYQUIST rate of the sound wave within the scanning duration. In other words, if f_{max} is the highest frequency of the scanned sound wave, the lower-limit of the scanning rate is

$$\min\left(1/\delta\tau_s\right) = 2f_{max}.$$

It may be shown that the upper-limit of $1/\delta\tau_s$ is determined by the specifications of the hardware used for the measurement. Let τ_i be the minimum duration of the illumination pulses which crucially depends on the light source illumination power, the recording device sensitivity and the DAQ precision. The minimum displacement which can be measured by two identical illumination pulses of duration τ_i, assuming that the displacement is measured between the mid-points of the pulses, is within τ_i. This implies that the input sound wave may be measured with the minimum precision of τ_i or

$$\max\left(1/\delta\tau_s\right) = 1/\tau_i.$$

For the experimental set-up used in this study, the upper-limit of $1/\delta\tau_s$ was obtained to be ~ 10 kHz.

When carrying out acoustic PIV measurements, the scanning frequency should

be set to the maximum value obtainable for the system. Although setting the scanning frequency higher than the Nyquist rate does not provide any more information about the reconstructed signal, which is assumed to be the same as the input signals, by doing so any unexpected behaviour of the output can be sampled.

5.3 Software: Output Data Analysis

A diagram describing the data analysis procedure is given in Figure (5.6). The image evaluation process begins by reading a pair of raw PIV images downloaded from camera via the frame-grabber. The images are then pre-processed using Gaussian smoothing which is effective in removing background noise. The kernel size of the smoothing filter was set to 3×3.

Three different algorithms were tried for the main data processing. The FFT-based traditional cross-correlation, as described in §3.5, was implemented as the standard approach. Introduced by Westerweel et al. (1997), *discrete window offset* was used in a second attempt to improve the accuracy in displacement detection in the correlation plane. The method is based on spatial offsetting between the interrogation windows corresponding to the image pair. The offsetting value is an integer-pixel vector which is chosen to be roughly equal to the expected displacement. Hence, the method works best with some pre-existing knowledge of the fluid motion, however, its 'built-in' noise removal is beneficial in reducing detection error.

Both of the previous processing methods generate unavoidable erroneous velocity vectors caused by non-ideal characteristics of the input PIV images. Consequently, in order to obtain reliable results, applying data validation is necessary when these methods are in use. The PIV image evaluation algorithm of *correlation-based correction* 'automatically' filters spurious velocity vectors while calculating displacements in the interrogation area of interest. The method, founded by Hart (2000), involves using two (or more) interrogation areas for detecting each vector. The windows are set apart by a fraction of the interrogation size. The corresponding correlation plane is yielded by element-by-element multiplication of the interrogation areas.

The post-processing filter was implemented to be used in conjugation with data processing methods with inaccurate output. A two-dimensional spatial *adaptive local median* is a common post-processing filter in which each vector

is validated by the median of its neighbours. Typical acoustic PIV measurements include more than two dimensional data, e.g. two dimensions in space and one more dimension in time or sound intensity. Based on this fact, the adaptive local median filter was extended to three dimensions using a $3 \times 3 \times 3$ kernel.

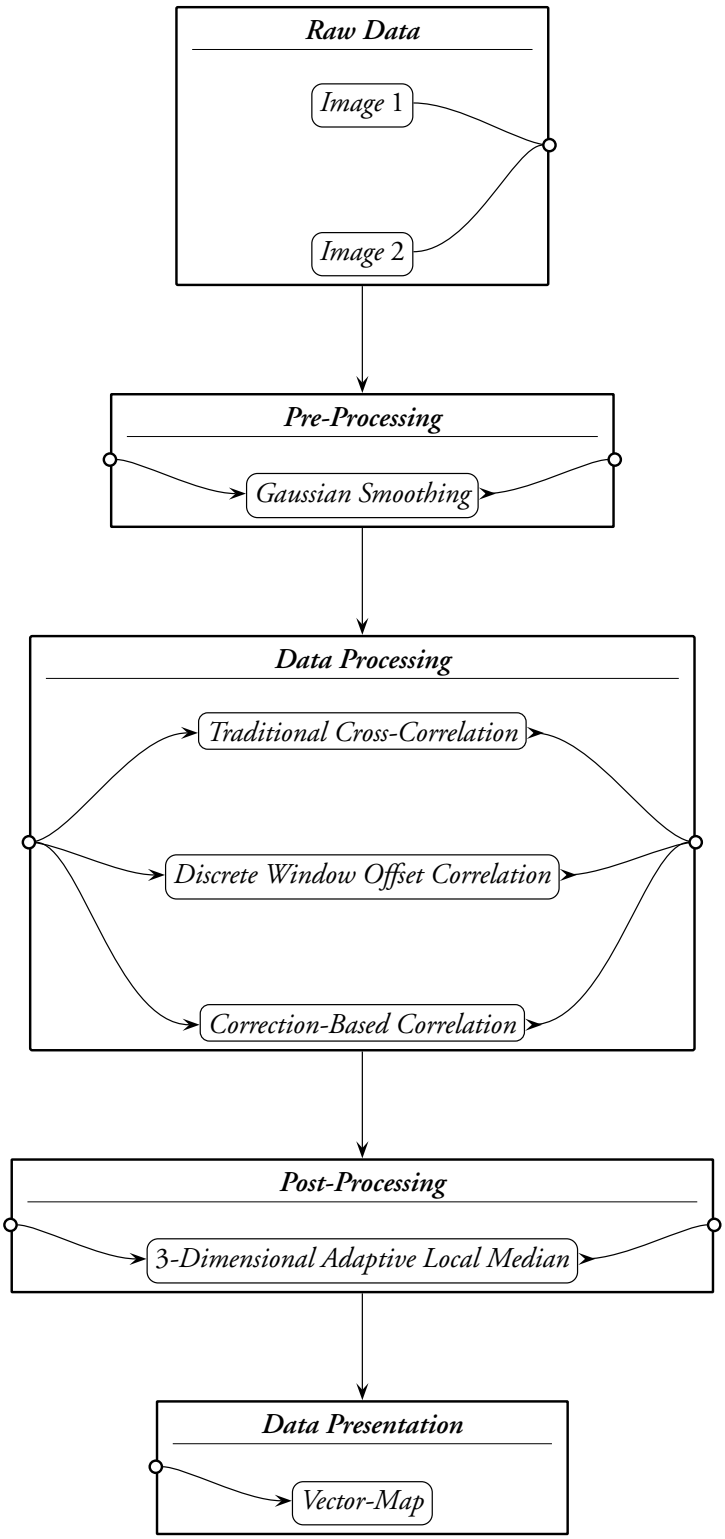

Figure 5.6: *Output data analysis diagram.*

Chapter 6

Measurements

Because things are
the way they are,
things will not stay
the way they are.

Bertolt Brecht

6.1 Sound Pulses

As a preliminary acoustic PIV measurement, the propagation of a sound pulse in tube *A* was studied. The structure of this experiment is similar to methods for finding the impulse response of a loudspeaker with the difference that here the propagation of the velocity wave, instead of the pressure wave, is measured.

6.1.1 Generation and Propagation of Sound Pulses

An ideal pulse may be represented by a δ-function. There are two main factors which cause the pulse created in practice to deviate from the ideal pulse: the pulse generation device and the medium in which the pulse propagates.

A wide range of approaches for generating an ideal sound pulse has been reported in the literature including the use of chemical reactions, spark discharges, electro-acoustic transducers and piezoelectric devices which can produce pulses of the duration of 0.07 to 2 ms. A review of these means may be found in Marshall (1990) where producing sound pulses of the duration of 0.1 ms by a digital signal generator, coupled to different sound generation devices, is presented.

While the pulse generation device diverges the shape of the created pulse temporally, the spatial deviation from the ideal shape is due to the attenuation and dispersion properties of the propagation medium. The acoustic harmonic motions are known to be decayed spatially in an exponential way (Morse and Ingard 1968, §6.4). In contrast, Learned (1979) showed that the spatial decay of sound pulses is non-exponential and is in the form of power-law (Kalinichenko et al. 2001, §5.3).

6.1.2 Measurement

As a basic estimation of a δ-function, a square-function of duration of 0.1 ms was chosen as the input signal for driving the loudspeaker. Two TTL illumination pulses of the duration of 0.1 ms separated by a delay identical to the illumination durations were used to record the PIV images. Figure (6.1) illustrates the design of the input signals.

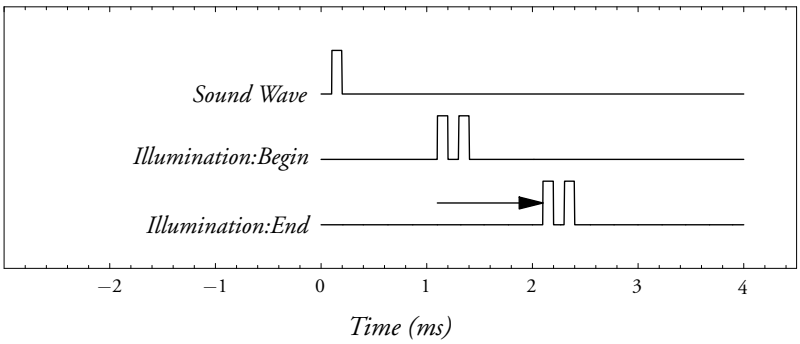

Figure 6.1: *Input signals for the measurement of a sound pulse.*

The measurement was executed at a position 18 cm away from the loudspeaker and for a scanning duration of 1 ms. At the first attempt, a scanning resolution of 0.1 ms was applied to produce 10 PIV images. This makes the temporal overlapping between two consecutive scans to be 50%. Spatially, the images almost covered the width of the tube. The images were then analysed

using correction-based correlation with interrogation areas of size of 256×256 pixels. The results are shown in Figure (6.2).

Figure (6.3) presents the measured velocity pulse obtained by spatial averaging of the acquired vector-maps across the tube, assuming that the change of the velocity vectors across the tube is negligible. While the reconstructed velocity wave is not of a desirable resolution, it confirms that the input square function is measured as a decayed bipolar pulse. The bipolarity of the result reflects the response of the loudspeaker to the input square function.

In order to have a better picture of the pulse, as well as testing the system at a high scanning rate, a second measurement was carried out with an improved temporal resolution of 0.01 ms, keeping the same scanning duration of 10 ms. Hence, the temporal overlapping of two consecutive scans in this measurement is 99%. This produced 100 PIV images which were analysed with the same parameters as the previous measurement. The result is given in Figure (6.4).

It is worthy of notice that the extremely high temporal overlapping of the second measurement not only did not generate over-sampled repeated information, but dramatically improved the reconstructed velocity pulse. Using this data, an excellent fit in the form of a non-symmetrical bipolar Gaussian was obtained describing the impulse response of the loudspeaker (Figure 6.4). Figure (6.5) compares the Fourier transforms of the measured velocity pulses with different scanning resolutions.

6.2 Linear Harmonic Oscillation

The acoustic velocimetry of standing sound waves inside the tube was carried out with the tube driven at its first natural frequency. The tube was coupled by a loudspeaker at one end and rigidly terminated at the other end (§5.1.1). Using an oscilloscope, the first two resonance frequencies were determined to be around 280 Hz and 570 Hz corresponding to periods of about 3.6 ms and 1.8 ms.

Figure (6.6) shows the input signals used for this measurement. A sinusoidal sound wave, with a period matching the resonance frequency of interest, was sent to the loudspeaker while the illumination signal scanned the sound wave over a full acoustic cycle using a temporal scanning resolution of 0.1 ms. This scanning resolution yields a sampling frequency of 10 kHz which is around 18 and 9 times the Nyquist frequency of the two first modes, respectively.

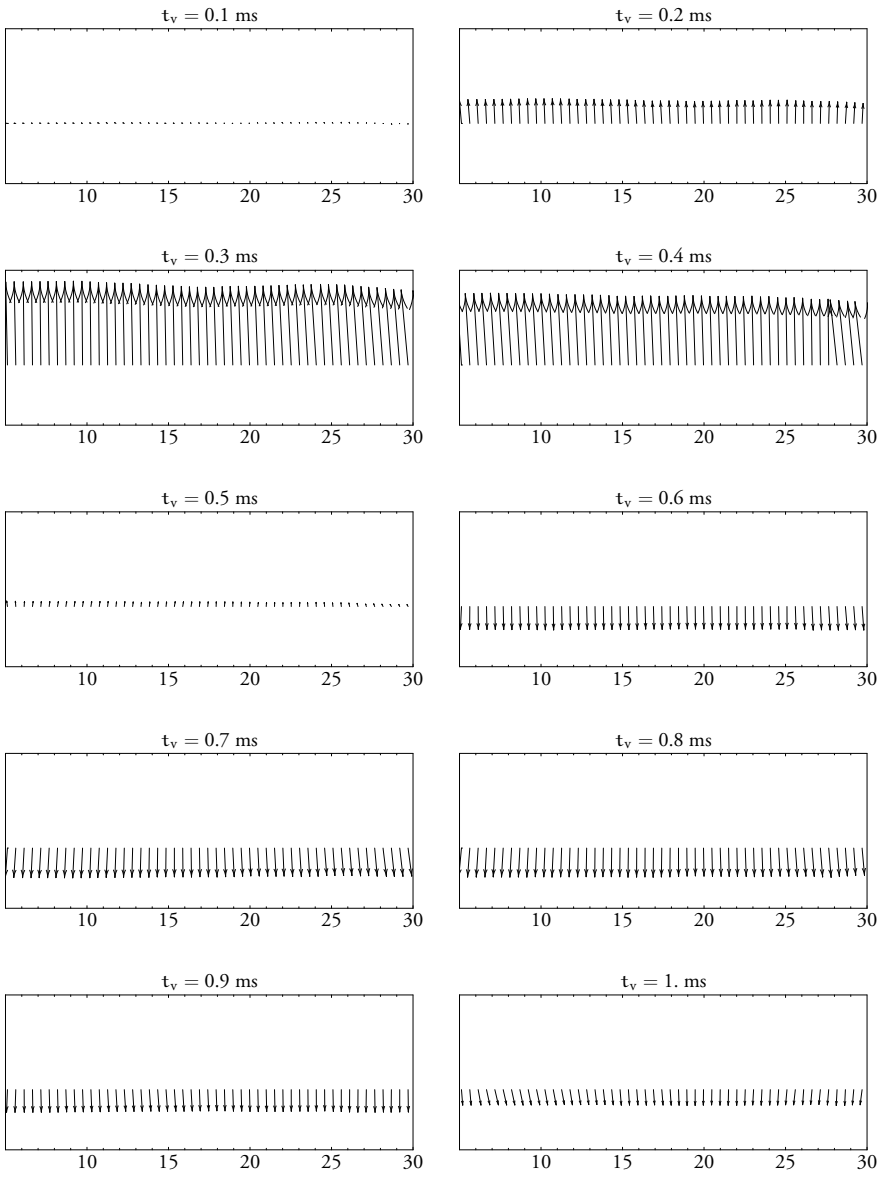

Figure 6.2: *Velocity vector-maps illustrating the temporal scanning of a sound pulse propagating along the tube. The measurements were carried out* 18 *cm away from the loudspeaker. The correlation-based correction algorithm was used with interrogation areas of size of* 256×256 *with* 93.75% *overlapping. The horizontal axes show the width of the tube in mm.*

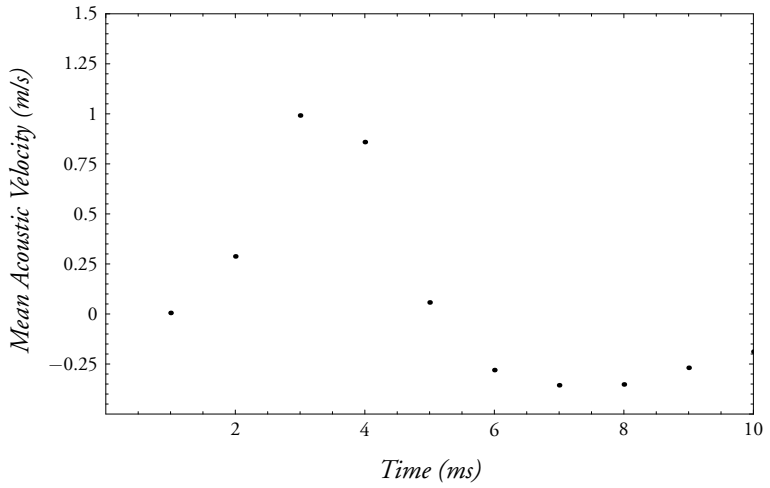

Figure 6.3: *Transversal mean acoustic velocity variation of a sound pulse propagating along the tube with the scanning resolution of* 0.1 *ms. Each point corresponds to the mean value of the velocity vectors in the vector-maps of Figure (6.2).*

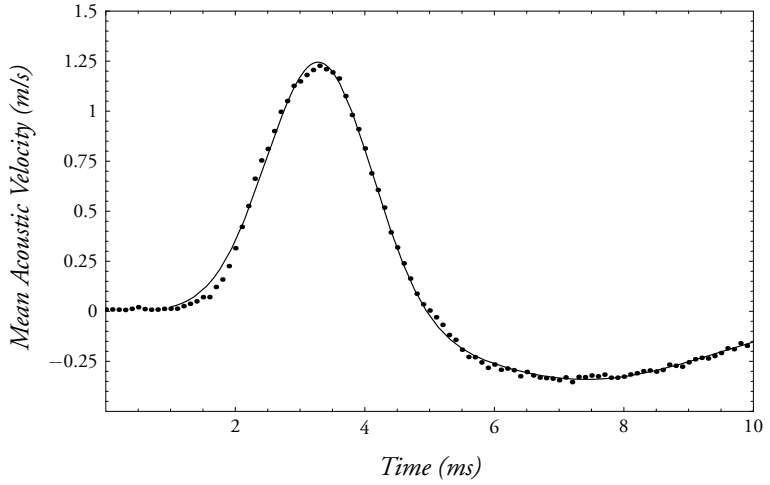

Figure 6.4: *Transversal mean acoustic velocity variation of a sound pulse propagating along the tube with the scanning resolution of* 0.01 *ms. The solid line represents a bipolar Gaussian fit as a function of time given by* $1.29e^{-(0.87t-2.86)^2} - 0.34e^{-(0.35t-2.56)^2}$.

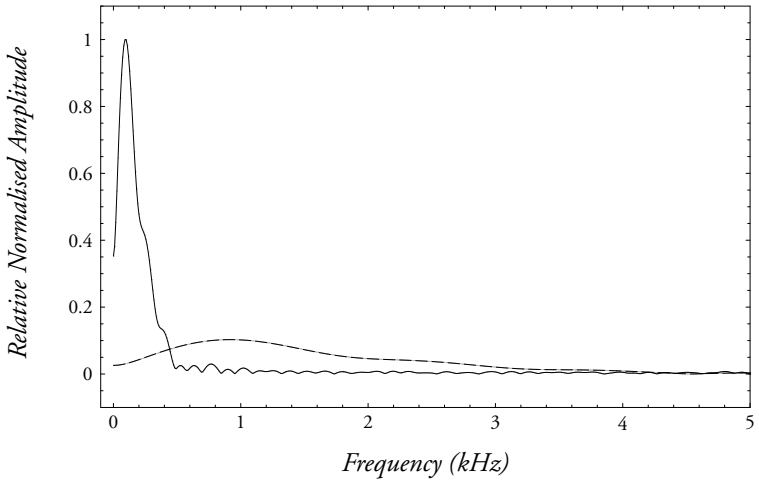

Figure 6.5: *Comparison of the Fourier transforms of the velocity pulse with scanning resolutions of* 0.1 *ms (*10 *samplings, dashed line) and* 0.01 *ms (*100 *samplings, solid line).*

The sound pressure level at the rigid termination was measured by a probe microphone (Brüel & Kjær, 4170) connected to a measuring amplifier (Brüel & Kjær, 2607). The needle of the probe microphone was entered into the tube through a small hole which was made at the end of the tube. Since the input sound intensity was controlled by driving the loudspeaker using a Hi-Fi amplifier, the probe microphone was applied to 'calibrate' the Hi-Fi amplifier. Results are given in Table (6.1).

6.2.1 Variation with Time

Driving the loudspeaker at the two first natural frequencies of the tube, the sound pressure level at the rigid end of the tube was read from the measuring amplifier to be 124.0 dB for the first mode and 123.4 dB for the second mode. The SPL values are corresponded to the Hi-Fi amplifier being set to $2\times$ (Table 6.1). Monitoring the acoustic pressure on an oscilloscope using the probe microphone confirmed sinusoidal variation of acoustic pressure.

Based on the described input signals, the PIV measurements were performed

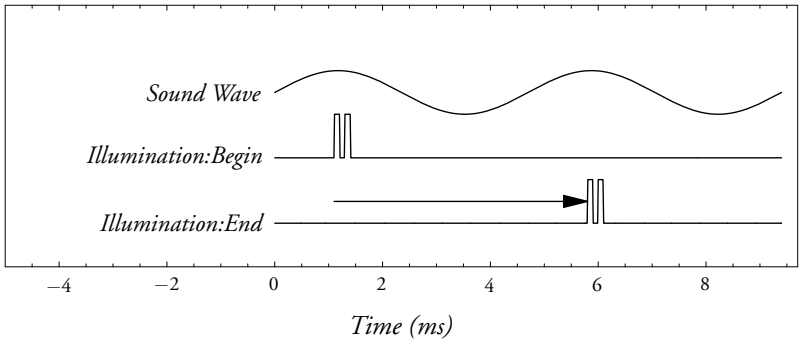

Figure 6.6: *Input signals for the measurement of standing waves.*

Hi-Fi amplifier dial	*SPL of the first mode (dB)*	*SPL of the first mode (dB)*
2×	142.0	143.4
4×	151.2	153.0
6×	155.0	156.9

Table 6.1: *Calibration of the Hi-Fi amplifier using the probe microphone. The SPL values are measured at the rigid end of the tube.*

at a distance 15 cm away from the loudspeaker. The PIV images were analysed by interrogation areas of size of 256×256 using the correlation-based correction algorithm. This algorithm generated vector-maps, shown in Figure (6.7), which did not need any post-processing including data-validation for excluding the spurious vectors.

Averaging the resulting acoustic velocity vectors across the width of the tube, the temporal variation of the standing wave was obtained as shown in Figures (6.8a) and (6.8b) for the first and the second modes, correspondingly. Both variations are almost in a sinusoidal form with an acoustic velocity amplitude of about 0.66 m/s (first mode) and 0.48 m/s (second mode). As the experiment was not designed to extract any temporal phase information, throughout, in presenting the results the temporal phase is manually set to zero.

Figure (6.8c) shows the FOURIER components of the measured acoustic velocity for the first two modes. The two highest peaks in the frequency domain are around the two natural frequencies of the tube. The contribution of the rest of

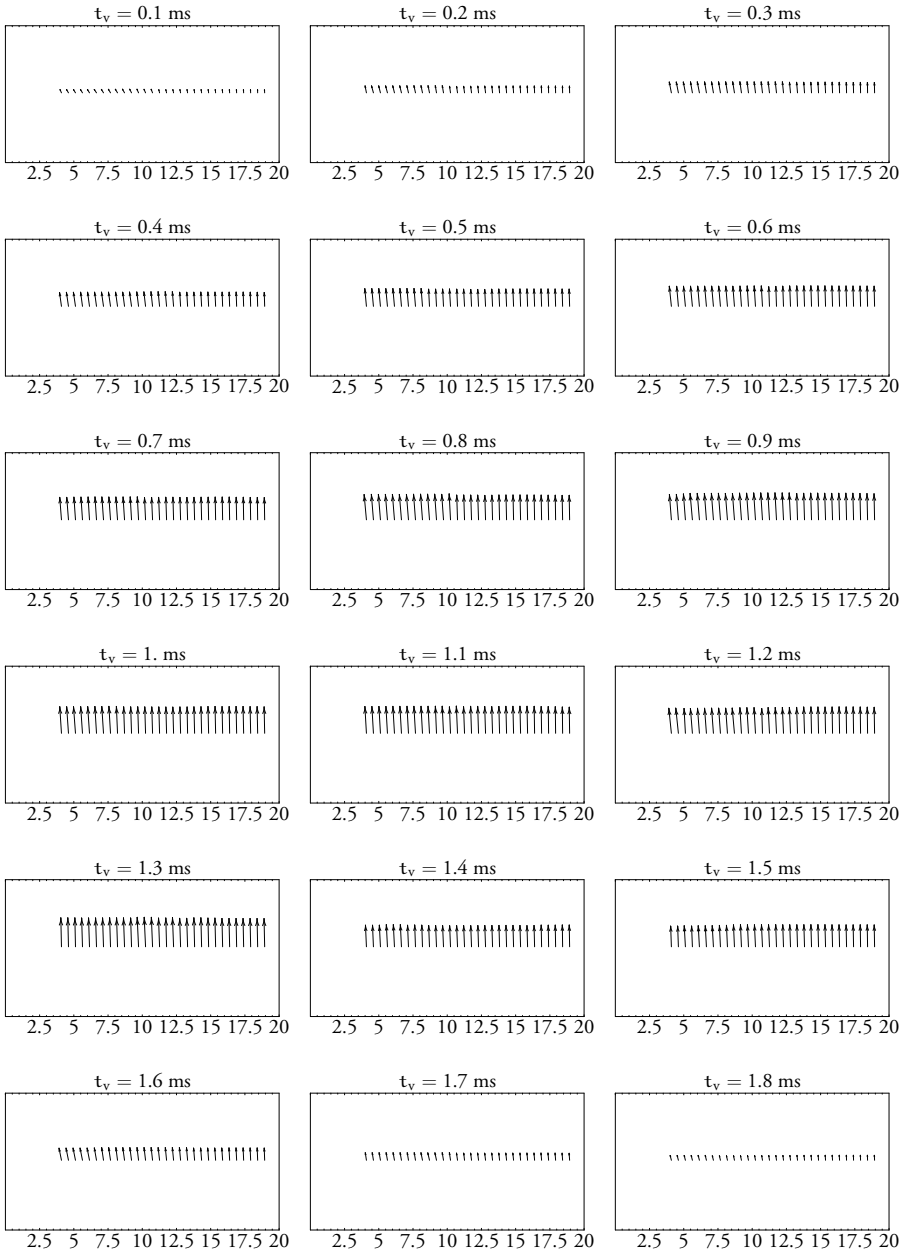

Figure 6.7: *Velocity vector-maps of the harmonic oscillation at the first resonance of the tube with a SPL of* 126.2 *dB and at a position* 15 *cm away from the loudspeaker.*→

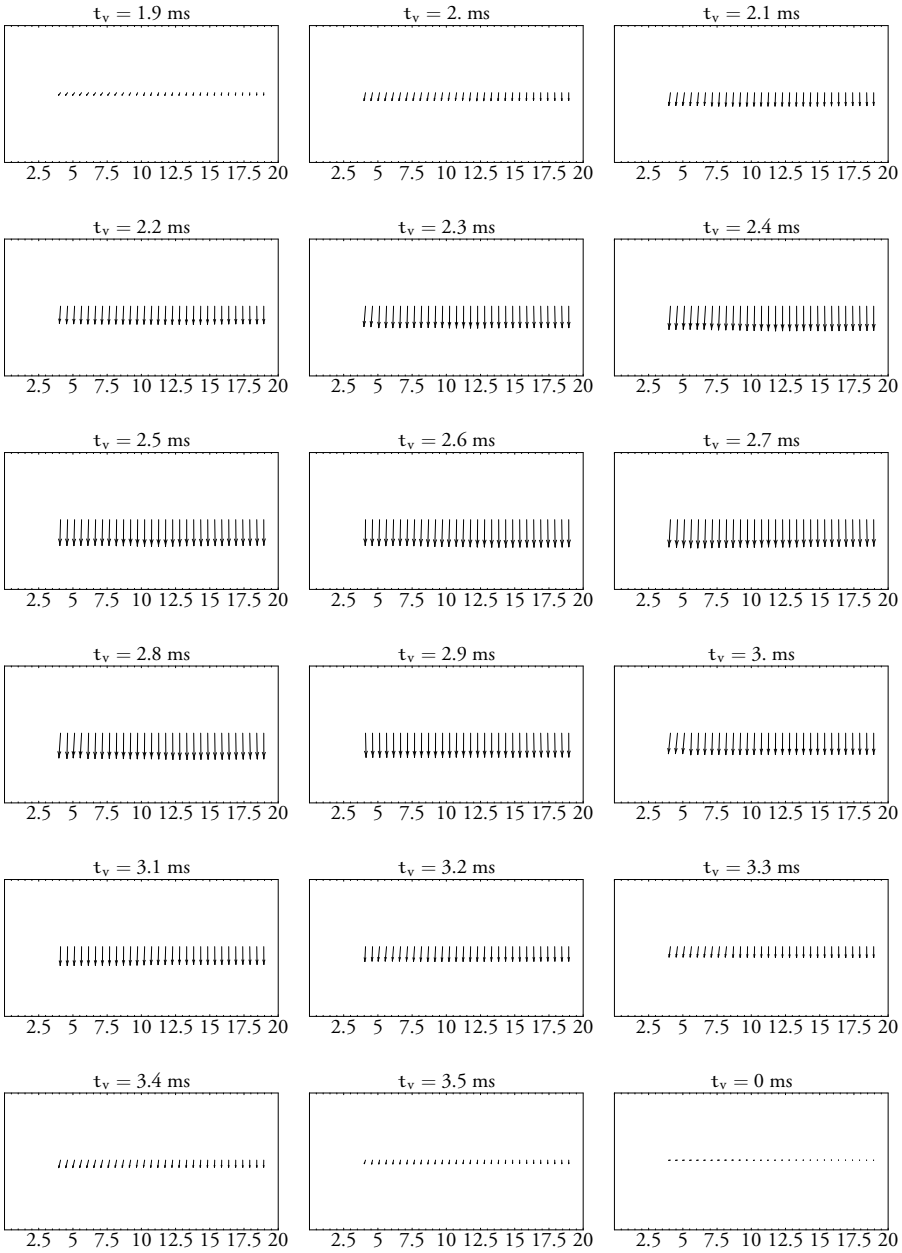

← *The correlation-based correction algorithm was used with interrogation areas of size of* 256×256 *with* 93.75% *overlapping. The horizontal axes show the width of the tube in mm.*

the peaks, especially for the first mode, is quite low.

6.2.2 Variation with Sound Intensity

In the previous measurement, the standing wave of acoustic velocity was measured for constant values of sound intensity and axial distance. The measurements were extended by changing the sound intensity while keeping the rest of the parameters the same.

At 23 cm away from the loudspeaker ($0.19\,\lambda_1$, $0.37\,\lambda_2$), the acoustic velocity inside the tube was temporally scanned for the first two modes when the Hi-Fi amplifier was set to $2\times$, $4\times$ and $6\times$ (Table 6.1). Analysing the PIV data, based on the same parameters used previously, the transversal mean acoustic velocity was obtained as presented in Figures (6.9a) and (6.9b) for the two first modes, respectively. It is noticeable from the results that as the sound intensity increases inside the tube, the measurement system fails to gain expected values. Later, in this work, the sources of this anomaly will be investigated, however–for the time being–the results of this investigation is used to analyse the measurements.

The algorithm employed so far in the processing of the PIV images is founded upon Correlation-Based Correction (CBC). It will be shown that using correlation-based correction together with the Symmetric Phase-Only Filter (CBC-SPOF) dramatically improves the anomalous results towards their expected values.

Figures (6.9c) and (6.9d) demonstrate the variation of acoustic velocities by processing the same PIV images using CBC-SPOF, which imply a significant change when compared to the results obtained by CBC processing.

Calculating their RMS values, the variation of the measured acoustic velocities at the given axial position ($0.19\,\lambda_1$, $0.37\,\lambda_2$) versus the measured SPL at the rigid end is shown in Figure (6.10). As illustrated, the CBC-SPOF processed results well-agree with the theoretical prediction.

6.2.3 Variation with Space

Extending the measurements in one more dimension, the former experiment was carried out along the axis of the tube. In detail, the standing acoustic velocity wave was temporally scanned for different frequencies, sound intensities and positions forming the standing wave patterns of the first two modes.

Figure (6.11) shows the results analysed by CBC-SPOF processing. A comparison of the experimental values with the theoretical standing wave pattern for

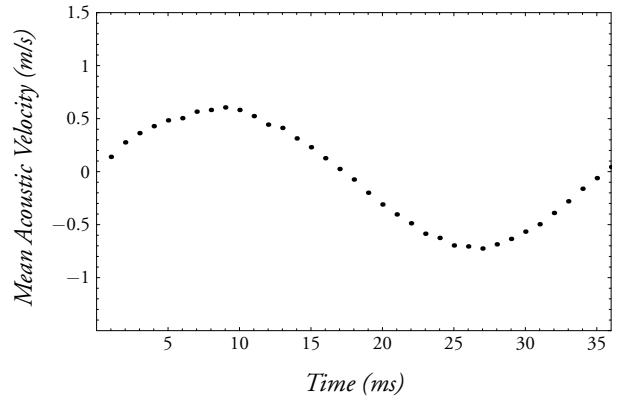

a) *Acoustic Velocity of the first mode with the SPL of* 124.0 *dB. Each point corresponds to the mean value of the velocity vectors in the vector-maps of Figure (6.7).*

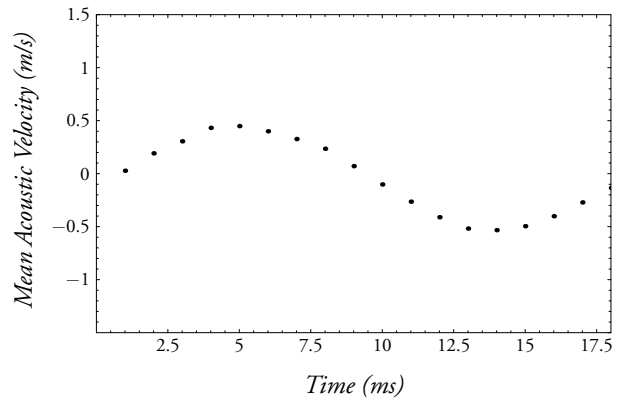

b) *Acoustic Velocity of the second mode with the SPL of* 123.4 *dB.*

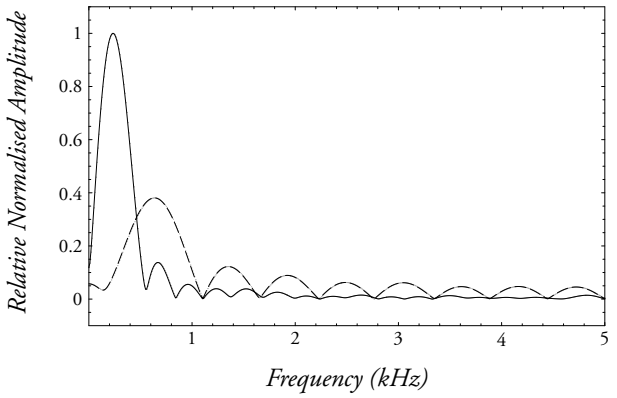

c) *The Fourier transforms of the acoustic velocities of the first mode (solid line) and the second mode (dashed line) of the tube.*

Figure 6.8: *Transversal mean acoustic velocity variation of the first two modes of the tube and their Fourier components. Measured at* 15 *cm away from the loudspeaker with the scanning resolution of* 0.1 *ms.*

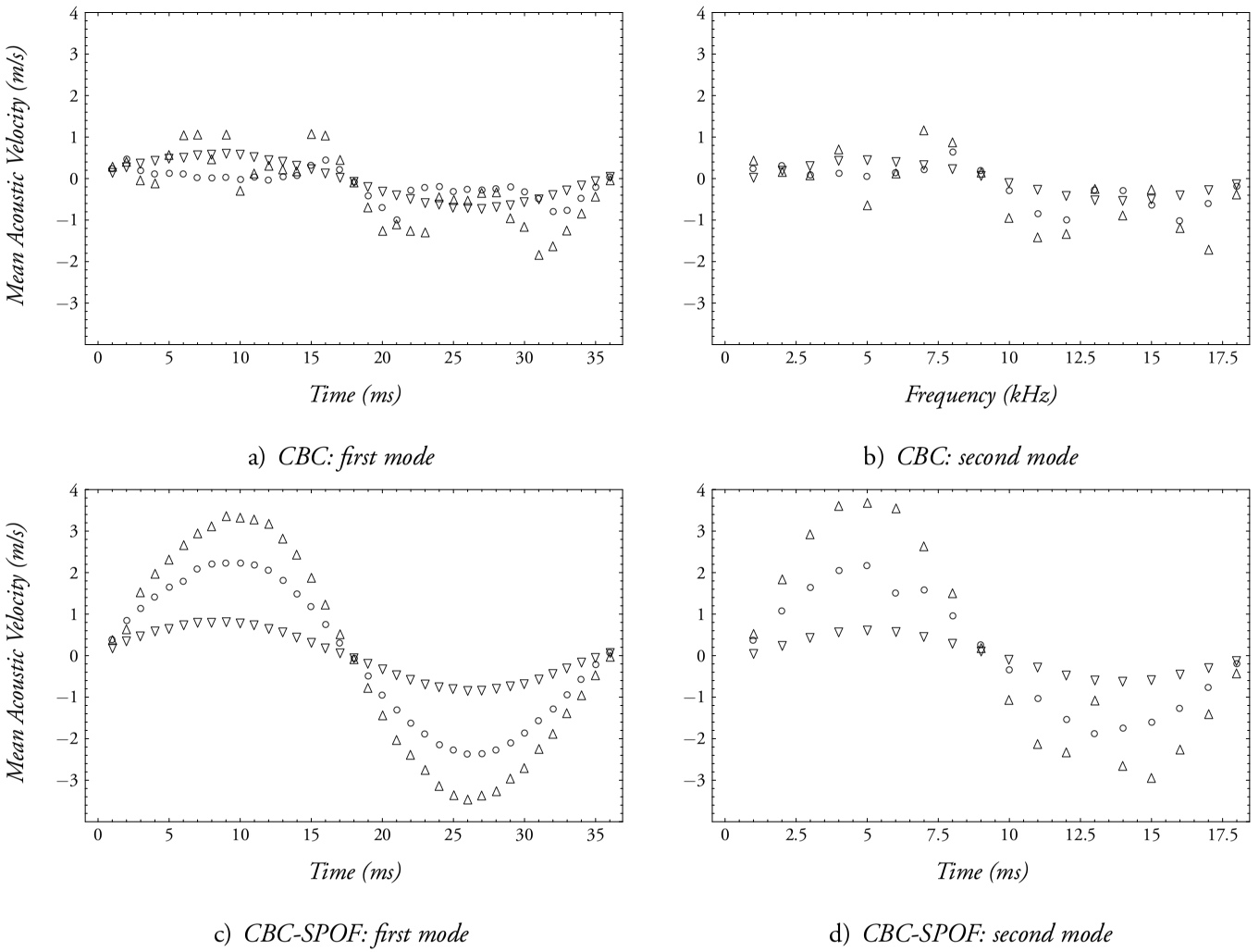

Figure 6.9: *Transversal mean acoustic velocity variation of the first two modes of the tube, measured at* 23 *cm away from the loudspeaker (*$0.19\,\lambda_1$, $0.37\,\lambda_2$*), for different sound intensities. First mode:* 142.0 *dB (▽), 151.2 dB (○) and* 155.0 *dB (△). Second mode:* 143.4 *dB (▽),* 153.0 *dB (○) and* 156.9 *dB (△).*

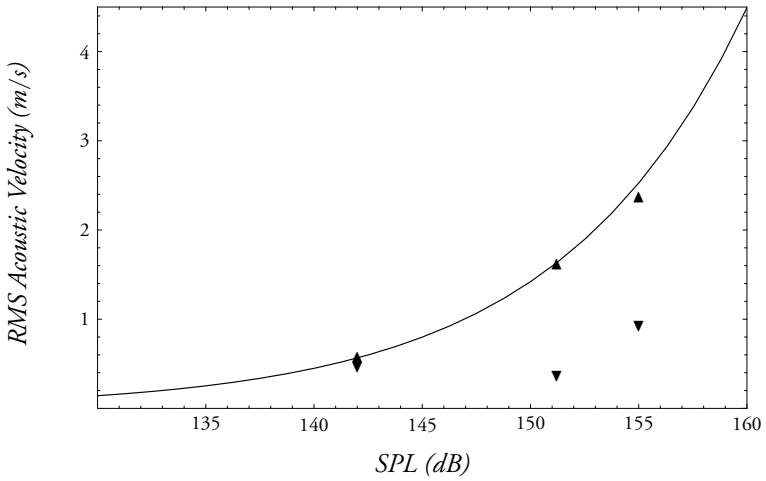

a) *First mode,* $x = 0.19\,\lambda_1$.

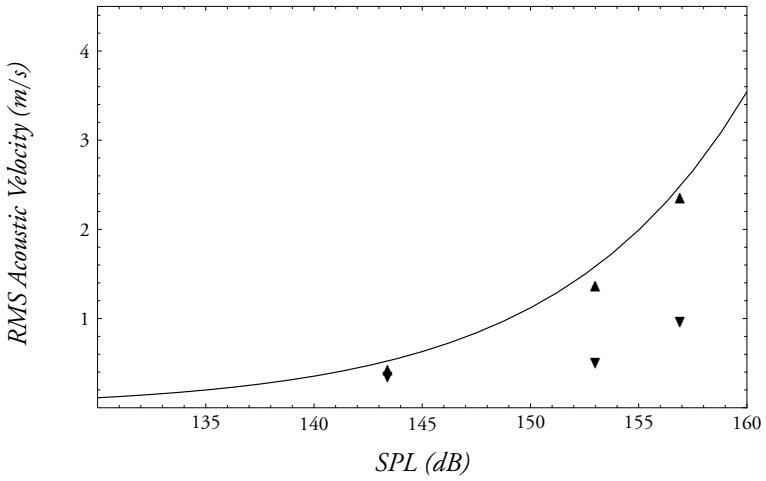

b) *Second mode,* $x = 0.37\,\lambda_2$.

Figure 6.10: *Variation of RMS acoustic velocity at* 23 *cm away from the loudspeaker with SPL measured at the rigid end. A comparison between the data analysed by CBC (▼) and CBC-SPOF (▲) is given together with the theoretical values (—). The RMS acoustic velocities are calculated by the values presented in Figure (6.9).*

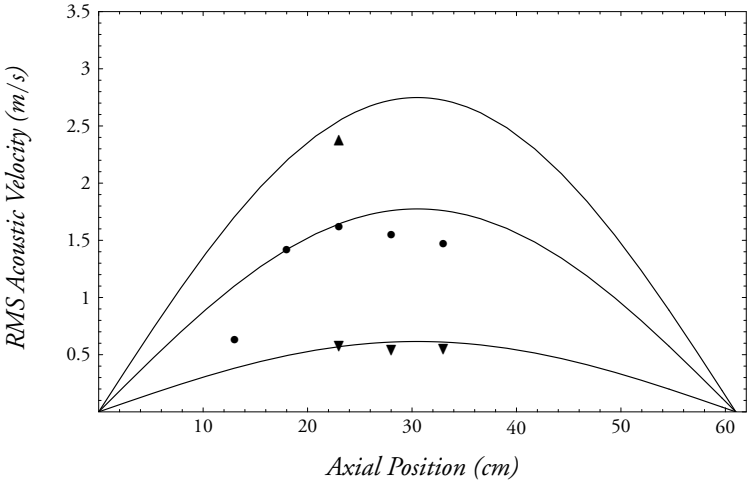

a) *First mode,* 142.0 *dB (▼), 151.2 dB (●) and* 155.0 *dB (▲)*

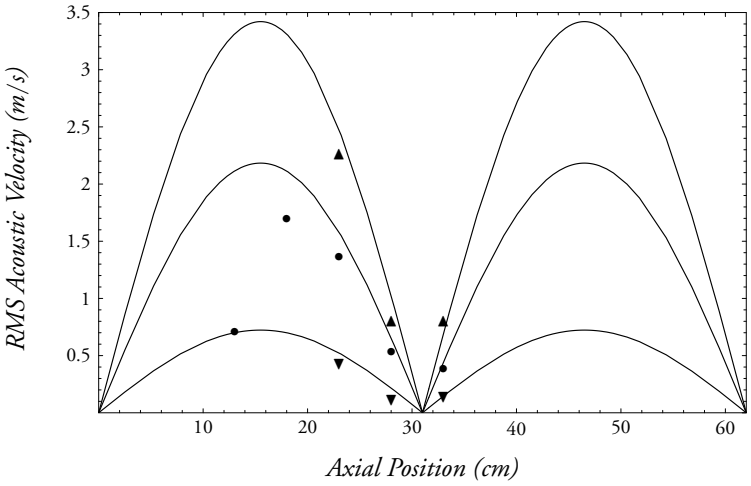

b) *Second mode,* 143.4 *dB (▼), 153.0 dB (●) and* 156.9 *dB (▲).*

Figure 6.11: *Variation of RMS acoustic velocity as a function of the axial position. All values are obtained by CBC-SPOF processing. The solid lines show the corresponding theoretical standing wave pattern of a tube with perfectly rigid terminations. The loudspeaker is located at* $x = 0$ *cm and the rigid end is at* $x = 62$ *cm.*

a tube with perfectly rigid terminations is also given. The results around the anti-node are in a good agreement with the predicted values. However, the measurements around the nodes are biased towards lower velocities. It seems that this bias is independent of the absolute value of the acoustic velocity.

Another type of deviation from the theoretical values is evident at positions close to the loudspeaker ($x = 0$ cm) where there is an acoustic velocity drop. This may be explained by pointing out the fact that as the loudspeaker termination is not absolutely rigid, there is no acoustic velocity node around this position. This implies that the standing wave pattern around the loudspeaker has a distorted form.

6.3 Streaming

6.3.1 Steady Streaming Visualisation

In order to investigate the presence of streaming, a measurement was carried out to visualise the tracer particles on a time-averaged basis.

Unlike the other measurements in this work, this experiment is a single-frame multiple-exposure measurement. An exposure signal of the length of a few acoustic cycles is sent to the camera (where each acoustic cycle is determined by the frequency of the sinusoidal sound wave signal). During the exposure signal, illumination pulses at the frequency of the sound wave signal are sent to the laser. For a better resolution, a lens of higher magnification was used (Lens *B* in Table (5.1)). The result is a super-imposed collection of particle-images.

In order to verify the reliability of the measurement, this test was carried out on an object connected to an electrical shaker vibrating at a frequency of 2 kHz. Figure (6.12a) shows the result for the first 20 cycles of the vibration of the object when it starts to oscillate. It may be seen that after around 10 cycles the object reaches equilibrium where its image intensity is higher.

A similar procedure was applied to the tracer particles in the first resonance of the tube around the anomalous location along the tube. In order to ensure that the sound field was in its equilibrium state, the measurement was taken after 100 acoustic cycles. To avoid any streaks, each illumination signal was synchronised to be sent around the phase position corresponding to zero acoustic velocities. Figure (6.12b) shows the super-positioning of the particle-images for 10 acoustic cycles. The expected super-position pattern would be a set of regularly-

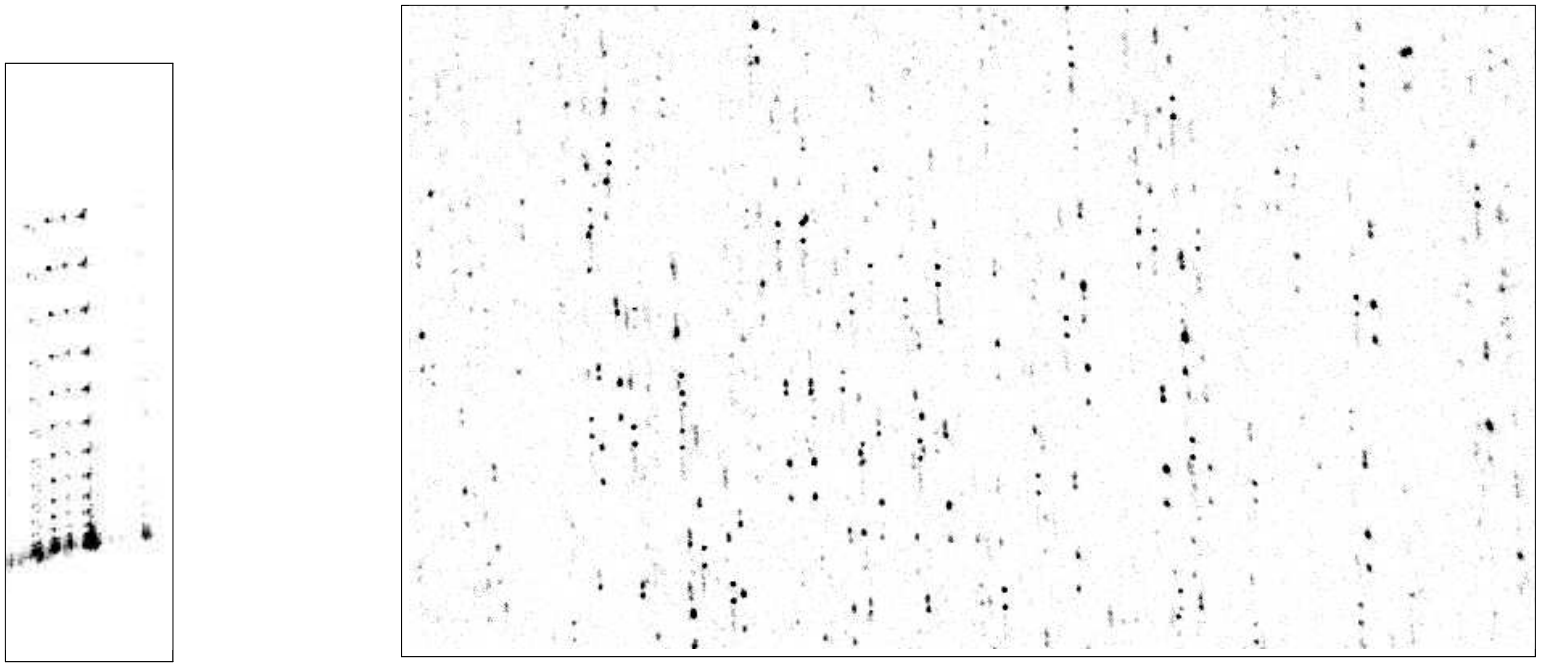

a) *Object on an electrical shaker.* b) *Visualisation of the tracer particles at the first resonance of the tube with a SPL of* 151.2 *dB. The measurement was performed around the middle of the tube.*

Figure 6.12: *The equilibrium test. For a better visualisation, the images are filtered.*

spaced particle-images corresponding to the number of recorded acoustic cycles. However, unexpectedly, this number for each individual particle-image does not exceed more than 2. The cause of this result will be investigated later in §6.5.2.2.

6.4 In-Plane Noise

An important outcome of the previously presented acoustic PIV measurements is the deviation of the experimental acoustic velocities from their expected values. The deviation is observed to be a function of space, time, and sound intensity but *not* the predicted or measured value of the acoustic velocity. The latter implies that the deviation cannot be immediately linked to the upper-limit restriction of the acoustic PIV system. In order to explain the anomalous behaviour of the measurement system, two main questions are investigated. First, an attempt is made to address the source of the deviation. Secondly, based on the cause of the anomaly, means to minimise the deviation are demonstrated or suggested.

6.4.1 Probing Correlation Plane

Since the information associated with the motion of the fluid under a PIV measurement is stored in the correlation plane, it is sensible to start tracing the source of the deviation by examining the correlation plane.

Figure (6.13) certifies the correlation planes obtained by some acoustic PIV measurements presented previously, namely, a sound pulse and a standing wave with different values of sound intensities. One common feature shared between the demonstrated correlation planes is the broad peak along the direction of illumination. It will be shown that the presence of this wide peak is due to the narrow height of the light sheet.

The effective height of the light sheet, measured by eye as given in §5.1.3, was around 1 cm. Figure (6.14) shows the illumination profile, visualised by the seeding particles, as recorded by the CCD camera. The illumination duration of this recording was 0.1 ms which is the same duration used in the presented measurements. The image indicates that the effective height of the recorded pulsed illumination profile is of the order of 1 mm which is about 10% of the one of continuous illumination profile as measured by eye. One reason behind this is the lack of sensitivity of the CCD chip to low-power light. As a trade-off, this deficiency may be compensated by increasing the illumination power.

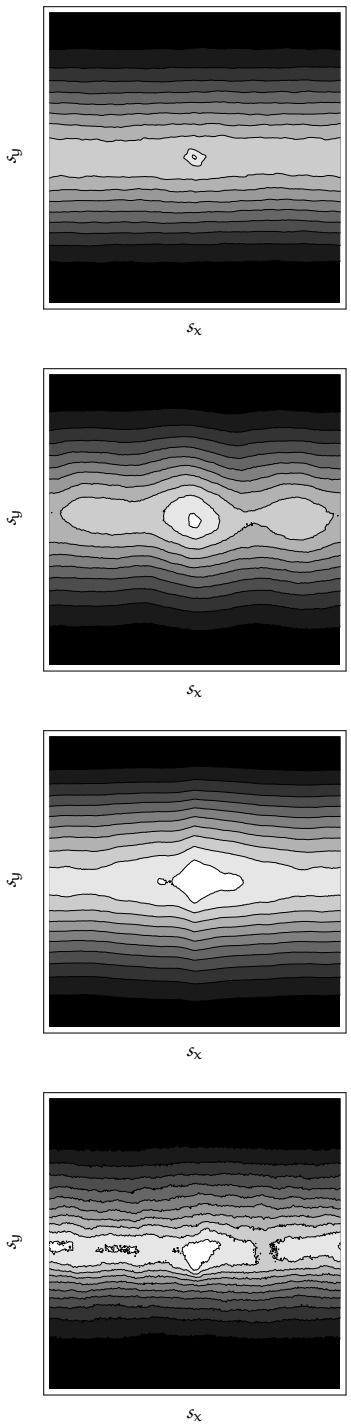

a) *Correlation plane of a sound pulse (Figure 6.4).*

b) *Correlation plane of the extremum of a standing wave (Figure 6.9c) with a SPL of* 142.0 *dB.*

c) *Correlation plane of the extremum of a standing wave (Figure 6.9c) with a SPL of* 151.2 *dB.*

d) *Correlation plane of the extremum of a standing wave (Figure 6.9c) with a SPL of* 155.0 *dB.*

Figure 6.13: *Comparison between the experimental correlation planes corresponding to acoustic motions. All correlation planes are obtained by CBC processing. The brighter regions stand for higher values.*

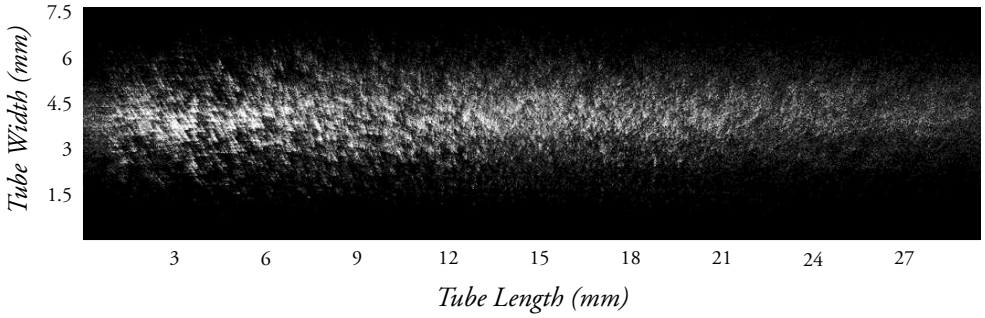

Figure 6.14: *The illumination profile as recorded by the CCD camera with an illumination duration of* 0.1 *ms.*

However, the laser used in this work had an output power of 250 mW which is classed as low to moderate power. Typically, lasers applied in PIV measurements are pulsed lasers with an output energy of 50 to 120 mJ per pulses of duration of 5 ns which is associated with a power of about 10 MW. Accordingly, while it is not possible to directly compare the output power of a continuous laser to a pulsed one, it is reasonable to assume that the laser used in this study is of many orders less powerful than a recommended laser for PIV measurements. However, the fact that the developed set-up, based on the low-power laser, was able to measure velocities up to a few meters per second is significant.

The narrow height of the recorded light sheet, relative to the size of the interrogation areas, causes a strong illumination gradient across the interrogation areas. Consequently, this induces a background correlation peak $\mathcal{R}_C(\vec{s})$ (see §3.5.6.2) to appear as broad peak. The background correlation peak has a Gaussian form with a width of 1/8th of the interrogation area size.

6.4.2 Filtering Correlation Noise

The discussed illumination and recording limitations do not prevent the data acquisition system from losing the displacement signal. In fact, the displacement peak signal is buried under the background correlation noise and may be extracted by an appropriate filter.

Removing the noise of correlation peaks is neither a new idea nor restricted to PIV data processing. Optimising the correlation signal-to-noise ratio was stud-

ied in the 1970s where it was applied to regain radar signals from noisy data (Carter 1976; Knapp and Carter 1976). The approach was first applied to PIV correlation planes by Wernet and Edwards (1988) based on optical correlators. More recently, an extension is implemented by Wernet (2005) where the author demonstrates the effectiveness of *phase-only filters* (*POF*), in particular *Symmetric phase-only filter* (*SPOF*), on PIV image evaluation. The basis of phase-only correlation is matching by the phase of the Fourier transformed data. This is in contrast to the traditional method which tries to match based upon the amplitude of the frequency domain. The significant advantage of phase matching over amplitude matching is that the phase component stores information about the *position* of the input objects, while the amplitude component saves information about their *size*. Correlation obtained by position-only matching not only yields a stronger displacement peak, but also fades the rest of the peaks remarkably, which may be counted as noise. Since the signal of interest in a PIV analysis is the displacement peak, SPOF effectively eliminates the unwanted peaks including background correlation.

The application of SPOF in recovering acoustic displacements measured by low-light PIV is manifested in this work (§6.2). Figure (6.15a) illustrates a correlation plane obtained by CBC which uses Fourier amplitude matching. The correlation plane, corresponding to a PIV image recorded by the previously mentioned narrow illumination, clearly contains a wide background correlation peak which conceals the displacement peak. The displacement peak, as shown in Figure (6.15b), is retrieved by using phase-only correlation.

6.5 Out-of-Plane Noise

6.5.1 Acoustic Motion Visualisation

A sound field visualisation experiment with high-magnification was set up to record the microscopic motion of the particle-sources. The aim of the test was to provide a direct observation of the motion of the particle-sources under the anomalous condition using the existing PIV set-up. The specifications of the measurements are as described in §6.2.1, the only difference being the use of a camera lens of greater magnification (Lens *B* in Table (5.1)).

Figures (6.16) and (6.17) show visualisations of the sound field generated when the tube was driven at its first natural frequency. The visualisations were

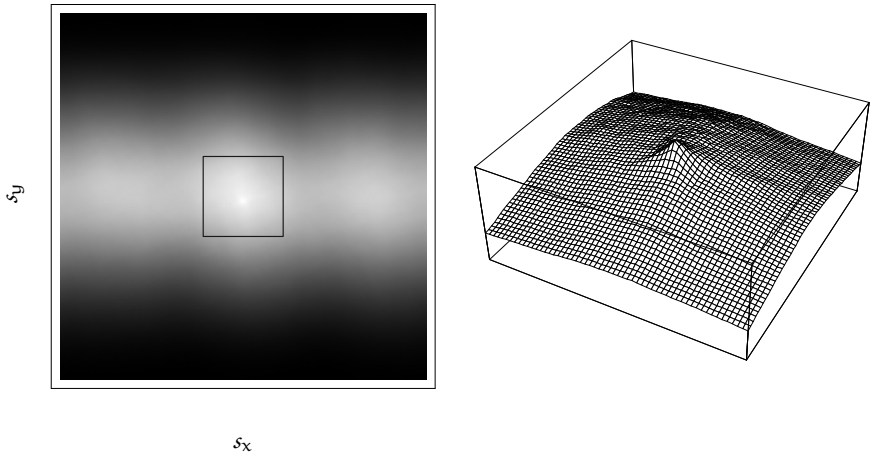

a) *CBC*

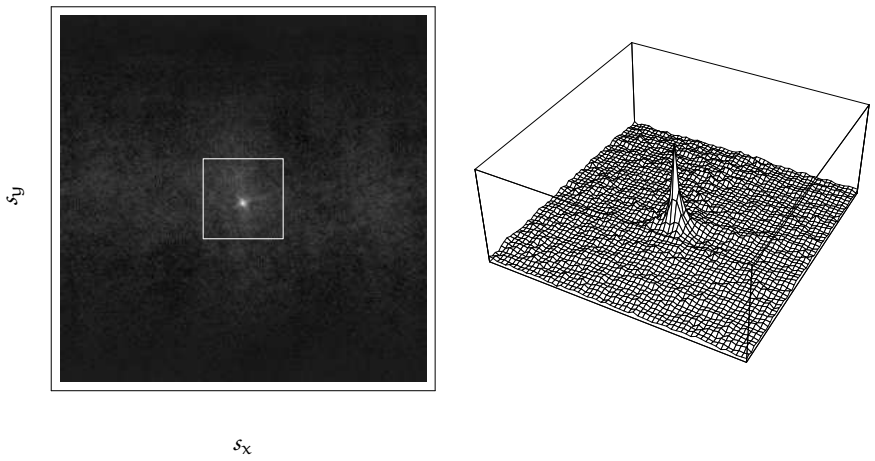

b) *CBC-SPOF*

Figure 6.15: *Comparison between correlation planes obtained by Fourier amplitude matching (CBC) and phase-only matching (CBC-SPOF). The three-dimensional plots correspond to the indicated square regions about the displacement peaks. The correlation plane is the same as in Figure (6.13b).*

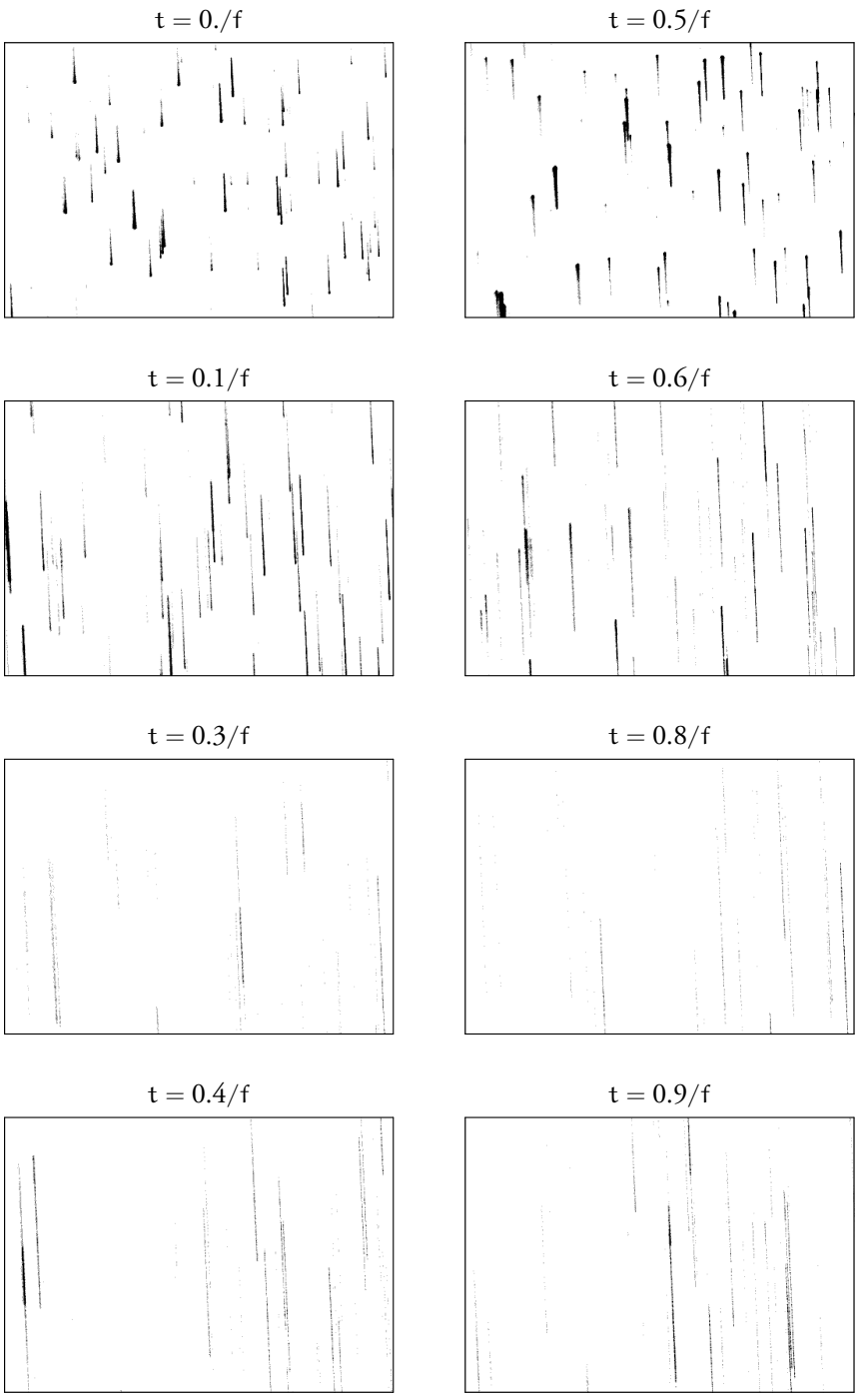

Figure 6.16: *Visualisation of sound field in the non-anomalous location of the tube.*

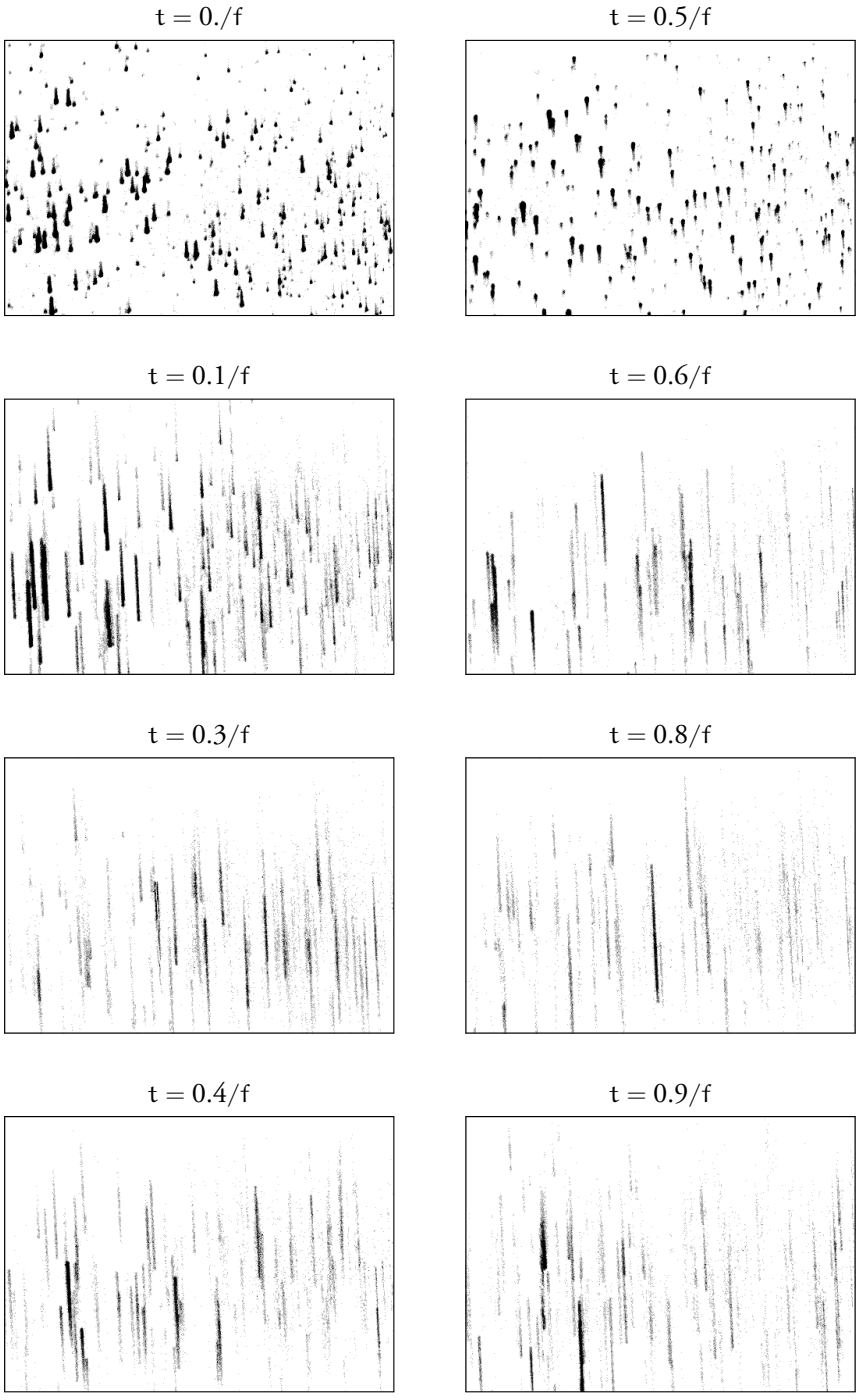

Figure 6.17: *Visualisation of sound field in the anomalous location of the tube.*

carried out at, respectively, the non-anomalous and anomalous positions inside the tube and at selected times within an acoustic cycle. For ease of observation, negatives of the images are presented. The visualised sound field is comparable to that presented in the works of Brandt and Hiedemann (1936) and Hann (1995) (see Figures (4.3a) and (4.3b) on page 61); however, the temporal resolution achieved in this study is of the order of 100 times greater than that of the mentioned works. Consequently, instead of having a 'dumbbell-shape' recorded over a few acoustic cycles, each particle-image is expected to appear as a streak at the extremum points of the acoustic velocity and as a 'half-dumbbell-shape' as they get closer to smaller velocities.

A qualitative comparison between the two sets of visualisations shows that the streaks recorded under the anomalous condition are relatively shorter and of stronger intensities than the non-anomalous streaks corresponding to the same phase. This is an unexpected result as the anomalous streaks, whether associated with higher sound intensities or regions around the velocity node, should be generally longer than the non-anomalous streaks. A more surprising outcome is observed about the temporal extremum points, $t = 0.3/f$ and $t = 0.8/f$. At these points the non-anomalous streaks have a predictably uniform intensity profile. However, the anomalous streaks of the same phases generated an intensity profile which looks like full-Gaussian or partial-Gaussian.

6.5.2 Discussions

The unexpected behaviour of the visualised acoustic motion may be interpreted once assuming that, during the illumination time, the particle-sources were laid on a plane parallel to and within the light sheet volume; and once assuming that they have a considerable displacement normal to the light sheet while they were recorded.

6.5.2.1 In-Plane Motion

The first of the above assumptions implies that the recorded streaks reflect the true two-dimensional motion of the particle-sources. Accordingly, it may be argued that particle-sources actually do not perform the expected harmonic oscillations. One may go further and expand this possibility to whether the source of the unpredicted motion is from the fluid flow itself or due to the fact that the particle-sources do not follow the flow faithfully.

The former hypothesis was rejected by measuring the acoustic pressure using a probe microphone. The measurement, which was carried out similarly to the description in §6.2, confirmed the sinusoidal form of acoustic pressure variation implying the same result for acoustic velocity.

Under the measurement conditions, given a frequency of the order of 10^2 Hz and SPL of less than about 160 dB, the infidelity of the particle-sources to the fluid flow in the sound field does not agree with the classical theory presented in §4.5.2.2. Even by neglecting the measurement conditions, the classical theory simply predicts the infidelity in the sense of attenuation in the amplitude of oscillation. This makes tracer particles infidelity to be a less-likely source of anomaly.

6.5.2.2 Out-of-Plane Motion

The idea of the motion of the particle-sources during the illumination time may be supported by a number of reasons. First, the stronger intensity of the anomalous particle-images may imply their motion normal to the recording plane, therefore, creating shorter streaks. Secondly, the unexpected Gaussian profiles of the anomalous streaks, at the temporal extremum points, can prove that the particle-sources cross the light sheet volume. Consequently, the Gaussian profile of the light sheet thickness is 'mapped' to the expected uniform profile of the streaks making them appear as Gaussian streaks. Hence, according to whether the particle-sources cross the light sheet volume completely or partially, they generate streaks with full-Gaussian or partial-Gaussian profiles, respectively. Finally, considering the out-of-plane motion of source particles explains the streaming visualisation pattern discussed formerly (Figure 6.12a) by the fact that the time-averaged motion normal to the light sheet cuts the continuation of the regularly-spaced particle-images.

One reason behind the out-of-plane motion could be due to the angle between the light sheet normal and the tube axis. In the PIV set-up used for the measurement of acoustic oscillatory motions, it is assumed that the normal vector of the light sheet is perpendicular to the axis of the tube. This prevents all the particle-sources initially located within the illumination volume from exiting the volume while avoiding new particle-sources simultaneously entering. However, in practice this angle may deviate from 90°.

Let the deviation angle be denoted by ϑ. From Equation (3.5.25), for a

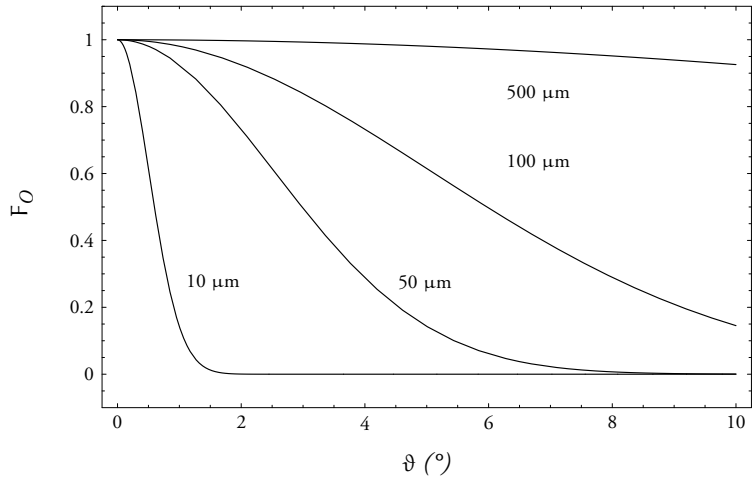

Figure 6.18: *Variation of out-of-plane loss-of-correlation with the deviation of the angle between the Gaussian light sheet normal and the tube axis for different values of thickness of light sheet. The acoustic motion corresponds to an extremum point in space-time with* $v_0 = 2$ *m/s and* $\tau_i = 0.2$ *ms for the first mode of the tube.*

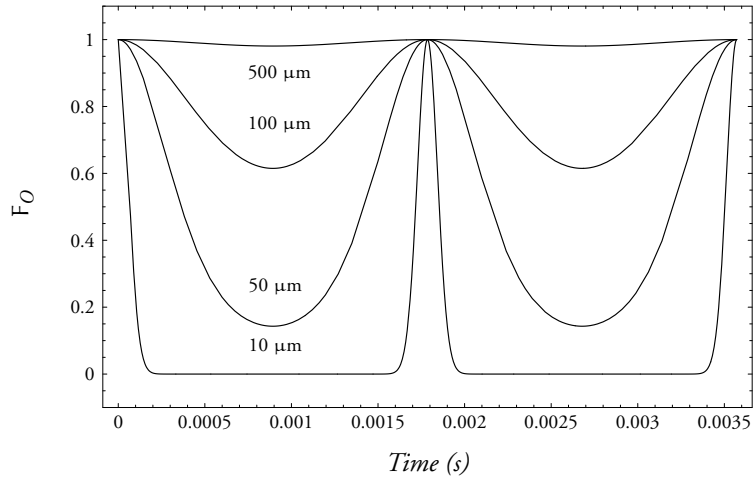

Figure 6.19: *Variation of out-of-plane loss-of-correlation with time at* $\vartheta = 5\,°$, $v_0 = 2$ *m/s and* $\tau_i = 0.2$ *ms for the first mode of the tube.*

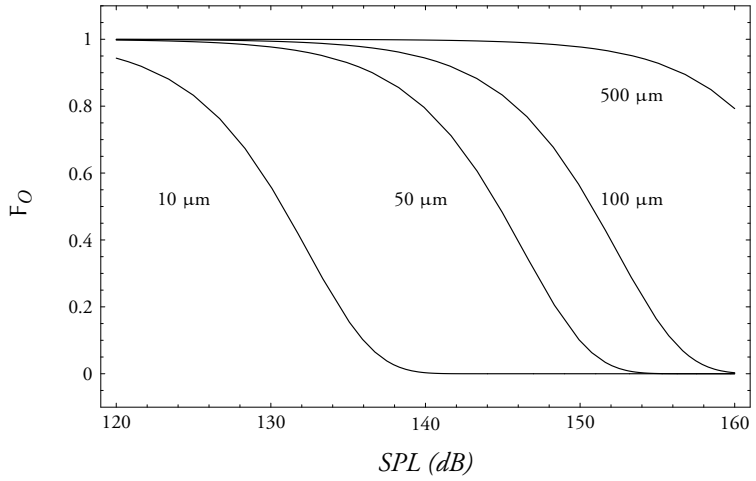

Figure 6.20: *Variation of out-of-plane loss-of-correlation with SPL at the velocity node of the first mode of the tube with* $\vartheta = 5\,°$ *and* $\tau_i = 0.2$ *ms.*

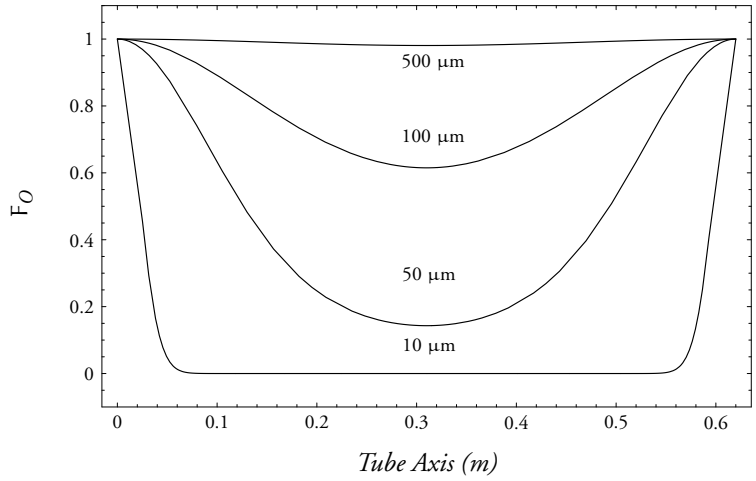

Figure 6.21: *Variation of out-of-plane loss-of-correlation with axial position at a temporal extremum with* $\vartheta = 5\,°$ *and* $\tau_i = 0.2$ *ms.*

Gaussian intensity profile of the light sheet, the out-of-plane loss-of-correlation F_O may be given as

$$F_O(\Delta z_L) = \frac{\sqrt{\pi}}{4}\,\Delta z_L \exp\left(-8\left(\frac{x + (v_0\,\sin(k_n x)\,\sin(\omega_n t))\,\tau_i\,\sin(\vartheta)}{\Delta z_L}\right)^2\right), \quad (6.5.1)$$

where v is the magnitude of the acoustic velocity, τ_i is the duration of the illumination and Δz_L is the thickness of the light sheet. Since the determining experimental parameter in this equation is the light sheet thickness, it is worthy to analyse the behaviour of F_O as a function of Δz_L.

Figures (6.18) to (6.21) examine the variations of $F_O(\Delta z_L)$ as a function of deviation angle, time, SPL, and axial position, respectively. In order to apply these results to the previous measurements, F_O is calculated for the first mode of the tube under investigation with an illumination duration of 0.2 ms. The graphs show a significant drop of valid detection of the correlation peak for an effective light sheet thickness of about 0.1 mm and less. Accordingly, the valid detection probability decreases at some points in space-time-intensity, namely around the extremum points of the phase and the velocity node of the tube. This is in general agreement with the previous unexpected observations.

Based on the calculated out-of-plane loss-of-correlation, and assuming that the in-plane loss is negligible, the anomalous measured velocity may be described as

$$v_n^*(x, t, \Delta z_L) = F_O(\Delta z_L)\, v_0\, \sin(k_n x)\, \sin(\omega_n t). \quad (6.5.2)$$

Figure (6.22) compares this theory to the experimental data presented in §6.2.1. The fitted curve is associated with a Gaussian light sheet with a thickness of about 0.05 mm and deviation angle of 9°. Since the height of the light sheet, as recorded by the camera, was observed to be around 10% of its actual value (§6.4.1), it is reasonable to assume that the same ratio is applicable to the thickness of the light sheet.

It is possible to decrease or eliminate the out-of-plane noise using a more powerful light source. In this case, the main benefit of more light energy is to produce a thicker light sheet and *not* obtain higher quality particle-images. Another option, which is harder to achieve, is to carefully align the laser sheet relative to the axis of the tube. Moreover, the use of a camera with a higher sensitivity allows shorter illumination pulses to be achieved without a significant loss of the effective light sheet thickness.

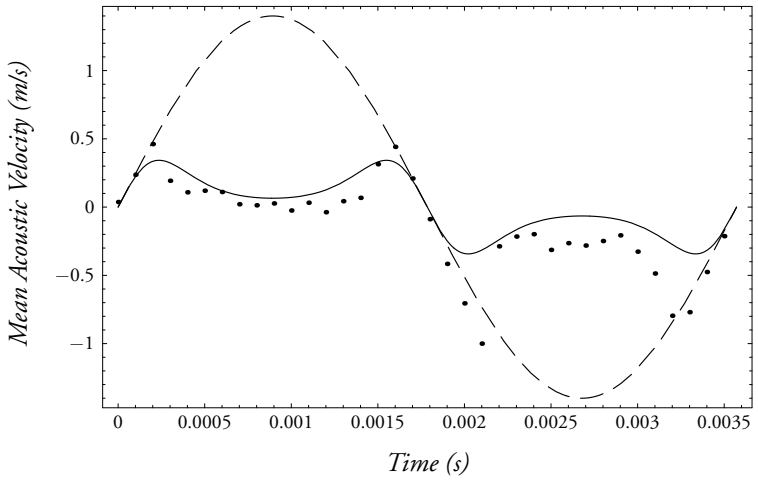

Figure 6.22: *Comparison between CBC-processed experimental acoustic velocities (•), the theoretical fit considering the out-of-plane effect (—) and the expected values (––) for the first mode of the tube with SPL* $= 151.2$ *dB and* $\tau_i = 0.2$ *ms. The fitted curve corresponds to a Gaussian light sheet with a thickness of* 0.05 *mm and a deviation angle of* $9°$.

Chapter 7

Closing Remarks

7.1 Summary and Conclusions

7.1.1 Introducing acoustic PIV

While a lot of research has been carried out on the acoustic velocimetry of low-speed flows, there is a perceptible lack of literature in measuring acoustic velocities particularly by non-intrusive whole-field means (§4.3). This study is an attempt to fill this absence by introducing the technique of acoustic PIV.

The verification of the principles of PIV (§3.2.3) in the presence of a sound field has been carried out by examining various interactions between the measurement components and the sound field (§4.4). Among these interactions, the effect of sound fields on the tracer particles was found to be negligible for low to moderate acoustic frequencies and sound intensities.

7.1.2 Scanning Sound Waves

The main idea behind the acoustic PIV experimental set-up is to be able to measure the velocity of the sound wave of interest at a high-enough temporal rate. An absolute scanning rate of up to 5 kHz has been achieved in this study, which is suitable for the precise measure of the time variation of sound waves within an acoustic cycle (§6.2.1).

The sound wave scanning process has been successfully applied to both sound pulses (§6.1) and sinusoidal waves (§6.2). Variation of acoustic velocities with sound intensity and the standing wave pattern of the first two modes of a simple

tube has been studied. In addition, more improved visualisations of acoustic and hydrodynamic motions were presented.

7.1.3 Low-Light High-Speed PIV

The laser used in this study was a CW solid-state laser externally triggered to produce quasi-pulses. The power of this laser was of many orders lower than typical pulsed lasers used in PIV measurements. Considering the fact that measuring acoustic velocities with a standard PIV system is near to the limitation border of the technique, it is a challenging task to perform acoustic PIV with low-power light sources.

Two main problems were encountered using the low-light system. The first one was due to the narrow height of the Gaussian light sheet used in this study which caused a significantly broad background peak in correlation planes. This noise, referred to as the in-plane noise, was successfully eliminated using a phase-only PIV image processing method (§6.4). The second problem was the presence of out-of-plane noise which was caused by the narrow thickness of the light sheet. It was demonstrated that this noise led to a excessive loss of valid detection at specific space-time-intensity points (§6.5).

7.2 Future Research

7.2.1 Instantaneous Measurement of Impedance

One immediate application of acoustic PIV is the calculation of acoustic impedance. While it is possible to measure the acoustic pressure independently using conventional methods, it is desirable and more convenient to calculate the pressure from the velocity vector-map (Imaichi and Ohmi 1983). Combining this method with acoustic PIV has the advantage of measuring variation of impedance simultaneously and non-intrusively. Estimating the acoustic pressure via the acoustic velocity is based on the numerical calculation of the spatial gradient of the velocity, implying that the velocity vector-map must be whole-field with valid representations of the sound field velocity values in each interrogation area. Evidently, this requires the tracer particles to be in the absolute fidelity phase.

Measurement of the impedance in this way has potential applications in noise reduction or the study of musical instruments. One attractive benefit of employ-

ing acoustic PIV in these applications is that the technique is independent of the shape of the flow passage, enabling acoustic measurements to be carried out in complex geometries.

7.2.2 Aerosol Measurements

Although this work is based on using aerosol particles to measure sound fields, acoustic PIV may be employed to use sound fields in the measurement of aerosols. Velocity vector-maps corresponding to sound fields store more information than just the acoustical properties. Indeed, the velocity distribution extracted from an acoustic PIV measurement contains data about the size distribution of the tracer particles (§4.5.3.2). In addition, it is possible to study the motion and internal interactions of aerosol particles in sound fields using acoustic PIV.

III

Appendices

Appendix A

Time Series

Broadly speaking, physical phenomena are processes varying in time, e.g. 'wave-like' structures. These processes are known as *time series*. In the following appendix, those elements of time series theory which are referred to in this study are presented in a compact form. The concepts are mainly taken from Priestly (1981).

A.1 Terminology

Definition A.i. Any functioning which can yield one of many likelihoods is called an *experiment* $\mathfrak{E}$.

Definition A.ii. All possible outcomes of an experiment $\mathfrak{E}$ are referred as the *sample space* $\underline{\Omega}$ of that experiment. Each single possibility in a sample space is named an *element* Ω.

Definition A.iii. Any sub-set of a sample space $\underline{\Omega}$ corresponding to an experiment $\mathfrak{E}$ is defined as an *event* $\mathcal{E}$ of that experiment.

Definition A.iv. Assume that there is a mapping from every event $\mathcal{E}$, belonging to a sample space $\underline{\Omega}$, to a real number $p(\mathcal{E})$. The number $p(\mathcal{E})$ is the *probability* of the event $\mathcal{E}$ and fulfills the following conditions

$$0 \leqslant p(\mathcal{E}) \leqslant 1 \tag{A.1.1a}$$

$$p(\underline{\Omega}) = 1; \tag{A.1.1b}$$

Definition A.v. For every element Ω, belonging to a sample space $\underline{\Omega}$, there exists a unique real number $X(\Omega)$ called a *random variable*.

A.2 Univariate Distributions

Consider, for any real number x, the event $\mathcal{E}(x)$ is given by

$$\mathcal{E}(x) = \{\Omega; (\Omega \in \underline{\Omega}) \wedge (X(\Omega) \leqslant x)\}. \tag{A.2.1}$$

The *univariate distribution function* $\mathcal{F}(x)$ of the random variable $X(\Omega)$ is defined as the probability of the event $\mathcal{E}(x)$, i.e.

$$\mathcal{F}(x) = p[\mathcal{E}(x)]. \tag{A.2.2a}$$

The distribution function may also be expressed explicitly in terms of the corresponding random variable:

$$\mathcal{F}(x) = p[X \leqslant x], \tag{A.2.2b}$$

where $p[X \leqslant x]$ is the probability for the random variable X.

A.2.1 Discrete Distributions

Assume X is a discrete random variable whose possible values are restricted to the set $\{x_1, x_2, x_3, \ldots\}$. The discrete probability p_i for X has the following properties

$$p_i = p[X = x_i], \tag{A.2.3a}$$

$$0 \leqslant p_i \leqslant 1, \tag{A.2.3b}$$

$$\sum_i p_i = 1, \tag{A.2.3c}$$

where i is a natural number. The discrete distribution function for p_i is given by

$$\mathcal{F}(x) = \sum_{i;\, x_i \leqslant x} p_i. \tag{A.2.4}$$

The mean and variance of the discrete distribution function $\mathcal{F}(x)$ can be calculated from

$$\mu = \sum_i x_i p_i, \tag{A.2.5}$$

and

$$\sigma^2 = \sum_i (p_i - \mu)^2. \tag{A.2.6}$$

A.2.2 Continuous Distributions

The random variable X is said to be continuous if we can define a function $f(x)$ with the following specifications for all x

$$f(x) = \lim_{\delta x \to 0} \frac{p[x < X \leqslant x + \delta x]}{\delta x}, \tag{A.2.7a}$$

$$f(x) \geqslant 0, \tag{A.2.7b}$$

$$\int_{-\infty}^{+\infty} f(x)\,\mathrm{d}x = 1. \tag{A.2.7c}$$

$f(x)$ is called the *probability density function* (*PDF* of X. Given the PDF of a random variable, the corresponding continuous distribution function may be calculated by

$$\mathcal{F}(x) = \int_{-\infty}^{x} f(x)\,\mathrm{d}x\,. \tag{A.2.8}$$

The mean and variance of the continuous distribution function $\mathcal{F}(x)$ is given by

$$\mu = \int_{-\infty}^{+\infty} x f(x)\,\mathrm{d}x\,, \tag{A.2.9}$$

and

$$\sigma^2 = \int_{-\infty}^{+\infty} (x - \mu)^2 f(x)\, dx. \tag{A.2.10}$$

A.2.3 The Expectation Value

The statistical properties of a distribution function can be presented in a compact form by the *expectation operator* $\mathcal{E}\{\ \}$. The *expectation value* of a given function $g(X)$ is defined as

$$\mathcal{E}\{g(X)\} = \sum_i g(x_i) p_i, \tag{A.2.11}$$

when X is discrete and

$$\mathcal{E}\{g(X)\} = \int_{-\infty}^{+\infty} g(x) f(x)\, dx, \tag{A.2.12}$$

when X is continuous.

Using the expectation operator, the definitions of mean and variance can be re-written as

$$\mu = \mathcal{E}\{X\}, \tag{A.2.13}$$

and

$$\sigma^2 = \mathcal{E}\{(X - \mu)^2\}. \tag{A.2.14}$$

A.2.4 Special Distributions

A.2.4.1 Binomial Distribution

The *binomial distribution with parameter* n is defined as

$$p_{i;n} = \frac{n!}{i!\,(n-i)!}\, p^i (1-p)^{n-1}, \quad i = 1, 2, 3, \ldots, n. \tag{A.2.15}$$

The distribution describes a sample space with only two elements, one of which has a probability p of occuring. The discrete probability $p_{i;n}$ represents the likelihood of n outcome with probability p.

A.2.4.2 Poisson Distribution

Consider the binomial distribution Equation (A.2.15) when $n \to \infty$ and $p \to 0$ with the condition $np = a$, where a is a positive constant. It can be shown that $p_{i;n}$, with the given assumptions, can be written

$$p_{i;a} = \frac{a^i}{i!} e^{-a}, \quad i = 1, 2, 3, \ldots, n. \tag{A.2.16}$$

This discrete probability is known as the *Poisson distribution with parameter* a.

A.2.4.3 Gaussian Distribution

Assuming that x is a continuous random variable, the associated PDF

$$f(x) = \frac{1}{(2\pi\sigma^2)^{\frac{1}{2}}} e^{-\frac{(x-\mu)^2}{2\sigma^2}}, \tag{A.2.17}$$

is said to have a *Gaussian distribution function with parameters* μ *and* σ^2.

A.3 Multivariate Distributions

The rationale behind univariate distributions can be extended to *multivariate distributions* when describing more than a single random variable.

A *multivariate discrete probability distribution* for n discrete values is defined as

$$p_{i_1,i_2,\ldots,i_n} = p[X_1 = x_{i_1}, X_2 = x_{i_2}, \ldots, X_n = x_{i_n}], \tag{A.3.1}$$

with

$$\begin{aligned} i_1 &= 1, 2, \ldots \\ i_2 &= 1, 2, \ldots \\ &\vdots \\ i_n &= 1, 2, \ldots. \end{aligned}$$

For n continuous variables, the *multivariate probability density function* is given

by

$$f(x_1, x_2, \ldots, x_n) = \lim_{\delta x_1, \delta x_2, \ldots, \delta x_n \to 0} \frac{p\,[x_1 < X_1 \leqslant x_1 + \delta x_1,\, x_2 < X_2 \leqslant x_2 + \delta x_2,\, \ldots,\, x_n < X_n \leqslant x_n + \delta x_n]}{\delta x_1 \ \ldots \ \delta x_n}. \tag{A.3.2}$$

Based on Equation (A.2.2b), the definition of the distribution function can be extended to its *cumulative* form:

$$\mathcal{F}(x_1, x_2, \ldots, x_n) = p\,[X_1 \leqslant x_1, X_2 \leqslant x_2, \ldots, X_n \leqslant x_n]; \tag{A.3.3}$$

where for the discrete and continuous random variable it is given by

$$\mathcal{F}(x_1, x_2, \ldots, x_n) = \sum_{i_1; x_{i_1} \leqslant x_1} \sum_{i_2; x_{i_2} \leqslant x_2} \cdots \sum_{i_n; x_{i_n} \leqslant x_n} p_{i_1, i_2, \ldots, i_n}, \tag{A.3.4}$$

and

$$\mathcal{F}(x_1, x_2, \ldots, x_n) = \int_{-\infty}^{x_{i_1}} \int_{-\infty}^{x_{i_2}} \cdots \int_{-\infty}^{x_{i_n}} f(x_1, x_2, \ldots, x_n)\, dx_1 dx_2 \ldots dx_n, \tag{A.3.5}$$

respectively.

A.4 Stochastic Processes

Assume that the outcome of an experiment $\mathfrak{E}$ is a quantity X which is a continuous function of time t. According to definition Equation (A.v), the parameter $X(t)$ is a random variable of the sample space $\underline{\Omega}$ of $\mathfrak{E}$. Let $\underline{\Omega}$ have n elements

$$\{\Omega_1, \Omega_2, \ldots, \Omega_n\},$$

for each time t the experiment $\mathfrak{E}$ can have a set of 'possible outcomes', called *records*, shown by

$$\{X(t, \Omega_1), X(t, \Omega_2), \ldots, X(t, \Omega_n)\}.$$

This set of the likely records is named the *ensemble*. Each single record in the ensemble is called to be a *realisation* and is typically denoted by $X(t, \Omega)$.

Assume that t varies over all its possible values and for each value a record is obtained. In this way, a set of realisations is generated which is referred to as a *stochastic process*[1]. A stochastic process with n random variables is shown by

$$\{X(t)\} \equiv \{X(t_1), X(t_2), \ldots, X(t_n)\},$$

and its corresponding cumulative distribution function is denoted as

$$\mathcal{F}_{X(t_1),X(t_2),\ldots,X(t_n)}(x_1, x_2, \ldots, x_n).$$

The preceding definitions are also valid for discrete random variables. However, in most practical cases, the random variables of a stochastic process is a continuous parameter. This will be assumed in the forthcoming sections sections.

It is worth noting that the parameter t in a stochastic process $\{X(t)\}$ need not necessarily represent time. Depending on the physical implementation of the process, it can be any quantity.

A.4.1 Stationary Univariate Processes

Let a stochastic process for any $t_1, t_2, \ldots, t_n$ be written

$$\{X(t_1), X(t_2), \ldots, X(t_n)\},$$

and the same process observed with any arbitrary delay or *lag* τ be written

$$\{X(t_1 + \tau), X(t_2 + \tau), \ldots, X(t_n + \tau)\}.$$

The process is said to be *stationary* if

$$\mathcal{F}_{X(t_1),X(t_2),\ldots,X(t_n)}(x_1, x_2, \ldots, x_n) = \mathcal{F}_{X(t_1+\tau),X(t_2+\tau),\ldots,X(t_n+\tau)}(x_1, x_2, \ldots, x_n). \tag{A.4.1}$$

A stationary stochastic process describes a physical system in which the statistical properties do not change over time, i.e. the system is in steady-state or equilibrium.

For the rest of this study we assume the processes are stationary.

[1] The so-called *random process*.

A.4.1.1 Mean and Variance

Consider the PDF $f_t(x)$ of the random variable $\{X(t)\}$ of a stationary process. Using Equations (A.2.8), (A.2.9), (A.2.13) and (A.2.14), the mean and variance of this random variable are given by

$$\text{mean}\{X(t)\} \equiv \mathcal{E}\{X(t)\} = \int_{-\infty}^{+\infty} x f_t(x)\, dx = \mu(t), \tag{A.4.2}$$

and

$$\text{var}\{X(t)\} \equiv \mathcal{E}\{ \Big(X(t) - \mu(t) \Big)^2 \} = \int_{-\infty}^{+\infty} \Big(x - \mu(t) \Big)^2 f_t(x)\, dx = \sigma^2(t). \tag{A.4.3}$$

A.4.1.2 Covariance and Correlation Coefficient

The *covariance* of two random variables $X(t_1)$ and $X(t_2)$ is defined as

$$\begin{aligned} \text{cov}\{X(t_1), X(t_2)\} &\equiv \mathcal{E}\{X(t_1)\, X(t_2)\} - \mathcal{E}\{X(t_1)\}\, \mathcal{E}\{X(t_2)\} \\ &= \mathcal{E}\{ \Big(X(t_1) - \mathcal{E}\{X(t_1)\} \Big) \Big(X(t_2) - \mathcal{E}\{X(t_2)\} \Big) \}. \end{aligned} \tag{A.4.4}$$

Parameters $X(t_1)$ and $X(t_2)$ are said to be *uncorrelated* if their covariance is vanished, or equivalently

$$\text{var}\{X(t_1) + X(t_2)\} = \text{var}\{X(t_1)\} + \text{var}\{X(t_2)\}; \tag{A.4.5}$$

otherwise, they are *correlated* random variables.

When the covariance function of two random variables is normalised by their variances, the outcome is named the *correlation coefficient* and is defined as

$$\mathcal{C}\{X(t_1), X(t_2)\} = \frac{\text{cov}\{X(t_1), X(t_2)\}}{\Big(\text{var}\{X(t_1)\}\, \text{var}\{X(t_2)\} \Big)^{\frac{1}{2}}}. \tag{A.4.6}$$

A.4.1.3 Auto-Covariance and Auto-Correlation

Applying Equation (A.4.4) to a stationary process, the covariance of two random variables with lag τ is given by

$$\text{cov}\{X(t), X(t+\tau)\} = \mathcal{E}\{ \Big(X(t) - \mu(t)\Big) \quad \Big(X(t+\tau) - \mu(t+\tau)\Big) \ \}. \tag{A.4.7}$$

It can be shown that this covariance is a only a function of τ. Therefore, it can be written as

$$\mathcal{R}(\tau) = \text{cov}\{X(t), X(t+\tau)\}. \tag{A.4.8}$$

The function $\mathcal{R}(\tau)$ is known as the *auto-covariance* of the process $\{X(t)\}$.

The normalised value of $\mathcal{R}(\tau)$ is named the *auto-correlation function* and is defined as

$$\rho(\tau) = \frac{\mathcal{R}(\tau)}{\mathcal{R}(0)}, \tag{A.4.9}$$

which may be also written in terms of the correlation coefficient as

$$\rho(\tau) = \mathcal{C}\{X(t), X(t+\tau)\}. \tag{A.4.10}$$

In the case of a stationary process with complex random variables, the associated auto-covariance function is defined by

$$\begin{aligned} \mathcal{R}(\tau) &= \text{cov}\{X(t), X(t+\tau)\} \\ &= \mathcal{E}\{ \Big(X(t) - \mathcal{E}\{X(t)\}\Big)^* \quad \Big(X(t+\tau) - \mathcal{E}\{X(t+\tau)\}\Big) \ \}, \end{aligned} \tag{A.4.11}$$

where the sign $(^*)$ denotes the complex conjugate.

A.4.2 Stationary Bivariate Processes

So far, the statistical properties of stationary processes in their univariate form have been presented. We now focus on the relationship between two stationary processes.

Consider two stationary univariate processes with continuous complex random variables, $\{X_1(t)\}$ and $\{X_2(t)\}$. The process $\{X_1(t), X_2(t)\}$ is known as a *stationary bivariate process* if $\text{cov}\{X_1(t), X_2(t+\tau)\}$ is a pure function of τ.

In a similar way to equation Equation (A.4.11), the auto-covariance functions of $\{X_1(t)\}$ and $\{X_2(t)\}$ can be defined as

$$\mathcal{R}_{11}(\tau) = \text{cov}\{X_1(t), X_1(t+\tau)\}, \tag{A.4.12a}$$

$$\mathcal{R}_{22}(\tau) = \text{cov}\{X_2(t), X_2(t+\tau)\}; \tag{A.4.12b}$$

respectively. The corresponding auto-correlation functions are given by

$$\rho_{11}(\tau) = \frac{\mathcal{R}_{11}(\tau)}{\mathcal{R}_{11}(0)}, \tag{A.4.13a}$$

$$\rho_{22}(\tau) = \frac{\mathcal{R}_{22}(\tau)}{\mathcal{R}_{22}(0)}. \tag{A.4.13b}$$

A.4.2.1 Cross-Covariance and Cross-Correlation

To describe the correlation 'between' two distinct processes, we introduce the concept of *cross-covariance* with lag τ defined by

$$\begin{aligned} \mathcal{R}_{21}(\tau) &= \text{cov}\{X_1(t), X_2(t+\tau)\} \\ &= \mathcal{E}\{ \Big(X_1(t) - \mathcal{E}\{X_1(t)\}\Big)^* \Big(X_2(t+\tau) - \mathcal{E}\{X_2(t+\tau)\}\Big) \}. \end{aligned} \tag{A.4.14}$$

The normalised value of $\mathcal{R}_{21}(\tau)$ is called the *cross-correlation function* and is written

$$\rho_{21}(\tau) = \frac{\mathcal{R}_{21}(\tau)}{\Big(\mathcal{R}_{11}(0)\,\mathcal{R}_{22}(0)\Big)^{\frac{1}{2}}}, \tag{A.4.15}$$

Similar expressions exist for $\mathcal{R}_{12}$ and ρ_{12} and it can be shown that

$$\mathcal{R}_{12}(\tau) = \mathcal{R}^*_{21}(-\tau). \tag{A.4.16}$$

A.4.3 Stationary Multivariate Processes

All of the concepts presented for a stationary bivariate process can be generalised to a multivariate process.

A multivariate process with n sample space elements is expressed by

$$\{\vec{\mathbb{X}}(t_1); \vec{\mathbb{X}}(t_2); \ldots; \vec{\mathbb{X}}(t_n)\},$$

or in a more compact form by $\{\vec{\mathbb{X}}(t)\}$; where $\vec{\mathbb{X}}$ is a column vector, containing the m variants of the process, defined for any t as

$$\vec{\mathbb{X}}(t) = \begin{pmatrix} \mathcal{X}_1(t) \\ \mathcal{X}_2(t) \\ \vdots \\ \mathcal{X}_m(t) \end{pmatrix}. \tag{A.4.17}$$

Using this definition, the *covariance matrix*, $\mathbb{R}$, at lag τ may be written as

$$\mathbb{R}(\tau) = \{\mathcal{R}_{ij}(\tau)\}, \quad i = 1, 2, \ldots, m, \quad j = 1, 2, \ldots, m; \tag{A.4.18}$$

where each matrix element is given by

$$\begin{aligned} \mathcal{R}_{ij}(\tau) &= \operatorname{cov}\{\mathcal{X}_j(t), \mathcal{X}_i(t+\tau)\} \\ &= \mathcal{E}\{ \Big(\mathcal{X}_j(t) - \mathcal{E}\{\mathcal{X}_j(t)\} \Big)^* \Big(\mathcal{X}_i(t+\tau) - \mathcal{E}\{\mathcal{X}_i(t+\tau)\} \Big) \}. \end{aligned} \tag{A.4.19}$$

Bibliography

Adrian R J. 'Scattering particle characteristics and their effect on pulsed laser measurements of fluid flow'. *Appl Opt*, 23:1690–1691 (1984).

Adrian R J. 'Image shifting technique to resolve directional ambiguity in double-pulsed velocimetry'. *Appl Opt*, 25(21):3855–3858 (1986*a*).

Adrian R J. 'Multi-point optical measurements of simultaneous vectors in unsteady flow – a review'. *Int J Heat Fluid Flow*, 7:127–145 (1986*b*).

Adrian R J. 'Particle-imaging techniques for experimental fluid mechanics'. *Opt Laser Eng*, 9:211–228 (1988*a*).

Adrian R J. 'Statistical properties of particle image velocimetry measurements in turbulent flow'. *Laser Anemometry in Fluid Mechanics*, III:115–129 (1988*b*). Lisbon: Instituto Superior Tecnico.

Adrian R J. 'Particle-imaging techniques for experimental fluid mechanics'. *Annu Rev Fluid Mech*, 23:261–304 (1991).

Adrian R J and Yao C S. 'Pulsed laser technique application to liquid and gaseous flows and the scattering power of seed materials'. *Appl Opt*, 24:44–52 (1985).

Akulichev V A. *High intensity ultrasonic fields*. Plenum Press, New York (1971).

Andrade E N D. 'On the circulation caused by the vibraion of air in a tube'. *P Roy Soc Lond A Mat*, 134:445–470 (1931).

Barker D B and Fourney M E. 'Measuring flow velocities with speckle patterns'. *Opt Lett*, 1:135–137 (1977).

Basset A B. 'On the acoustic radiation pressure on spheres'. *Philos Trans R Soc*, 179:43–63 (1888).

Blackshire J L. 'Analysis of particle image velocimetry (piv) data for acoustic velocity measurements'. *Technical report*, Hampton, Virginia (1997). NASA Contractor Report 201664.

Boussinesq J. 'Sur la résistance qu'oppose unliquide indéfini en repos, sans pesanteur au mouvement varié d'une sphére solide qu'il mouille sur toute sa surface, quand les vitesses restent bien continues et assez faibles pour que leurs carrés et produits soent négligeables'. *Comptes Rendus Academie des Sciences Paris*, 100:935–937 (1885).

Brandt O and Hiedemann E. 'The aggregation of suspended particles in gases by sonic and supersonic waves'. *Trans Faraday Soc*, 32(184):1101–1110 (1936).

Buick J M, Cosgrove J A, Campbell D M and Greated C A. *Development of an optical measuring technique for the study of acoustical phenomena*, pages 133–142. Professional Engineering Publishing (2002). Book: Optical Methods for Data Processing in Heat and Fluid Flow, ISBN: 1860582818.

Burch J M and Tokarski J M J. 'Production of multiple field fringes from photographic scatters'. *Optica Acta*, 15:101–111 (1968).

Campbell M, Cosgrove J A, Greated C A, Jack S and Rockliff D. 'Review of lda and piv applied to the measurement of sound and acoustic streaming'. *Opt Laser Technol*, 32:629–639 (2000).

Carter G C. Ph.D. thesis, University of Connecticut (1976).

Cooley J W and Tukey O W. 'An algorithm for the machine calculation of complex fourier series'. *Math Comput*, 297-301:19 (1965).

Cosgrove J A, Buick J M, Campbell D M and Greated C A. 'Piv applied to acoustical phenomena'. pages 470–486. Hong Kong, China (2001). The 8th International Congress on Sound and Vibration.

Coupland J M and Halliwell N A. 'Particle image velocimetry: rapid transparency analysis using optical correlation'. *Appl Opt*, 27:1919–1921 (1988).

Cummins H Z, Knable N and Yeh Y. 'Observation of diffusion broadening of rayleigh seatered light'. *Phys Rev Lett*, 12:150–153 (1964).

Elsinga G E, van Oudheusden B W and Scarano F. 'Evaluation of aero-optical distortion effects in piv'. pages 404–491. 12th International Symposium

on Applications of Laser Techniques to Fluid Mechanics, Lisbon, Portugal (2004).

Fahy F J. 'Measurement of acoustic intensity using the cross-spectral density of two microphone signals'. *J Acoust Soc Am*, 62(4):1057–1059 (1977).

Fowles G R. *Introduction to Modern Optics*. Holt, Rinehart and Winston Inc (1975).

Gharib M, Kremers D, Koochesfehani M M and Kemp M. 'Lèonardo's vision of flow visualization'. *Exp in Fluids*, 33:219–223 (2002).

Goodman J W. *Introduction to Fourier Optics*. McGraw-Hill (1968).

Grant I. 'Particle image velocimetry: a review'. volume 211 Part C, pages 55–76. Proc Instn Mech Engrs (1997).

Hann D B. *Simultaneous measurement of acoustic fields and flow fields using optical methods*. Ph.D. thesis, The University of Edinburgh (1995).

Hann D B and Greated C A. 'Measurement of acoustic particle velocity using particle image velocimetry techniques'. *Acustica*, 83(2):354–358 (1997a).

Hann D B and Greated C A. 'Particle image velocimetry for the measurement of mean and acoustic particle velocities'. *Meas Sci Technol*, 8(6):656–660 (1997b).

Hann D B and Greated C A. 'The measurement of flow velocity and acoustic particle velocity using particle image velocimetry'. *Meas Sci Technol*, 8(12):1517–1522 (1997c).

Hardy A C and Perrin F H. *The Principles of Optics*. McGraw-Hill (1932).

Hart D P. 'PIV error correction'. *Experiments in Fluids*, 29:13–22 (2000).

Hogg R V and Tanis E A. *Englewood Cliffs*. Dover, 5th edition (1996).

Humphreys Jr W M, Bartram S M, Parrott T L and Jones M G. 'Digital piv measurements of acoustic particle displacements in a normal incidence impedance tube'. 20th AIAA advanced measurement and ground tsting technology conference, Albuquerque, NM (1998). NASA Contractor Report 201664.

Imaichi K and Ohmi K. 'Numerical processing of flow-visualisation pictures—measurement of two-dimentional vortex flow'. *J Fluid Mech*, (129):283–311 (1983).

Jack S H, Hann D B and Greated C A. 'The influence of the acousto-optical effect on laser doppler anemometry signals'. *Rev Sci Instrum*, 69:4074–4081 (1998).

Jack S H, Hann D B and Greated C A. 'The influence of a standing wave on laser doppler signals'. *Meas Sci Technol*, 10(12):1279–1285 (1999).

Jetter J J, Guo Z, McBrian J A and Flynn M R. 'Characterization of emissions from burning incense'. *The Science of the Total Environment*, 296:51–67 (2002).

Johansson E L, Benckert L and Gren P. 'Particle image velocimetry (piv) measurement of velocity field at an organ labium'. pages 321–324. Stockholm Music Acoustics Conference 2003 (SMAC 03), Sweden (2003).

Kalinichenko A I, Lazurik V T and Zalyubovsky I I. *Introduction to Radiation Acoustics*. Harwood Academic Publishers (2001).

Keane R D and Adrian R J. 'Optimization of particle image velocimeters. part i: Double pulsed system'. *Meas Sci Technol*, (1):1202–1215 (1990).

Keane R D and Adrian R J. 'Optimization of particle image velocimeters. part ii: Multiple pulsed system'. *Meas Sci Technol*, (2):963–974 (1991).

Keane R D and Adrian R J. 'Theory of cross-correlation analysis of piv images'. *APPL SCI RES*, 49(3):191–215 (1992).

Kinsler L E, Frey A R, Coppens A B and Sanders J V. *Fundamentals of Acoustics*. John Wiley & Sons, Inc, New York, 4th edition (2000).

Knapp C H and Carter G C. 'The generalized method for estimation of time delay'. *IEEE Transactions on Acoustics, Speech, and Signal*, 24:320–327 (1976).

Lamb L. *Hyrodynamics*. Dover, New York, 6th edition (1932).

Landau L D and Lifshitz E M. *Fluid Mechanics*. Butterworth-Heinemann, Oxford, 2nd edition (1987).

Learned J G. 'Acoustic radiation by charged atomic particles in liquids: An analysis'. *Physical Review D (Particles and Fields)*, 19:3293–3307 (1979).

Lighthill J. 'Acoustic streaming'. *Journal of Sound and Vibration*, 83(3):391–418 (1978).

Marshall I. 'The production of acoustic impulses in air '. *Measurement Science and Technology*, 1:413–418 (1990).

Meinhart C D, Wereley S T and Santiago J G. 'Piv measurements of a microchannel flow'. *Exp in Fluids*, 27:414–419 (1999).

Meyer E and Neumann E G. *Physical and applied acousics*. Academic Press, New York (1972). Translated by J M Taylor, Jr.

Morse P M and Ingard K U. *Theoretical Acoustics*. McGraw-Hill, USA (1968).

Nyborg W L. *Physical Acoustics IIB*, pages 265–331. Academic, New York (1965).

Oseen C W. *Hydromechanik*. Academische Verlag, Leipzig, Germany (1927).

Polyanin A D and Zaitsev V F. *Handbook of Exact Solutions for Ordinary Differential Equations*. CRC Press, Boca Raton, FL (1995).

Prandtl L. 'Über flüssigkeitsbewegung bei sehr kleiner reibung'. pages 404–491. verhandlungen des III. International Mathematiker-Kongresses, Heidelberg (1904).

Pratt R L, Elliott S J and Bowsher J M. 'The measurement of the acoustic impedance of bras instruments'. *Acustica*, 38:236–246 (1977).

Press W H, Flannery B P, Teukolsky S A and Vetterling W T. *Numerical recipes in FORTRAN: The art of acientific computing*. Cambridge University Press, Cambridge, England, 2nd edition (1992).

Priestly M B. *Spectral analysis and time series*. Academic Press, London (1981).

Raffel M, Willert C and Kompenhans J. *Particle Image Velocimetry: A Practical Guide*. Springer, Berlin Heidelberg (1998).

Rayleigh L. *The Theory of Sound*, volume II. Dover, New York, 2nd edition (1945).

Reynolds O. 'On the experimental investigation of the circumstances which determines whether the motion of water shall be direct or sinuous and the law of resistance in parallel channels'. *Philos Trans R Soc*, 174:435–982 (1883).

Riley N. 'Steady streaming'. *Annu Rev Fluid Mech*, 33:43–65 (2001).

Rockliff D. *Application of particle image velocimetry to the measurement of non-linear effects generated by high-intensity acoustic fields*. Ph.D. thesis, The University of Edinburgh (2002).

Rockliff D, Campbell D M and Greated C A. 'Piv experimental study on acoustic streaming in cylindrical air-filled tubes using high intensity sound field'. pages 199–202. The 5th French Congress on Acoustics (CFA) 2000, France (2000).

Rockliff D and Greated C A. 'Application of piv to the measurement of acoustic fields in woodwind instruments'. pages 399–402. International Symposium on Musical Acoustics (ISMA) 2001, Perugia, Italy (2001).

Sapriel J. *Acousto-Optics*. John Wiley & Sons, Inc (1979).

Sharpe J P, Greated C A, Gray C and Campbell D M. 'The measurement of acoustic streaming using particle image velocimetry'. *Acoustica*, 68:168–172 (1988).

Skudrzyk E. *The foundations of acoustics*. Springer-Verlag, Austria (1971).

Skulina D J, Campbell D M and Greated C A. 'Measurment of the termination impedance of a tube using particle image velocimetry'. pages 747–750. Stockholm Music Acoustics Conference 2003 (SMAC 03), Sweden (2003).

Stokes G G. 'On the theory of oscillatory waves'. *Trans Camb Phil Soc*, 8:441–455 (1847).

Taylor K J. 'Absolute measurement of acoustic particle velocimetry'. *J Acoust Soc Am*, 59(3):691–694 (1976).

Temkin S. *Elements of acoustics*. John Wiley & Sons, Inc, USA (1981).

van der Eerden F J M, de Bree H E and Tijdeman H. 'Experiments with a new acoustic particle velocity sensor in an impedance tube'. *Sensor Actuat A-Phys*, 69(2):126–133 (1998).

Vignola J F, Berthelot Y H and Jarzynsky J. 'Laser detection of sound'. *J Acoust Soc Am*, 90(3):1275–1286 (1991).

Wernet M P. 'Symmetric phase-only filtering: a newparadigm for DPIV data processing'. *Meas Sci Technol*, 16:601–618 (2005).

Wernet M P and Edwards R V, editors. *Application of optical correlation techniques to particle imaging* (1988).

Westerweel J. *Digital Particle Image Velocimetry - Theory and Application*. Ph.D. thesis, Delft University (1993).

Westerweel J. 'Fundamentals of digital particle image velocimetry'. *Meas Sci Technol*, (8):1379–1392 (1997).

Westerweel J, Dabiri D and Gharib M. 'The effect of a discrete window offset on the accuracy of cross-correlation analysis of digital PIV recordings'. *Experiments in Fluids*, 23:20–28 (1997).

Willert C E and Gharib M. 'Digital particle image velocimetry'. *Exp in Fluids*, 10:181–193 (1991).

Yeh Y and Cummins H Z. 'Localized fluid flow measurements with an he-ne laser spectrometer'. *Phys Rev Lett*, 4:176–178 (1964).

Young M. *Optics and Lasers*. Springer-Verlag, Berlin, 3rd edition edition (1986).

Nomenclature

Roman Letters

$\mathcal{A}$	Complex field amplitude of light
$\mathcal{B}$	Adiabatic bulk modulus
c	Thermodynamic speed of sound of fluid
$\mathcal{C}$	Density of particle-source number
C_D	Drag Coefficient
č	Speed of light
c_P	Specific heat of fluid at constant pressure
c_V	Specific heat of fluid at constant volume
$\vec{d}$	Displacement field
D	Diameter
d_i	Image distance
$\vec{\tilde{d}}$	Displacement field in image space
D_L	Diameter of lens
d_o	Object distance
$\mathcal{E}$	Event
$\mathfrak{E}$	Experiments
$\mathcal{F}$	Distribution function
F	Force
f	Frequency
$f^{\#}$	Lens f-number
f	Probability distribution function (PDF)
F_I	In-plane loss-of-correlation

F_O	Out-of-plane loss-of-correlation
f_r	PDF of size distribution of aerosol particles
f_v	PDF of velocity distribution of aerosol particles
G	Particle-source pattern
$\tilde{G}$	Particle-image pattern
$\mathcal{H}$	Impulse response
$\mathcal{H}_{\mathcal{A}}$	Impulse response of imaging system
$\mathcal{H}_{I_\Delta I}$	Discrete impulse response
$\mathcal{H}_G$	Impulse response of particle-source pattern
I	Windowed irradiance
$\Delta\tilde{x}_I$	$= (\tilde{x}_I, \tilde{y}_I)$, Interrogation area dimensions in image plane
I_Δ	Discrete irradiance field
$\bar{I}_\Delta$	Mean of Discrete irradiance field
$\tilde{\mathcal{I}}$	Irradiance
$\mathcal{I}$	Intensity of light field
$\mathcal{J}_n$	The nth order Bessel function of the first kind.
k	Wave number
$\mathbf{k}$	Complex wave number
$\check{k}$	Wave number of light field
L	Length
Δ_L	Resolution limit of lens
l	Displacement amplitude of the sound generating device
M	Magnification
N	Interrogation area size in pixels
$\mathcal{N}_F$	The Fresnel number
$\mathcal{N}_I$	Image density
$\mathcal{N}_p$	Number of particle-sources
$\mathcal{N}_p$	Instantaneous number of aerosol particles
n_p	Instantaneous number density of aerosol particles
$\mathcal{N}_{p_0}$	Equilibrium number of aerosol particles
n_{p_0}	Equilibrium number density of aerosol particles

$\delta\mathcal{N}_p$	Fluctuation of number of aerosol particles
δn_p	Fluctuation of number density of aerosol particles
$\mathcal{N}_{Re}$	Reynolds number of the aerosol particles
$\mathcal{N}_S$	Source density
n_s	Scanning rate
p	Probability
$\mathcal{P}_0$	Equilibrium pressure of fluid
$\mathcal{P}$	Instantaneous pressure of fluid
p	Acoustic pressure
p	Reference pressure level
p_0	Acoustic pressure amplitude
Δ_{px}	Dimensions of pixel area
$\widehat{\mathcal{R}}$	Estimated covariance matrix element
r	Radius
$\tilde{r}_A$	Radius of the Airy disk
Δ_R	Resolution limit of recording medium
r_I	Radius of interrogation spot
r_p	Radius of source-particle
$\tilde{r}_p$	Radius of particle-image
S	Area
$\vec{s}$	Correlation plane
s	Condensation of fluid
$\vec{s}_\Delta$	$= (s_{\Delta_x}, s_{\Delta_y})$, Discrete correlation plane
S_I	Interrogation area
$\vec{\tilde{s}}$	Correlation plane in image space
t	Time
T	Temperature in degrees Celsius
T_K	Temperature in Kelvin
t_v	Velocimetry time
V	Volume
$\vec{v}$	$= (v_x, v_y, v_z)$, Velocity vector, Particle velocity of a fluid element

v_0	Acoustic velocity amplitude
V_I	Interrogation cell
$\vec{v}_p$	Velocity of source-particle, velocity of aerosol particles
V_R	Resolution cell
$\mathcal{W}$	Window function
W_P	Bandwidth
$\vec{x}$	$= (x, y, z)$, Position vector
$\hat{x}, \hat{y}, \hat{z}$	Position normal vectors
$\vec{x}_\Delta$	$= (x_\Delta, y_\Delta)$, Discrete position vector
$\vec{\tilde{x}}$	$= (\tilde{x}, \tilde{y})$, Position vector in image space
χ	Random variable parameter
$\mathcal{X}$	Random variable
$\vec{\mathbb{X}}$	Random variable vector
Δx_L	Length of light sheet
Z	Acoustic impedance
Z_0	Characteristic impedance
Δz_L	Thickness of light sheet
Z_M	Mechanical impedance
Z_S	Specific impedance

Greek Letters

α	Absorption coefficient
α_S	Spatial absorption coefficient
γ	Specific heat ratio
Γ	Valid-data yield
γ_f	Focal length
δ	Dirac delta-function
η	Dynamic viscosity coefficient of fluid
η_B	Bulk viscosity coefficient of fluid
ϑ	The angle between the light sheet normal and the tube axis
κ	Thermal conductivity of fluid
λ	Wavelength

$\check{\lambda}$	Wavelength of light field
ν	Kinematic (shear) viscosity coefficient of fluid
μ	Mean
μ_g	Flow-around coefficient
μ_p	Entrainment coefficient
ρ_0	Equilibrium density of fluid
ρ	Instantaneous density of fluid
ρ_p	Density of source-particle
ρ	Autocorrelation
τ_i	Illumination duration
τ_s	Scanning duration
$\delta\tau_s$	Scanning step
σ_ν	Width of velocity distribution of aerosol particles
τ_f	Relaxation time of viscous fluid elements
τ_p	Relaxation time of aerosol particles
τ_S	Spatial relaxation time of viscous fluid elements
ϕ	Velocity potential of sound wave
ϕ_0	Velocity potential amplitude of sound wave
φ	Phase
φ	Phase shift angle
$\check{\varphi}$	Phase of light field wave
$\vec{\chi}$	$= (\chi_x, \chi_y)$, Position vector in the FOURIER'S SPACE
χ	Thermal diffusivity of fluid
$\vec{\xi}$	$= (\xi_x, \xi_y, \xi_z)$, Displacement from equilibrium of a fluid element
$\underline{\Omega}$	Sample space
Ω	Element of sample space
ω	Angular frequency
$\check{\omega}$	Angular frequency of light field wave

Other Symbols

$\imath$	Imaginary unit
$\star$	Correlation

$\circledast$	Convolution
.	Scalar product
$\rightarrow$	Vector symbol
σ	Variance
$\mathcal{C}\{\,,\,\}$	Correlation coefficient operator
$\mathrm{cov}\{\,,\,\}$	Covariance operator
$\mathbb{R}$	Covariance matrix
$\mathcal{R}$	Covariance matrix element
d	Differentiation
∂_x	Partial differentiation
$\vec{\nabla}$	Gradient
$\vec{\nabla}.$	Divergent
$\vec{\nabla}\times$	Curl
∇^2	$= \partial_x^2 + \partial_y^2 + \partial_z^2$, Laplacian operator
$\Box^2$	d'Alembertian operator
$\Box_L^2$	Lossy d'Alembertian operator
$\mathcal{E}\{\}$	Expectation operator
$\langle\,\rangle$	Mean operator
$\langle\,\rangle_x$	Mean value over x
$\mathfrak{F}\,[\,]$	Fourier transform operator
$\mathfrak{DFT}\,[\,]$	Discrete Fourier transform (DFT) operator
$\mathfrak{DFT}^{-1}\,[\,]$	Reverse discrete Fourier transform (DFT) operator
$\mathfrak{R}\,[\,]$	Real part
$\mathfrak{I}\,[\,]$	Imaginary part

About the Cover

A PIV analysis of two woodcut engravings corresponding to 1666 (left) and 1999 (right) based on the novel *The Club Dumas* by Arturo Pérez-Reverte. The 1666 engraving belongs to the book *De Umbrarum Regis Novum Portis* written by a fictional author named Aristide Torchia in Venice, where the actual engraving was performed by the artist Francisco Solé. The 1999 engraving is from the film *The Ninth Gate* by Roman Polański.
Aligned by the engraved borders, the images were analysed using correlation-based correction combined with the symmetrical phase-only filter.